Master's Thesis

# Real Gas Effects on Spray Evaporation Modelling under High Pressure Diesel Injection Conditions

Written by

Grabner Matthias, BSc.

Supervisors:

Ass.Prof. Dipl.-Ing. Dr.techn. Thomas Wallek, TU Graz

Dr. Klaus Pachler, AVL List GmbH

Institute of

Chemical Engineering and Environmental Technology

Graz, August 2016

## STATUTORY DECLARATION

I declare that I have authored this thesis independently, that I have not used other than the declared sources / resources, and that I have explicity marked all material which has been quoted either literally or by content from the used sources.

date                                                              (signature)

## Abstract

Temperature and pressure change significantly in an internal combustion engine during the compression cycle. The behavior of single component droplets in evaporation processes in high pressure environments is well investigated [1][2][3]. However, only few investigations for multicomponent droplets have been found for high pressure environments.

In this master thesis an already available multicomponent evaporation model by Abramzon, Sirignano [4] and Brenn et al. [5] is extended by a real gas equation of state for the AVL FIRE™ CFD code. The Universal Group Contribution Volume Translated Peng Robinson equation of state has been used to calculate the fugacity coefficients in gas and liquid phase at the droplet surface which modify the evaporation rate of the fuel components as compared with the previous ideal gas approach. This addition accounts for high pressure effects during evaporation. Furthermore ,the non-uniform heating process inside a droplet is taken into account by a series expansion approach for solving the heat conduction equation through a model by Frolov [6].

To examine the impact of the modified model, multiple computer simulations with multicomponent fuels were executed and analyzed. Therefore, various simulations with the old and modified model for single droplet, spray box and engine sector simulation cases were set up.

Most significant deviations between the original and the modified model were identified in the near injector region where fuel vapor and spray droplets coexist. However, average results over the used calculated computational grids as, e.g. mean spray penetration, pressure curves and rate of heat release in engine calculations showed only minimal differences.

# Table of Contents

## List of Figures

## List of Tables

## Nomenclature

| Symbol | Name | Unit |
|---|---|---|
| **Latin Symbols** | | |
| a | attraction parameter | (J m³)/mol² |
| | thermal diffusity | m²/s |
| $a_{ij}$ | cross- correlation attraction parameter | (J m³)/mol² |
| | UNIFAC binary interaction parameter | K |
| A | cubic equation coefficient | - |
| | Antoine constant | - |
| | Two-Suffix Margules empirical constant | J/mol |
| b | co-volume parameter | m³/mol |
| $b_{ij}$ | cross- correlation mole specific co-volume parameter | m³/mol |
| | UNIFAC binary interaction parameter | - |
| B | cubic equation coefficient | - |
| | Antoine constant | - |
| $B_H$ | Spalding heat transfer number | - |
| $B_M$ | Spalding mass transfer number | - |
| c | translation parameter | m³/mol |
| $c_{ij}$ | UNIFAC binary interaction parameter | 1/K |
| $c_p$ | specific heat capacity | J/(kg K) |
| C | cubic equation coefficient | - |
| | Antoine constant | - |
| | constant | - |
| D | mass diffusivity | m²/s |
| f | fugacity | Pa |
| g | molar Gibbs free energy | J/mol |
| G | Gibbs free energy | J |

| | | |
|---|---|---|
| h | height | m |
| K | K-Factor | - |
| I | integral | - |
| $k_{ij}$ | binary interaction parameter | - |
| $l_{ij}$ | binary interaction parameter | - |
| L | Twu, component specific parameter | - |
| m | EoS alpha-function component specific constant | - |
| | mass | kg |
| $\dot{m}$ | mass flow | kg/s |
| M | Twu, component specific parameter | - |
| n | EoS alpha-function component specific constant | - |
| | mole | mol |
| N | Twu, component specific parameter | - |
| P | pressure | Pa |
| q | relative van-der-Waals surface | - |
| | arbitrary EoS variable | - |
| | group vdW surface | - |
| r | relative van-der-Waals volume | - |
| | radius | m |
| R | universal gas constant | J/(mol K) |
| | group vdW volume | - |
| s | molar entropy | J/mol |
| t | time | s |
| T | temperature | K |
| v | molar volume | m³/mol |
| u | molar internal energy | J/mol |
| x | mole fraction | - |
| X | mole fraction | - |

| | | |
|---|---|---|
| y | mass fraction | - |
| z | real gas factor | - |
| | coordination number | - |

**Greek Symbols**

| | | |
|---|---|---|
| $\alpha$ | NRTL non-randomness constant | - |
| | EoS alpha-function | - |
| | sector angle | ° |
| $\beta$ | arbitrary EoS variable | - |
| $\chi$ | arbitrary EoS variable | - |
| $\gamma$ | activity coefficient | - |
| $\varepsilon$ | EoS constant | - |
| $\lambda$ | thermal conductivity | W/(m K) |
| $\mu$ | chemical potential | J/mol |
| $\rho$ | density | kg/m³ |
| $\sigma$ | EoS constant | - |
| $\theta$ | average area fraction | - |
| $\Theta$ | group average area fraction | - |
| $\tau_{ij}$ | binary interaction parameter | - |
| $\phi$ | average segment fraction | - |
| $\Psi$ | UNIFAC parameter | - |
| $\varphi$ | fugacity coefficient | - |
| $\omega$ | acentric factor | - |

**Nondimensional Parameters**

| | |
|---|---|
| $B_M$ | Spalding Mass Transfer Number |
| $B_H$ | Spalding Heat Transfer Number |

F       Generalized Correction Function

$Nu_0$      diffusive Nusselt number

$Nu^*$      modified Nusselt number

Pr      Prandtl number

Re      Reynolds number

Sc      Schmidt number

$Sh_0$      diffusive Sherwood number

$Sh^*$      modified Sherwood number


**Superscripts**

'       reference state

+       next calculated variable

0       reference state

att     attraction

E       excess

iG      ideal Gas

l       liquid phase

rep     repulsion

s       saturated state

v       vapour phase


**Subscripts**

0       reference state

∞       ambient condition

c       critical

calc    calculated

comb    combinatorial

d       droplet

| | |
|---|---|
| d,c | droplet center |
| d,s | droplet surface |
| exp | experimental |
| f | in droplet gas film |
| H | heat transfer |
| M | mass transfer |
| | Michelsen |
| r | reduced intensive state variable |
| res | residual |
| s | surface |
| SV | Stryjek-Vera |
| thres | threshold |
| UGC | Universal Group-Coefficient |
| V | Vidal |
| i | component index i |
| j | component index j |
| k | component index k |

## Abbreviations

| | |
|---|---|
| AAD | Average Absolute Deviation |
| CA | Crank Angle |
| CFD | Computational Fluid Dynamics |
| cEoS | cubic Equation of State |
| DOI | Direction of Injection |
| EoS | Equation of State |
| HV | Huron-Vidal |
| ICE | Internal Combustion Engine |
| iG | ideal Gas |

| | |
|---|---|
| LCVM | Linear Combination of HV and Michelsen |
| MHV1/2 | Michelsen Huron-Vidal ½ |
| mMC | modified Multi- Component |
| NP | Number of Points |
| NRTL | Non-Random Two-Liquid |
| oMC | original Multi- Component |
| PR | Peng-Robinson |
| PSRK | Predictive Soave-Redlich-Kwong |
| SRK | Soave-Redlich-Kwong |
| SV | Stryjek-Vera |
| UGC | Universal Group-Coefficient |
| UNIFAC | Universal Quasi-Chemical Functional Group Activity Coefficients |
| vdW | van der Waals |
| VLE | Vapour-Liquid-Equilibrium |
| VTPR | Volume-Translated Peng-Robinson |
| WS | Wong Sandler |

# Acknowledgements

I would like to thank Prof. Thomas Wallek for sparking my interest in chemical engineering.

I would like to thank Dr. Klaus Pachler for the opportunity to write my master's thesis at AVL AST.

I would like to thank Dipl.-Ing. von Berg for his persistent technical support throughout the work.

Thanks to all my friends. Especially Lisa König, Hannes Wolf, Martin Almer, Manuel Bruschi. Without you I certainly wouldn't have come this far.

Last but not least I would like to thank my parents for their lifelong support. Without you I literally would not be here.

Graz, August 2016                                                                            Matthias Grabner

# 1. Introduction

In the FIRE™ CFD code the droplet evaporation is treated by a Lagrangian model for the dispersed phase, which is applied in-between subsequent gas phase solution time steps of the overall Navier-Stokes-Solver.

The correct spray modelling of fuels is very important in engines influencing the evaporation of the fuel and further processes such as burning and the composition of the pollutants which is fundamentally dependent on the mixture composition. The accuracy of the droplet evaporation modelling affects all successive phases. Especially the droplet evaporation model may influence the liquid and the vapour penetration length and the compound composition in the gas phase.

The evaporation of a droplet is controlled by the phase change of the species at the surface of the droplet. The relation between the liquid droplet phase and the surrounding gas phase is described through a vapour-liquid equilibrium.

The ideal gas assumption is sufficient at "low" pressures (chapter 5 of [7]) while for rising pressure real gas effects become increasingly important:

1. in the evaporation of droplets
2. in the gas- phase surrounding the droplet
3. in the overall gas flow solver

Depending on the respective pressure and temperature the model of the VLE may have a considerable impact on the calculated evaporation rate. The present work focuses on the description of VLE modelling. Taking into account real gas effects instead of the existing assumptions of validity of the ideal gas conditions.

## 2. Vapour-Liquid Equilibrium (VLE)

The following chapter describes how the VLE is defined. Vapour and liquid of a species are in equilibrium if the pressures, temperatures and chemical potentials of all phases $\alpha, \beta, ..., \pi$ are equal.

$$P^{\alpha} = P^{\beta} = ... = P^{\pi}$$
$$T^{\alpha} = T^{\beta} = ... = T^{\pi} \qquad (2.1)$$
$$\mu_i^{\alpha} = \mu_i^{\beta} = ... = \mu_i^{\pi}$$

Since direct usage of chemical potential in VLE calculations has some practical disadvantages (e.g. for ideal gas and low pressure the chemical potential tends to negative infinity [8]) the auxiliary entity fugacity was introduced by Lewis [9] to account for non- idealities [10]. It can be shown that fugacities are equivalent to the chemical potentials of the individual components in describing the VLE. Thus identity of fugacities in each phase is applied as VLE condition in this work.

$$f_i^{\alpha}(T^{\alpha}, \mathbf{P}^{\alpha}) = f_i^{\beta}(T^{\beta}, \mathbf{P}^{\beta}) = ... = f_i^{\pi}(T^{\pi}, \mathbf{P}^{\pi}) \qquad (2.2)$$

For the VLE we can write:

$$f_i^{v} = f_i^{l} \qquad (2.3)$$

with $f_i^{v}$ as the fugacity of the species i in the vapour phase and $f_i^{l}$ as the fugacity of the species i in the liquid phase.

In general one of two methods to calculate the fugacities can be chosen.

1. The equation of state (EoS), $(\varphi - \varphi)$ method:

Through the help of the fugacity coefficient which is defined as ratio of fugacity to pressure or partial pressure in the case of mixtures it can be written for the vapour phase

$$f_i^{v} = y_i \varphi_i^{v} P \qquad (2.4)$$

$y_i$ is the mole fraction of the species i in the vapour phase, $\varphi_i^v$ is the fugacity coefficient of the species i in the vapour phase, $P$ is the pressure of the system. The fugacity of the liquid phase is defined in an analogous way by

$$f_i^l = x_i \varphi_i^l P \tag{2.5}$$

$x_i$ is the mole fraction of the species i in the liquid phase, $\varphi_i^l$ is the fugacity coefficient of the species i in the liquid phase, $P$ is the pressure of the system.

2. The second method involves the utilization of the activity coefficient which can be calculated from an excess Gibbs energy model for the liquid phase, $(\gamma - \varphi)$ method:

The activity of a species is defined by Lewis as the ratio of its fugacity $f_i$ and a reference fugacity $f_i^0$.

$$a_i(T,P,x_i) = \frac{f_i(T,P,x_i)}{f_i^0(T,P^0,x_i^0)} \tag{2.6}$$

The activity coefficient is defined through the ratio of activity and the conveniently chosen liquid mole fraction and is preferred by engineers to describe the local measure of non-ideal behaviour of the liquid phase [11].

$$\gamma_i = \frac{a_i}{x_i} \tag{2.7}$$

From this definition the liquid fugacity of a species in a mixture can be expressed as

$$f_i^l = x_i \gamma_i f_i^0 \tag{2.8}$$

with $x_i$ as the mole fraction of the species i in the liquid phase, $\gamma_i$ as the activity coefficient of the species i in the liquid phase, $f_i^0$ as the reference fugacity of the pure species i. As the reference state for the fugacity of the species i in the mixture usually the fugacity of the pure saturated liquid at temperature and pressure of the system is used [12]. This can be expressed as

$$f_i^0 = \varphi_i^s P_i^s POY_i \tag{2.9}$$

which is determined by $\varphi_i^s$ the fugacity coefficient of the species i at saturation, $P_i^s$ the vapour pressure of the species i at saturation and $POY_i$ the Poynting correction of species i to account for the pressure dependence (deviation from saturation pressure to system pressure) of the fugacity.

For the first $(\varphi - \varphi)$ method to calculate the molar fraction of the vapour phase $y_i$, Eq. (2.4) and Eq. (2.5)are combined to

$$y_i \varphi_i^v = x_i \varphi_i^l$$

yielding

$$y_i = x_i \frac{\varphi_i^l}{\varphi_i^v} \tag{2.10}$$

and the K- factor

$$K_i = \frac{y_i}{x_i} = \frac{\varphi_i^l}{\varphi_i^v} \tag{2.11}$$

Equations of state are used to calculate the fugacity coefficients and to solve Eq.(2.10) . These will be further described in the following chapter 3 for single components and chapter 5 for multi-components.

For the second $(\gamma - \varphi)$ model to calculate the molar fraction of the vapour phase $y_i$. Eq.(2.4) , (2.8) and (2.9) are combined to

$$y_i \varphi_i^v P = x_i \gamma_i \varphi_i^s P_i^s POY_i$$

yielding

$$y_i = x_i \gamma_i \frac{P_i^s}{P} \left[ \frac{\varphi_i^s POY_i}{\varphi_i^v} \right] \tag{2.12}$$

and the K- factor

$$K_i = \frac{y_i}{x_i} = \gamma_i \frac{P_i^s}{P} \left[ \frac{\varphi_i^s POY_i}{\varphi_i^v} \right] . \tag{2.13}$$

The last term on the RHS in brackets of Eq. (2.12) for moderate pressures is around unity [12]. With that only an activity coefficient model has to be chosen to solve Eq. (2.12). The activity coefficients are calculated through an activity coefficient model. Methods to calculate activity coefficients are described in chapter 4.

The K-factor or also vapour/liquid equilibrium ratio $K_i$ as seen in (2.11) and (2.13) depends on the respective VLE model selected.

For this thesis both methods are utilized for validation of experimental binary data but only the first $(\varphi - \varphi)$ method is used for the performed droplet evaporation simulations.

## 3. Equations of State (EoS)

The pressure-volume-temperature (PvT) behavior of a pure substance and of mixtures can be described by equations of state (EoS). In an EoS the temperature, pressure and volume are related. An EoS offers the possibility to calculate all real thermodynamic properties, due to the availablility of residual functions and excess properties, with the ideal thermodynamic properties known. The simplest form of an EoS is the ideal gas law:

$$Pv = RT \tag{3.1}$$

with $v$ as the molar volume and $R$ as the universal gas constant $R = 8.134 \ \mathrm{Jmol^{-1}K^{-1}}$.

As mentioned the ideal gas law is a simplified model not taking into account repulsive or attractive forces between the molecules of the substance. These terms were first proposed by van der Waals [13] in his cubic equation of state:

$$P = P^{rep} + P^{att} \tag{3.2}$$

$$P = \frac{RT}{v-b} - \frac{a}{v^2} \tag{3.3}$$

is called the pressure explicit form with can be rewritten as the general form

$$1 = \frac{1}{z-\beta} - \frac{q\beta}{z^2} \tag{3.4}$$

$$\text{with } \beta = \frac{bP}{RT}, \quad q = \frac{a}{bRT}$$

the parameter $b$ as the co-volume and parameter $a$ as the attraction parameter. The real gas factor z is the deviation from the ideal gas law which can be defined as

$$z = \frac{Pv}{RT} \tag{3.5}$$

The cubic equation and its parameters allow the description of a liquid and a vapour phase. There are numerous modifications to the van der Waals cubic equation of state: the equation of Redlich-Kwong [14], Soave-Redlich-Kwong [15], Peng-Robinson [16] and many more.

In Figure 1 the comparison of a density calculation for the component carbon dioxide for the P-$\rho$ isotherms at 300 and 600 K is shown between the ideal gas law and the Peng-Robinson Stryjek-Vera (PR-SV) cubic equation of state. It can be seen that the ideal gas law is generally valid for $P \rightarrow 0$ and $T \rightarrow \infty$. As the pressure and temperature deviate from these ideal conditions the ideal gas law deviates from the real fluid. The black vertical continuous line shows the limit of density that is theoretically possible through the co-volume parameter M/b and the black horizontal continuous line shows the pressure limit, as the pressure cannot become negative.
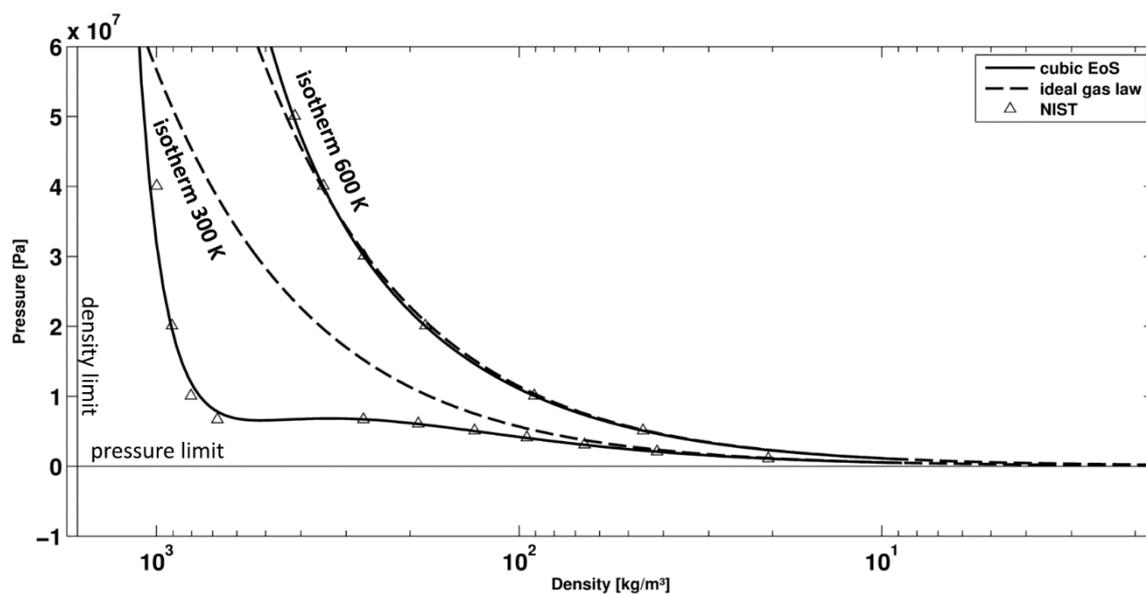


**Figure 1: Comparison of density calculation between the ideal gas law and a cubic equation of state as well with experimental data from NIST**[17]**.**

As the a most general form, the cubic equation of state can be written as

$$P = \frac{RT}{v - b + c} - \frac{a}{(v + \varepsilon b + c)(v + \sigma b + c)}$$

(3.6)

with coefficients a, b and c depending on critical data and partly also on temperature and the acentric factor $\omega$. The latter introduces an additional dependency from the reduced saturation pressure of the individual components (see Eq.(3.13) )

In Table 1 a few examples for equation of state parameters are listed.

**Table 1: Parameters $a$, $\sigma$, $\varepsilon$ and $c$ for a few specific EoS**

| Equation | $a$ | $\sigma$ | $\varepsilon$ | $c$ |
|---|---|---|---|---|
| *van der Waals(vdW)* | $a_c$ | $0$ | $0$ | $0$ |
| *Peng-Robinson(PR)* | $a(T,\omega)$ | $1+\sqrt{2}$ | $1-\sqrt{2}$ | $0$ |
| *Soave-Redlich-Kwong(SRK)* | $a(T,\omega)$ | $1$ | $0$ | $0$ |
| *Volume-Translated PR(VTPR)* | $a(T,\omega)$ | $1+\sqrt{2}$ | $1-\sqrt{2}$ | $c$ |

This again can be written as the pressure explicit (e.g. PR EoS) form

$$P = \frac{RT}{v-b} - \frac{a(T,\omega)}{v^2 + 2bv - b^2} \tag{3.7}$$

or the general form

$$1 = \frac{1}{z-\beta} - \frac{q\beta}{z^2 + 2\beta z - \beta^2} \quad . \tag{3.8}$$

The temperature dependent attraction parameter $a(T,\omega)$ was first proposed by Wilson [18] and further developed by Soave [15]. This improvement in accuracy for pure species also leads to an improvement in mixtures [15]. It is composed of a constant part $a_c$ and a temperature and $\omega$ - dependent part $\alpha$.

$$a(T,\omega) = a_c \cdot \alpha(T,\omega) \tag{3.9}$$

The parameters $a_c$ and $b$ can be determined through fitting of PVT data or through the critical data of the species using $\left(\frac{\partial P}{\partial v}\right)_{T_c} = 0$, $\left(\frac{\partial^2 P}{\partial v^2}\right)_{T_c} = 0$. These parameters are equation of state specific (seen in Table 2) if critical data of the species are used.

The critical data were used for the calculation of the parameters $a_c$ and $b$ in this thesis.

**Table 2: Attraction parameter *a* and co- volume parameter *b* for a few specific EoS determined at the critical point**

| EoS | $a_c$ | $b$ |
|---|---|---|
| vdW | $\dfrac{27}{64}\dfrac{R^2 T_c^2}{P_c}$ | $\dfrac{1}{8}\dfrac{RT_c}{P_c}$ |

| SRK | $0.42748 \dfrac{R^2 T_c^2}{P_c}$ | $0.08664 \dfrac{R T_c}{P_c}$ |
|---|---|---|
| PR/VTPR | $0.45724 \dfrac{R^2 T_c^2}{P_c}$ | $0.0778 \dfrac{R T_c}{P_c}$ |

$T_c$ is the critical temperature and $P_c$ is the critical pressure of the species.

There are further developments trying to improve $\alpha(T, \omega)$. Some of them which were used in this thesis are depicted in Table 3. A more complete overview is given in [19].

**Table 3:** $\alpha(T)$ **functions considered in the present work. The function parameters for selected components can be found in Appendix C - Alpha Function Parameters.**

| *Author* | $\alpha(T)$ *- function* |
|---|---|
| *Soave*[15] | $\left[ 1 + m_i \left( 1 - \sqrt{T_r} \right) \right]^2$ (3.10) <br> $m_i = 0.48 + 1.574 \omega_i - 0.176 \omega_i^2$ |
| *Stryjek and Vera*[20] | $\left\{ 1 + \left[ m_i + n_i \left( 1 - \sqrt{T_r} \right) \left( 0.7 - T_r \right) \right] \left( 1 - \sqrt{T_r} \right) \right\}^2$ <br> $m_i = 0.378893 + 1.4897153 \omega_{SV,i} - 0.17131848 \omega_{SV,i}^2 + 0.0196554 \omega_{SV,i}^3$ (3.11) <br> $n_i$... pure component specific |
| *Twu et al.*[21] | $T_r^{N(M-1)} \exp\left[ L(1 - T_r^{NM}) \right]$ (3.12) <br> $L_i, M_i, N_i$... pure component specific |

In Table 3 $T_r$ denotes the reduced temperature $T_r = T / T_c$ and $\omega_i$ is the acentric factor of the species i. The acentric factor is used to improve the EoS at saturation-condition and to account for the complexity of the molecule. It was introduced by Pitzer [22] and can be calculated by

$$\omega = -1 - \log\left( P_r^s \right)_{0.7 \cdot T_r} .$$ (3.13)

It should be noted that Stryjek and Vera [20] are using a marginally deviating $\omega_{SV}$ from the general $\omega$ as their parameters are a result of a best fit to experimental data.

Twu et al.[21] proposed an exponential function to correlate the vapour pressure of pure components using an equation of state. Although there is an equation for the subcritical and supercritical region available, only the subcritical equation Eq.(3.12) is used as proposed by [23] to achieve better consistency in the Universal Group Contribution Volume-Translated PR EoS (UGC VTPR EoS) which is further explained in chapter 5.3 Mixing Rules.

The Volume-Translated-Peng-Robinson (VTPR) EoS is a further improved cEoS to accurately calculate the liquid density through an additional volume translation parameter c (Figure 2).

The pressure explicit VTPR EoS

$$P = \frac{RT}{v - b + c} - \frac{a(T, \omega)}{(v + c)(v + b + c) + b(v - b + c)} \tag{3.14}$$

and the general form

$$1 = \frac{1}{z - \beta + \chi} - \frac{q\beta}{(z + \chi)(z + \beta + \chi) + \beta(z - \beta + \chi)} \quad . \tag{3.15}$$

$$\text{with } \beta = \frac{bP}{RT}, \ \chi = \frac{cP}{RT}, \ q = \frac{a}{bRT}$$

The volume translation parameter c can be determined through an inaccurate generalized function determined in [24] that is

$$c = -0.252 \frac{RT_c}{P_c} \left( 1.54482 - 0.4024 \right) \tag{3.16}$$

or if experimental data is available via the difference of experimental and calculated molar volumes at the reduced temperature $T_r = 0.7$ of the species i at 1 atm.

$$c_i = V_{exp,i} - V_{calc(PR-EoS),i} \tag{3.17}$$

Figure 2 shows that the liquid density can be predicted more accurate with the VTPR-EoS than with the PR EoS. In the VTPR results shown in Figure 2 using the translation parameter c at 1 atm to match the calculated VTPR EoS density to the density data of NIST. The improvement

is significant but it can also be seen that for pressures higher than 1 atm the c's would need to be fitted again to match the experimental data better.

The c's of selected components can be found in Appendix D - UGC VTPR Parameter.
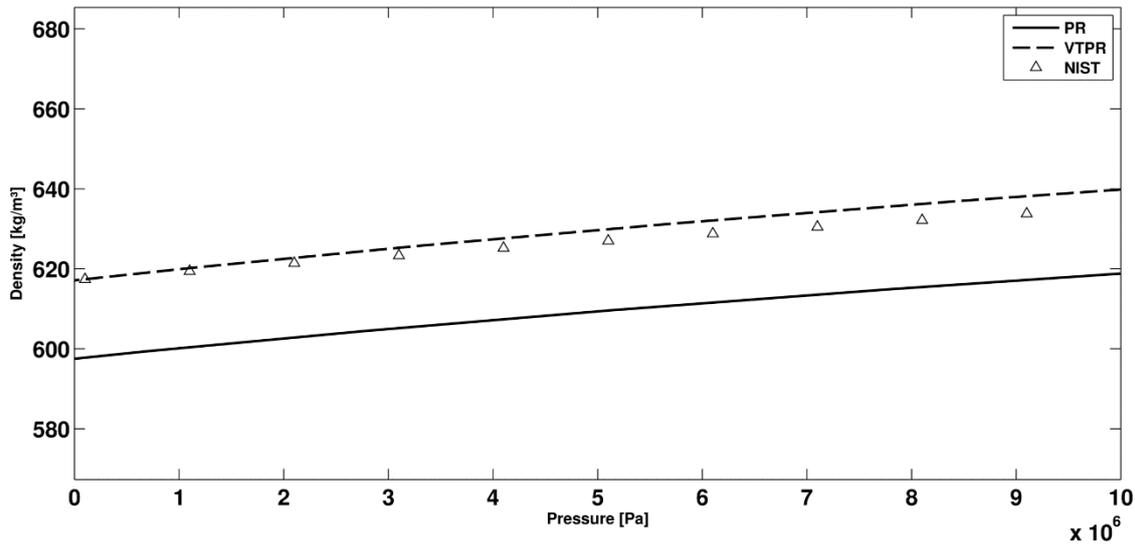


**Figure 2: Comparison of pressure dependency of density for n-decane at Tr = 0.7 for PR, VTPR and NIST experimental data** [17]**.**

## 3.1. Fugacity and Fugacity Coefficient

To derive the fugacity coefficient $\varphi$, which is defined as

$$\varphi = \frac{f}{P} \tag{3.18}$$

the molar Gibbs free energy can be used as a starting point. First the relation of the free Gibbs energy of an ideal gas and pressure can be calculated from

$$dg = vdP - sdT + \sum_i \left[ \frac{\partial g}{\partial n_i} \right] dn_i \tag{3.19}$$

with T , $n_i = \text{const.}$ and $v = \dfrac{RT}{P}$ (ideal gas) one finds

$$d\left(g^{iG}\right) = RTd\left(\ln P\right) . \tag{3.20}$$

To extend this expression for real fluids Lewis [9] introduced the fugacity. This yields the following relation

$$d(g) = RTd(\ln f)$$ (3.21)

with $g$ as the molar free Gibbs energy of a real fluid, f as the fugacity.

This allows the calculation of the fugacity coefficient at any pressure. Combining Eq. (3.20) and Eq.(3.21) performing an integration results in

$$g - g_0 - \left(g^{iG} - g_0^{iG}\right) = RT\ln\left(\frac{f}{f'}\right) - RT\ln\left(\frac{P}{P'}\right) = RT\ln\left(\frac{P'f}{f'P}\right)$$ (3.22)

with $g_0 = g_0^{iG}$ and $f' = P'$

$$\left(g - g^{iG}\right)_{P,T,n_{i\neq j}} = RT\ln\frac{f}{P} = RT\ln\varphi$$ (3.23)

Equation (3.23) allows us to determine the needed fugacity coefficient $\varphi$ for the VLE calculation. The LHS of Eq. (3.23) is called the residual function of the free Gibbs energy and is the difference between real and ideal Gibbs energy.

The relationship of Eq.(3.21) with (3.19) lead to the pressure dependency of the fugacity

$$\left(\frac{d\ln(f)}{dP}\right)_T = \frac{v}{RT}$$ (3.24)

$$\int_{f'}^{f} d(\ln(f)) = \frac{1}{RT}\int_{P'}^{P} vdP$$ (3.25)

$$\ln\frac{f}{f'} = \frac{1}{RT}\int_{P'}^{P} vdP$$ (3.26)

Further analogous for the ideal gas

$$\left(\frac{d\ln(P)}{dP}\right)_T = \frac{v}{RT}$$ (3.27)

with $v = \dfrac{RT}{P}$ yields

$$\int_{P'}^{P} d(\ln(P)) = \int_{P'}^{P} \frac{1}{P} dP \qquad (3.28)$$

$$\ln \frac{P}{P'} = \int_{P'}^{P} \frac{1}{P} dP \qquad (3.29)$$

Using Eq.(3.26) and Eq.(3.29) with Eq.(3.30) and $f' = P' \to 0$ leads us to the volume explicit form of $\ln \varphi$

$$\ln \varphi = \ln \frac{f}{f'} - \ln \frac{P}{P'} \qquad (3.30)$$

$$\ln \varphi = \frac{1}{RT} \int_{0}^{P} \left( v - \frac{RT}{P} \right) dP \qquad (3.31)$$

or the pressure explicit form of the fugacity coefficient

$$\ln \varphi = z - 1 - \ln z + \frac{1}{RT} \int_{\infty}^{v} \left( \frac{RT}{v} - P \right) dv . \qquad (3.32)$$

A graphical representation of the fugacity coefficient is shown in Figure 3. According to Eq.(3.31) the dashed area represents the logarithm of the fugacity coefficient respectively the difference of the real and ideal Gibbs energy over an integral of P' to P.
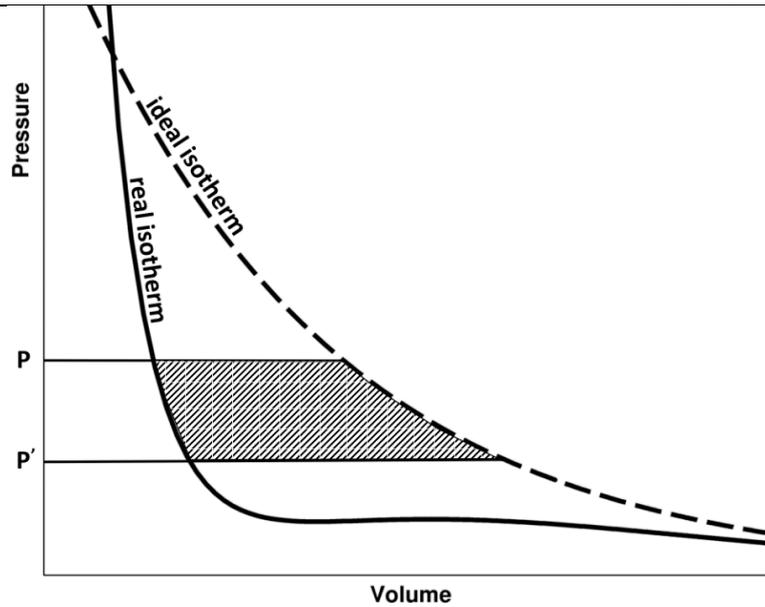
**Figure 3: Fugacity calculation with the help of P-V isotherms. The dashed isotherm represents the ideal gas law P=RT/V and the continuous line the isotherm of a real gas equation of a non-ideal gas (carbon dioxide).**

Equation (3.32) in combination with a pressure explicit EoS as given in (3.6) can be used to calculate the fugacity coefficient for pure species

$$\ln\frac{f}{P} = \ln\varphi = z - 1 - \ln\left(z - \beta + \chi\right) - qI \tag{3.33}$$

$$\text{with } \beta = \frac{bP}{RT}, \ \chi = \frac{cP}{RT}, \ q = \frac{a}{bRT}$$

and

$$I = \int_{\infty}^{v} \frac{vdv}{(v + \varepsilon b + c)(v + \sigma b + c)} \begin{cases} \varepsilon \neq \sigma & I = \frac{1}{\sigma - \varepsilon}\ln\frac{z + \sigma\beta + \chi}{z + \varepsilon\beta + \chi} \\ \varepsilon = \sigma \ \& \ c = 0 & I = \frac{\beta}{z + \varepsilon\beta} \end{cases}$$

The compressibility factor $z$ to be used in Eq.(3.33) can be calculated by solving the cubic equation of state in z

$$z^3 + Az^2 + Bz + C = 0 \tag{3.34}$$

with

$$A = \left( \beta(\sigma + \varepsilon - 1) - 1 + 3\chi \right)$$

$$B = \left[ \beta^2(\sigma\varepsilon - (\sigma + \varepsilon)) - \beta\left(\sigma + \varepsilon - q - \chi(2\sigma + 2\varepsilon - 2)\right) + \chi(3\chi - 2) \right]$$

$$C = \left[ -\beta^2\left(\sigma\varepsilon\beta + \sigma\varepsilon + q + \chi(\varepsilon + \sigma - \varepsilon\sigma)\right) + \beta\left(\chi(q - \varepsilon - \sigma) + \chi^2(\sigma + \varepsilon - 1)\right) + \chi^3 - \chi^2 \right]$$

and the parameters $q$, $\sigma$, $\varepsilon$, $\chi$ specific for the EoS used (seen in Table 1).

Equation (3.34) can be solved through the analytical method of Cardano or with a faster more accurate numerical root finding method proposed by Deiters [25]. For this thesis both methods were used. First Cardano's method was applied to find a starting value for the then used numerical root finding method.

While Eq.(3.34) stays the same for multi-component mixtures and pure species, the fugacity coefficient calculation Eq.(3.33) does change and has to be derived separately for each mixing rule (see chapter 5).

# 4. Activity Coefficient Models

To calculate equilibrium conditions using Eq. (2.12) one needs to describe activity coefficients. The activity coefficients are derived from the molar excess Gibbs free energy $g^E$. According to [8] the excess chemical potential of a component in a mixture is related to the activity coefficient $\gamma_i$, by

$$\mu_i^E = \overline{g}_i^E = RT \ln \gamma_i \ . \tag{4.1}$$

The sum of Eq.(4.1) over all components of a mixture leads to the molar excess Gibbs energy

$$g^E = \sum_i x_i \mu_i^E = RT \sum_i x_i \ln \gamma_i \ . \tag{4.2}$$

The simplest nontrivial expression of the excess Gibbs energy for simple liquid mixtures (i.e. mixtures of molecules that are similar in size, shape, chemical nature) is the Two-Suffix Margules/Porter Equation [7]

$$g^E = Ax_1 x_2 \tag{4.3}$$

that meets the condition of

$$\begin{aligned} g^E &= 0 \text{ when } x_1 = 0 \\ g^E &= 0 \text{ when } x_2 = 0 \end{aligned} \tag{4.4}$$

with A as an empirical constant.

The activity coefficient can then be calculated using the partial derivative of $g^E$ with Eq.(4.3)

$$\overline{g}_i^E = RT \ln \gamma_1 = \left( \frac{\partial n_T g^E}{\partial n_i} \right)_{T,P,n_{i \neq j}} \Rightarrow \ln \gamma_1 = \frac{A}{RT} x_2^2 \text{ and } \ln \gamma_2 = \frac{A}{RT} x_1^2 \ . \tag{4.5}$$

Eq.(4.3) is the simplest case of a more general polynomial representation known as Redlich-Kister equation.

$$g^E = RTx_1 x_2 \left[ A + B(x_1 - x_2) + C(x_1 - x_2)^2 + ... \right] \tag{4.6}$$

Eq.(4.6) is written for a binary system but can be extended to a multicomponent system [26].

The development of semi-empirical (i.e. assigning rough physical meanings to the parameters used) activity coefficient models started with the Wohl expansion

$$
\begin{aligned}
\frac{g^E}{RT\left(x_1 q_1 + x_2 q_2\right)} &= 2a_{12}z_1 z_2 + 3a_{112}z_1^2 z_2 + 3a_{122}z_1 z_2^2 \\
&+ 4a_{1112}z_1^3 z_2 + 4a_{1222}z_1 z_2^3 + 6a_{1122}z_1^2 z_2^2 + ..
\end{aligned}
\tag{4.7}
$$

with $z_1 = \dfrac{x_1 q_1}{x_1 q_1 + x_2 q_2}$ and $z_2 = \dfrac{x_2 q_2}{x_1 q_1 + x_2 q_2}$. The q's are effective volumes and a's are interaction parameters. This leads to the van Laar Equation, Margules Equations, Scatchard-Hildebrand Equation and many more which are obtained by Wohl's formulation [7].

Three important practical equations cannot be obtained from the Wohl expansion [7]. These three models are the Wilson Equation, the Non Random Two Liquids Model (NRTL), and the Universal Quasi Chemical Model (UNIQUAC).

These models are based on molecular considerations with non-randomness parameters or/and interaction energies between molecules taking into account local compositions which are different from global mole fractions (see Figure 4).
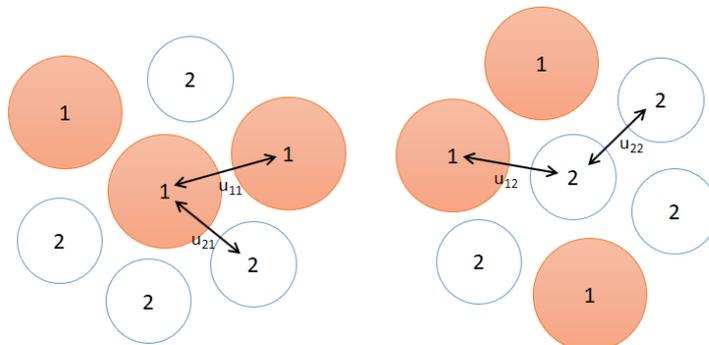


**Figure 4: Local Composition with binary interaction parameters**

For the Wilson and NRTL model only the pros and cons are mentioned [7].

Wilson:

+ can be applied to multi- component mixtures
+ two adjustable parameters per binary

+   good representation of many miscible mixtures

-   cannot indicate miscibility gaps

NRTL

+   can be applied to multi- component mixtures

+   can be applied to partly miscible mixtures

-   three adjustable parameters per binary

As the Universal Group Coefficient (UGC) method for the VLE calculation was used which is similar to UNIQUAC/UNIFAC, both models will be further described in detail in the following sections.

## 4.1. Universal Quasi Chemical Model (UNIQUAC)

The Universal Quasi Chemical (UNIQUAC) model is an extension to the quasi-chemical theory introduced by Guggenheim [27]. The extension renders it possible to calculate the activity coefficients (deviations from the ideal behavior) of mixtures whose molecules are different in size and shape (universal), unlike the original theory of Guggenheim which was only useable for small molecules of the same size [28].

The development of the UNIQAC model was motivated and got more popular because only two parameters instead of three parameters per binary pair (NRTL model) had to be fitted, in a time were experimental data were more scarce than today [7].

According to Eq.(4.5) the activity coefficients can be derived from the molar excess Gibbs energy. The calculation of the molar excess Gibbs energy is split into two parts

$$\frac{g^E}{RT} = \left( \frac{g^E}{RT} \right)_{combinatoral} + \left( \frac{g^E}{RT} \right)_{residual} \, . \qquad (4.8)$$

The combinatorial part of the molar excess Gibbs energy which accounts for the dominant entropic contribution by defining the composition and the size/shapes of molecules in the mixture is given as

$$\left(\frac{g^E}{RT}\right)_{combinatorial} = \sum_i x_i \ln\frac{\phi_i}{x_i} + \frac{\zeta}{2}\sum_i q_i x_i \ln\frac{\theta_i}{\phi_i} \tag{4.9}$$

and the residual excess Gibbs energy which describes the intermolecular forces by defining additional two adjustable binary interaction parameters is given as

$$\left(\frac{g^E}{RT}\right)_{residual} = -\sum_i q_i x_i \ln\left(\sum_j \theta_j \tau_{ji}\right). \tag{4.10}$$

Eq.(4.9) and (4.10) were derived by [28], where the average segment fraction $\phi$ and the average area fraction $\theta$ are calculated by

$$\phi_i = \frac{r_i x_i}{\sum_j r_j x_j} \tag{4.11}$$

$$\theta_i = \frac{q_i x_i}{\sum_j q_j x_j} \tag{4.12}$$

$q$ and $r$ are pure component structural parameters of surface respectively volume, $x$ stands for mole fraction, $\zeta$ as the coordination number which is set to 10 [28], $\tau_{ji}$ are binary adjustable parameters that are defined by

$$\tau_{ji} = \exp\left[-\left(\frac{u_{ji} - u_{ii}}{RT}\right)\right]. \tag{4.13}$$

It is seen from Equation (4.9) that only pure component data and no adjustable parameters are needed in the combinatorial term. The adjustable binary parameters used in the residual term, that is $\left(u_{ij} - u_{ii}\right)$ and $\left(u_{ji} - u_{jj}\right)$ with $u_{ij} = u_{ji}$, are fitted to experimental data (e.g. vapour-liquid and liquid-liquid equilibrium data).

Using a general relation between partial molar entities and molar state variables given by the Gibbs energy one gets for the excess chemical potential which is given by [29]

$$\mu_i^E = \left(\frac{\partial n_T g^E}{\partial n_i}\right)_{P,T,n_{i\neq j}} = g^E - \sum_{k\neq i}^N x_k \left(\frac{\partial g^E}{\partial x_k}\right)_{P,T,n_{i\neq j}} = RT \ln\gamma_i. \tag{4.14}$$

From this expression one finds

$$\ln \gamma_i = \frac{g^E}{RT} - \sum_{k \neq i}^{N} x_k \left( \frac{\partial \left( g^E / RT \right)}{\partial x_k} \right)_{P,T,n_{i \neq j}} . \tag{4.15}$$

Introducing (4.8) into (4.15) the activity coefficient for species i in a multicomponent mixture becomes after [28]

$$\ln \gamma_i = \ln \frac{\phi_i}{x_i} + \left( \frac{\zeta}{2} \right) q_i \ln \frac{\theta_i}{\phi_i} + l_i - \frac{\phi_i}{x_i} \sum_j x_j l_j - q_i \ln \left( \sum_j \theta_j \tau_{ji} \right) + q_i - q_i \sum_j \frac{\theta_j \tau_{ij}}{\sum_k \theta_k \tau_{kj}} \tag{4.16}$$

where

$$l_i = \left( \frac{\zeta}{2} \right) \left( r_i - q_i \right) - \left( r_i - 1 \right) . \tag{4.17}$$

## 4.2. Universal Functional-group Activity Coefficient Model (UNIFAC)

The model combines a functional-group concept with the UNIQUAC model resulting in the UNIversal Functional-group Activity Coefficient (UNIFAC) model. With the functional-group concept a molecule can be divided into functional-groups which can be seen in Figure 5.
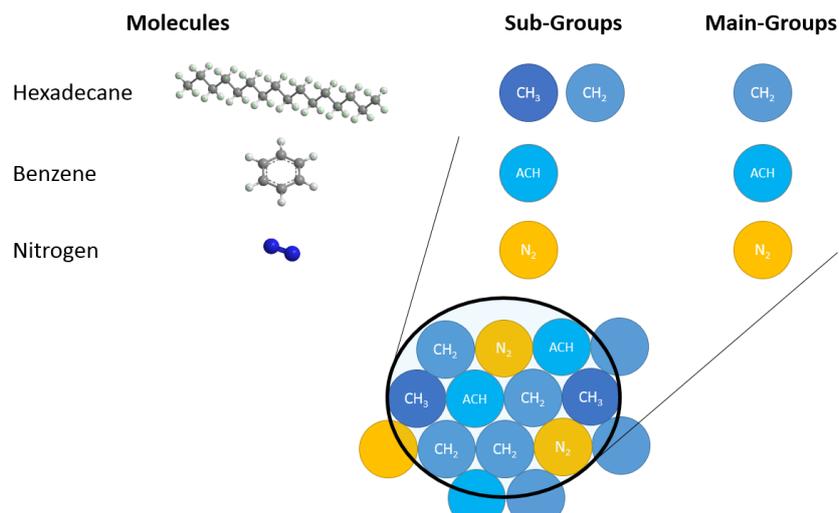


**Figure 5: The functional-group concept of the VTPR-UNIFAC model by the example of the components of hexadecane, benzene and nitrogen in a multi-component mixture.**

The combinatorial part of the activity coefficient is calculated in the same way as in UNIQUAC, but $r_i$ and $q_i$ occurring in Equations (4.11) and (4.12) must now be calculated by group volume and surface parameters, $R_k$ and $Q_k$, given by

$$r_i = \sum_k v_k^{(i)} R_k \text{ and } q_i = \sum_k v_k^{(i)} Q_k \tag{4.18}$$

where $v_k^{(i)}$, always an integer, is the number of sub-groups of type k in molecule i. The residual part of Equation (4.16) is replaced by the solution-of-groups concept [30]

$$\ln \gamma_i^{residual} = \sum_k^{all\ groups} v_k^{(i)} \left[ \ln \Gamma_k - \ln \Gamma_k^{(i)} \right] . \tag{4.19}$$

Where $\Gamma_k$ is the group residual activity coefficient and $\Gamma_k^{(i)}$ is the residual activity coefficient of group k in a reference solution containing only molecules of type i. Similar to the residual activity coefficient of the UNIQUAC model, the group activity coefficient $\Gamma_k$ can be found as

$$\Gamma_k = Q_k \left[ 1 - \ln \left( \sum_m \Theta_m \Psi_{mk} \right) - \sum_m \frac{\Theta_m \Psi_{km}}{\sum_n \Theta_n \Psi_{nm}} \right] \tag{4.20}$$

with $\Theta_m$ the area fraction of sub-group m

$$\Theta_m = \frac{Q_m X_m}{\sum_n Q_n X_n} \tag{4.21}$$

where $X_m$ is the fraction of sub-group m in the mixture given by

$$X_m = \frac{\sum_j v_m^{(i)} x_j}{\sum_j \sum_n v_n^{(i)} x_j} \tag{4.22}$$

The parameter $\Psi_{mn}$ contains the binary group interaction parameter $a_{mn}$ between functional groups n and m

$$\Psi_{mn} = \exp \left( -\frac{a_{mn}}{T} \right) . \tag{4.23}$$

The functional groups are called main groups and consist of one or more sub-groups. The interaction parameters are fitted almost exclusively to experimental data stored in the Dortmund Data Bank [31].

### 4.2.1. Modified UNIFAC (Do) / Universal Group Coefficient (UGC)

There are many modifications and extensions to the original UNIFAC model, however in this thesis only modifications and extensions of Gmehling et al. are used (modified UNIFAC(Dortmund) [32] and group- contribution equations of state, Predictive Soave-Redlich-Kwong (PSRK) [33] / Universal Group-Coefficient (UGC) VTPR EoS [24] ( see 5.3 Universal Group Contribution Volume Translated Peng Robinson Equation of State (UGC VTPR EoS) ).

Modifications were done to the combinatorial part of the activity coefficient

$$\ln \gamma_i^{combinatorial} = 1 - \phi_i' + \ln \phi_i' - 5q_i \left( 1 - \frac{\phi_i}{\theta_i} + \ln \frac{\phi_i}{\theta_i} \right) \tag{4.24}$$

$$\phi_i' = \frac{r_i^{3/4} x_i}{\sum_j r_j^{3/4} x_j} \tag{4.25}$$

and the residual part of the activity coefficient through temperature depended binary interaction parameters

$$\Psi_{mn} = \exp \left( -\left( \frac{a_{mn} + b_{mn} T + c_{mn} T^2}{T} \right) \right) \tag{4.26}$$

Further the group volume and surface parameters, $R_k$ and $Q_k$, are fitted together with the binary interaction parameters $(a_{mn}, b_{mn}, c_{mn})$ to experimental data.

In Figure 6 (a) the status of the year 2014 for the UGC VTPR EoS group interaction parameters matrix is seen and (b) the groups which were implemented are depicted. Of which were the main groups: CH2, ACH, ACCH2, OH, C3OH, H2O and N2 specifically used in the further presented VLE validation, single droplet, spray box and engine case studies. In Figure 6 empty regions mean that no interaction parameters are available (i.e. these combinations are not covered by the method yet), the blue regions mean that two interaction parameters are

available for $a_{mn}$ , the green regions mean that four interaction parameters are available for $a_{mn}$ , $b_{mn}$ and the orange regions mean that six interaction parameters are available for $a_{mn}$ , $b_{mn}$ and $c_{mn}$ .
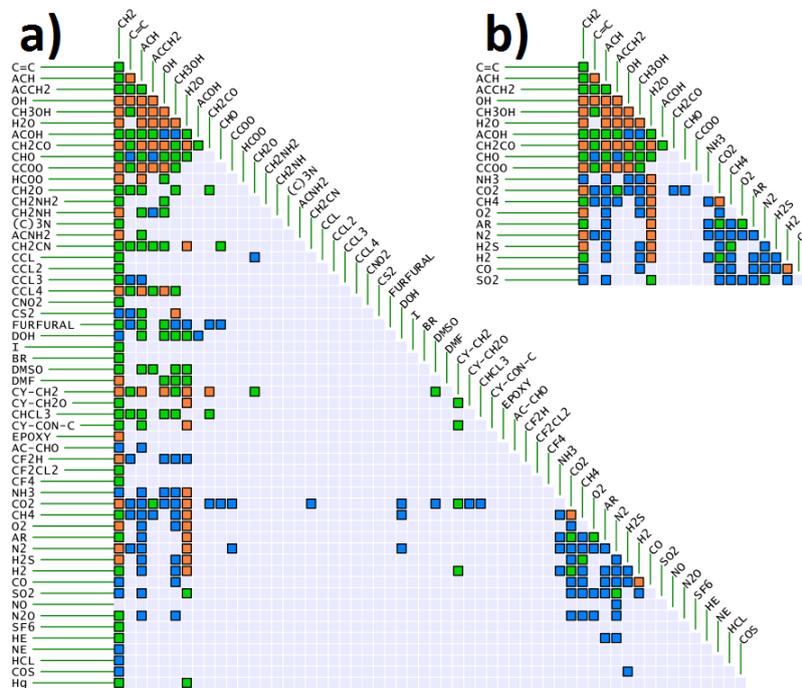


**Figure 6: (a) Group interaction matrix for the VTPR UGC-EoS** [34] **with (blue) two parameters, (green) four parameters,(orange) six parameters; (b) only specific components were used which represent a smaller matrix. All VTPR GC-EoS parameters for the used groups can be found in the appendix.**

For this thesis the UGC VTPR-Twu EoS, after validation with high pressure experimental data, was used to calculate the vapour-liquid equilibrium at the interface of the droplet.

The UGC VTPR EoS is still under further development to be used in a wide area of application as illustrated by Schmid et al [23] (Figure 7).

prediction of phase equilibria and excess properties (VLE, SLE, GLE, SCF,.., $h^E$, ..)

diffusional mass transfer ($\Delta a_i$, $\Delta f$, $\Delta \mu_i$ instead of $\Delta c_i$)

selection of refrigerants

prediction of thermo-dynamic properties (h, $\Delta h_v$, s, $\Delta h_R$(P), ..)

prediction of the fate of chemicals (bioaccumulation)

prediction of flash points of flammable liquid mixtures

description of reversible reactions

group contribution EOS VTPR ($\gamma_i$, $\varphi_i$, PVT, (X-X$^{id}$))

selection of working fluids for thermodynamic cycles

detection of separation problems, e.g. azeotropic points

construction of residue curves

selection of suitable solvents for separation processes, chemical processes, SCF, ..

design of separation columns ($N_{th}$,H)

consideration of the real behavior ($K_\gamma$, $K_\varphi$) on the chemical conversion

**Figure 7: The UGC-EoS has potential in many areas of process development** [23]

# 5. Mixing Rules

To describe multicomponent fluids with an equation of state, mixing rules are needed. The purpose of a mixing rule is to calculate EoS parameter a, b and c creating a pseudo pure component which is suitable to calculate mixture thermodynamic properties using the same type of equation of state as for the single components.

The first reasonable accurate mixing rule was the van der Waals one-fluid mixing rule but there are limitations using it especially for non-ideal mixtures. Thus efforts have been made to combine the advanced EoS (PR, SRK) with an activity coefficient model resulting in the so called $G^E$ -mixing rules. Typical representatives are the Huron-Vidal (HV) , Michelsen Huron-Vidal 1 (MHV1), Wong-Sandler (WS), Michelsen Huron-Vidal 2 (MHV2), Linear Combination of Vidal and Michelsen (LCVM) ( see [35], [36] for more details ). For the most recent and most accurate development of mixing rules the Predictive Soave-Redlich-Kwong (PSRK) and UGC VTPR have been derived by Gmehling et al [12] using the Dortmund Data Base.

Finally the UGC method was used in this thesis for the improved modelling of fuel droplet evaporation.

## 5.1. van der Waals Mixing Rule (vdW)

The van der Waals one-fluid mixing rule is used for the calculation of the mixture co- volume $b$ and the mixture attraction parameter $a$ .

$$b = \sum_i \sum_j x_i^{v,l} x_j^{v,l} b_{ij} \text{ with } b_{ij} = \frac{b_i + b_j}{2}(1 - l_{ij}) \tag{5.1}$$

$$a = \sum_i \sum_j x_i^{v,l} x_j^{v,l} a_{ij} \text{ with } a_{ij} = \sqrt{a_i a_j}(1 - k_{ij}) \tag{5.2}$$

Here $a_i$ , $b_i$ denotes the parameters of the respective components ( see 3 Equations of State (EoS) ) with $l_{ij}$ and $k_{ij}$ as the binary interaction parameters which can either be fitted to experimental data or can be found by other means for most hydrocarbons (e.g. correlations, group contribution methods [37]).

As the simplest mixing rule it is typically used with $l_{ij} = 0$ reducing the mixing of the co-volume to a linear combination, $b = \sum_i x_i^{v,l} b_i$ which is called the classical combining mixing rules [36].

Ultimately the classical combining rules are applicable for non-polar/non-polar, or non-polar/supercritical gas mixtures but fail/become inaccurate for non-ideal mixture VLE calculations. As the binary interaction parameter for most non-ideal mixtures is strongly temperature dependent the use of the vdW mixing rules becomes impractical.

## 5.2. Linear Combination of the Vidal and Michelsen Rules (LCVM)

The LCVM belongs to the $G^E$ mixing rules. It is the most widely used mixing rule, being the oldest successful model for size-asymmetric mixtures. It was proposed as a linear combination of the Huron-Vidal and the Michelsen $G^E$ mixing rule [38]:

$$q = \lambda q_V + (1 - \lambda) q_M \text{ with } q = \frac{a}{bRT} \tag{5.3}$$

$$q_V = \frac{1}{C_V} \left( \frac{g^E}{RT} \right) + \sum_i x_i^{v,l} q_i \tag{5.4}$$

$$q_M = \frac{1}{C_M} \left[ \left( \frac{g^E}{RT} \right) + \sum_i x_i^{v,l} \ln \frac{b}{b_i} \right] + \sum_i x_i^{v,l} q_i \tag{5.5}$$

$$a = bRT \left[ \left( \frac{\lambda}{C_V} + \frac{1-\lambda}{C_M} \right) \left( \frac{g^E}{RT} \right) + \frac{1-\lambda}{C_M} \sum_i x_i^{v,l} \ln \left( \frac{b}{b_i} \right) + \sum_i x_i^{v,l} q_i \right] \tag{5.6}$$

$C_V$ and $C_M$ are EoS specific constants, the co-volume parameter uses the linear mixing rule $b = \sum_i x_i^{v,l} b_i$ and the parameter $\lambda = 0.36$ ( which is specific to the original UNIFAC [38]) was fitted from asymmetric mixture data.

As already stated the mixing rule is preferably applied to asymmetric mixtures containing non-polar/polar components at high pressures but as the UNIFAC parameters contain no interaction parameters for supercritical gases like nitrogen it has not been used for droplet simulations in this thesis.

Further information on the LCVM mixing rule, can be found in the papers Boukouvalas et al. [38] and by Kontogeorgis et al. [36].

## 5.3. Universal Group Contribution Volume Translated Peng Robinson Equation of State (UGC VTPR EoS)

The UGC EoS- VTPR was initially derived using the Predictive Soave-Redlich-Kwong $G^E$ -mixing rule [12] reducing the deviations from experimental data further with the VTPR EoS. The mixing rule for the parameter a of the VTPR is set up as

$$\frac{a}{bRT} = \frac{1}{C_{UGC}} \left[ \frac{g^E}{RT} + \sum_i x_i^{v,l} \ln\left(\frac{b}{bi}\right) \right] + \sum_i x_i^{v,l} q_i \quad \text{with } q_i = \frac{a_i}{b_i RT} \quad . \tag{5.7}$$

As already seen in Eq.(4.8), the molar excess Gibbs energy is the sum of a combinatorial and a residual term.

$$g^E = g^E_{comb} + g^E_{res} \tag{5.8}$$

with

$$\frac{g^E_{comb}}{RT} = \sum_i x_i^{v,l} \ln\left(\frac{r_i}{\sum_j x_j^{v,l} r_j}\right) + 5 \sum_i x_i^{v,l} q_i \ln\left(\frac{\theta_i}{\phi_i}\right). \tag{5.9}$$

The assumptions made in [12]

$$\frac{r_i}{\sum_j x_j^{v,l} r_j} \cong \frac{b_i}{b} \quad \text{and} \quad 5 \sum_i x_i^{v,l} q_i \ln\frac{\theta_i}{\phi_i} << g^E_{res}$$

result in the elimination of the combinatorial excess Gibbs energy finally yielding for a

$$\frac{a}{b} = \sum_i x_i^{v,l} \frac{a_i}{b_i} + \frac{g^E_{res}}{C_{UGC}} \tag{5.10}$$

with $C_{UGC} = -0.53087$ [12]. The mixture co-volume parameter b is defined as

$$b = \sum_i \sum_j x_i^{v,l} x_j^{v,l} b_{ij} \tag{5.11}$$

with the cross correlation parameters

$$b_{ij} = \left( \frac{b_i^{3/4} + b_j^{3/4}}{2} \right)^{4/3} \tag{5.12}$$

and the volume translation parameter, which is needed for the VTPR EoS, is defined through

$$c = \sum_i x_i^{v,l} c_i \tag{5.13}$$

with $c_i$ calculated from Eq.(3.16) or (3.17).

A comparison between vdW1, LCVM and the UGC mixing rule in a Pxy diagram can be seen in Figure 8. For the dashed line the Soave version of PR-EoS is used with the van der Waals mixing rule. For the dotted line the Stryjek-Vera version of PR-EoS is used with the linear combination of Vidal and Michelsen mixing rule and for the solid line the Twu version of the VTPR-EoS is used with the universal group coefficient mixing rule. The triangles represent the experimental data. The results show that the Twu UGC VTPR EoS variant is closest to the experimental data.
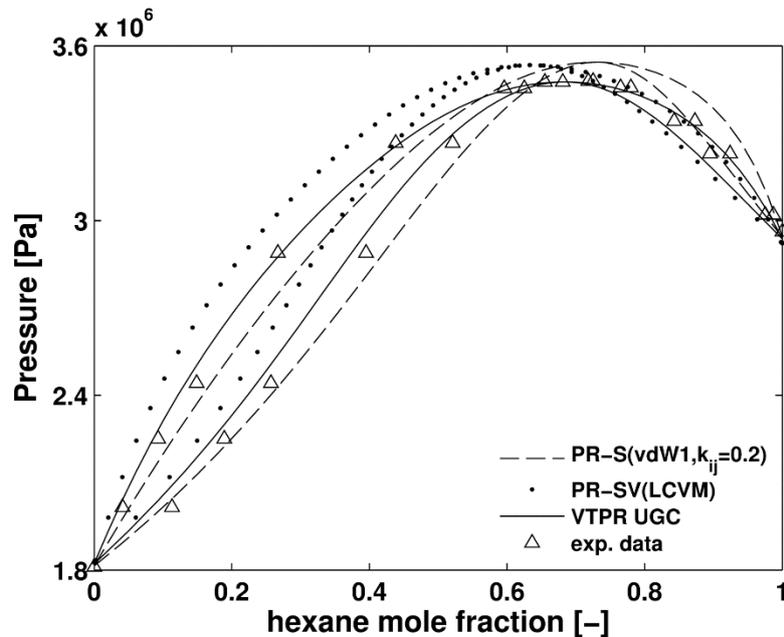


**Figure 8: Comparison between the three mixing rules (vdW1,LCVM,UGC) for the system of ethanol-hexane at 473.15 K with experimental data** [39]**.**

## 5.4. Fugacity Coefficient of a Species i in the Mixture

As mentioned in chapter 3.1 the form of the fugacity coefficient depends on the mixing rule used.

Eq.(5.14) and Eq.(5.15) show the volume-explicit and pressure-explicit formulations

$$\ln \varphi_i = \frac{1}{RT} \int_0^P \left[ \left( \frac{\partial v}{\partial n_i} \right)_{T,P,n_{j \neq i}} - \frac{RT}{P} \right] dP \qquad (5.14)$$

$$\ln \varphi_i = \frac{1}{RT} \int_\infty^v \left[ \frac{RT}{v} - \left( \frac{\partial P}{\partial n_i} \right)_{T,P,n_{j \neq i}} \right] dv - \ln z \ . \qquad (5.15)$$

Similar to Eq.(3.33) this allows us to calculate the fugacity coefficient of the mixture components with the general pressure explicit EoS to

$$\ln \varphi_i = \frac{b'}{b}(z-1) - \ln(z - \beta + \chi) - q \left( 1 + \frac{a'}{a} - \frac{b'}{b} \right) \ln \left( \frac{z + \sigma \beta + \chi}{z + \varepsilon \beta + \chi} \right) \qquad (5.16)$$

with $a'$ and $b'$ as the molar derivatives

$$b' = \left( \frac{\partial (nb)}{\partial n_i} \right)_{T,n_{j \neq i}} \quad \text{and} \quad a' = \left( \frac{\partial (na)}{\partial n_i} \right)_{T,n_{j \neq i}} \qquad (5.17)$$

E.g. $b'$ and $a'$ for classical mixing rules can be found in [8]

$$b'_{vdW1} = b_i \quad \text{and} \quad a'_{vdW1} = 2 \sum_j x_i^{v,l} a_{ij} - a \qquad (5.18)$$

With the other mixing rules more complex expressions result.

Combining Eq.(5.16) and Eq.(5.18) results in the fugacity coefficient equation for the general EoS with the classical mixing rules

$$\ln \varphi_i = \frac{b_i}{b}(z-1) - \ln(z-\beta+\chi) - q\left(2\sum_j x_i^{v,l} a_{ij} - \frac{b_i}{b}\right) \ln\left(\frac{z+\sigma\beta+\chi}{z+\varepsilon\beta+\chi}\right) \tag{5.19}$$

The fugacity coefficients for the remaining mixing rules are given in Appendix E - Mixture Fugacities.

## 6. VLE EoS Verification and Validation

Temperatures and pressures in an internal combustion engine change considerably during the compression cycle. Gas pressure rises depending on the load and the fuel used (diesel / gasoline) up to approximately 120 bar and 20 bar respectively. It is clear that a precise description of the vapour-liquid equilibrium at the interface is necessary for the evaporation algorithm used. This will be accomplished by applying the used UGC VTPR EoS suitable for high pressure vapour-liquid equilibrium calculations.

The vapour-liquid equilibrium calculations for the bubble and dew points are solved through a successive substitution algorithm which for the bubble point calculation consists of the following steps

1. Read the ambient temperature $T$ and the liquid composition $x_i$

2. Set estimates of the gas pressure $P$ and the vapour composition $y_i$ ( if available use the last P and y of the last calculation step )

3. Try to calculate the fugacity coefficients $\varphi_i^{v,l}$ and set a flag if successful or not successful respectively

4. Save the estimated vapour composition $y_i$ and gas pressure $P$, as well as the K-factor $K_i$ and $\sum_i K_i x_i$

5. Calculate the new pressure $P^+$ with a correction factor and an under-relaxation factor, with the correction factor set to $\sum_i K_i x_i$ and the under-relaxation factor set to unity by default

6. Try to calculate the fugacity coefficients $\varphi_i^{v,l}$ and a new K-factor $K_i^+$ setting a flag if successful or not successful respectively

   a. if it is successful continue with step 7

   b. if it is not successful and step 3 has been successful, continue with step 5 and the under-relaxation factor halved

   c. if it is not successful and a limit for the under-relaxation factor and a limit of inner loop iterations is reached leave the VLE calculation with a flag set indicating that no VLE could be calculated

7. Calculate a new vapour composition $y_i^+ = \dfrac{K_i^+ x_i}{\sum\limits_i K_i^+ x_i}$

8. While $|\Delta \sum\limits_i K_i^+ x_i| > \varepsilon_2$ go to step 6 and increase the inner loop count by one

9. If outer loop limit is reached, leave the VLE calculation with a flag set indicating that no VLE could be calculated

10. While $|\sum\limits_i K_i^+ x_i - 1| > \varepsilon_1$ go to step 4 and increase the outer loop count by one

11. Output the result of the successive substitution algorithm $P$ and $y_i$

A simplified flow- diagram of the algorithm is depicted in Figure 9.
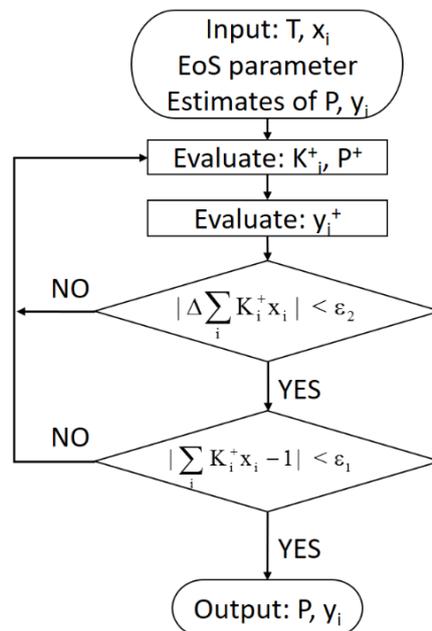


**Figure 9: Simplified flow chart of a successive substitution vapour-liquid equilibria algorithm calculating the pressure and vapour molar fractions of the mixture, with the mixture temperature and the composition of the liquid phase.**

The method of successive substitution is neither the most stable nor the fastest method that can be used for the calculation of the vapour-liquid equilibria as stated in [40]. There are also other numerical methods that can be used instead (e.g. Accelerated Successive Substitution, the Nelder-Mead Simplex or quasi-Newton methods). However, in the present application no problems have been encountered with ambient temperatures up to 1100 K and pressures up to 150 bar for the liquid components used. Thus this method

is regarded as sufficient for usage in ICE applications.

The UGC VTPR EoS, $\varphi - \varphi$ method, to calculate the vapour-liquid equilibrium was chosen after comparing the average deviations of pressure and vapour molar fraction for the experimental data using four different models as given in Table 4.

**Table 4: Models that are compared with experimental data**

| No. | VLE method | EoS | α(ω,T) | activity coef. model in liquid phase | mixing rule |
|---|---|---|---|---|---|
| 1 | γ-φ | - | - | UNIFAC | - |
| 2 | γ-φ | VTPR | Twu | UNIFAC | UGC ($g^E$) |
| 3 | φ-φ | PR | Stryjek-Vera | - | LCVM ($g^E$) |
| 4 | φ-φ | VTPR | Twu | - | UGC ($g^E$) |

The experimental data for the binary systems used are given in Table 5.

## 6.1. Model Comparisons

After the implementations of the fugacity coefficient and the mixture rule calculation algorithms VLEs were analyzed to detect the most accurate mixing rule and EoS. The systems in Table 5 were chosen as they were available in high pressure conditions and their components were already included in the thermophysical data base of AVL FIRE™.

**Table 5: High pressure/ temperature vapour-liquid equilibrium data found in literature to test the applicability of the used models by comparison of experimental with calculated data.**

| System (species 1+ species 2) | Temperature range [K] | Pressure range [MPa] | number of data points | Ref. |
|---|---|---|---|---|
| Methanol+ Benzene | 318.15-493.15 | 0.029-5.757 | 99 | [41] |
| Ethanol+ Pentane | 372.7-500 | 0.224-5.719 | 43 | [42] |
| Ethanol+ Heptane | 483.15-523.15 | 1.163-3.772 | 19 | [43] |
| Ethanol+ | 473.15-503.15 | 1.811-5.194 | 36 | [39] |

| | | | | |
|---|---|---|---|---|
| Hexane | | | | |
| Benzene+ Heptane | 333.15-488.15 | 0.158-1.777 | 68 | [44] |
| Hexane+ Hexadecane | 333.15-623 | 0.001-3.824 | 31 | [45][46] |
| Ethanol+ Water | 423.15-598.15 | 0.558-15.706 | 63 | [47] |

Table 6 presents the comparisons of the different models as given in Table 4. As evaluation criteria the average absolute deviation for pressures

$$\text{AAD(P)} = \frac{1}{\text{NP}} \sum_{i=1}^{\text{NP}} \text{ABS}\left( \frac{P_{i,calc} - P_{i,exp}}{P_{i,exp}} \right) \tag{6.1}$$

and the average deviation for vapour mole fractions

$$\Delta y = \frac{1}{\text{NP}} \sum_{i=1}^{\text{NP}} \text{ABS}\left( y_{i,calc} - y_{i,exp} \right) . \tag{6.2}$$

The number of data points, as seen in Table 5, is the sum of bubble and dew points that could be calculated using the experimental temperature and liquid component data as initial conditions for the bubble/ dew point calculations.

The average deviation of the UGC VTPR-Twu is overall the most accurate of the four models compared, with 1,54 % average pressure deviation. The LCVM PR-SV EoS is the second best model with 2,27 % deviation. The $\gamma - 1$ method follows next with a 11,67 % deviation while the $\gamma - \varphi$ approach which becomes very unstable with higher temperatures (i.e. failing the VLE calculation) reaching 29.73 % deviation. The reason for the unstable behavior is unclear but it is indicated in [19] that it is the result of using two different models to describe the liquid and vapour phase respectively. The LCVM PR-SV EoS yields increasing accuracy with rising pressure for most of the examined systems. The accuracy of the UNIFAC approach generally decreases with rising pressure especially for the calculated bubble points.

**Table 6: Comparisons of deviations for pressure and vapour mole fraction for the VLE calculation models**

| Temperature | AAD(P)% | | | | Δy*100 | | | | |
|---|---|---|---|---|---|---|---|---|---|
| | VTPR (Twu) UGC | PR(SV) LCVM | γ-φ ( UNIFAC ) | γ-1 ( UNIFAC ) | VTPR (Twu) UGC | PR(SV) LCVM | γ-φ ( UNIFAC ) | γ-1 ( UNIFAC ) | Data Points |
| [K] | | | | | | | | | |
| **Polar/Non-Polar** | | | | | | | | | |
| Methanol+Benzene | | | | | | | | | |
| 318.15 | 2.3% | 3.8% | 1.2% | 1.4% | 0.70 | 1.59 | 0.88 | 0.88 | 33 |
| 363.15 | 2.8% | 2.2% | 4.8% | 3.0% | 2.26 | 2.05 | 1.59 | 1.37 | 6 |
| 393.15 | 1.4% | 1.5% | 8.9% | 5.9% | 1.09 | 1.09 | 3.35 | 3.04 | 10 |
| 413.15 | 1.8% | 2.4% | 12.7% | 8.7% | 1.39 | 1.62 | 4.44 | 4.61 | 10 |
| 433.15 | 1.3% | 2.8% | 15.4% | 10.4% | 1.75 | 1.41 | 5.05 | 5.68 | 10 |
| 453.15 | 0.8% | 4.4% | 20.6% | 13.6% | 1.79 | 2.25 | 6.42 | 7.66 | 10 |
| 473.15 | 1.4% | 4.3% | 72.2% | 14.2% | 2.76 | 2.12 | 8.57 | 8.71 | 10 |
| 493.15 | 1.1% | 5.4% | 76.5% | 14.8% | 3.63 | 3.34 | 8.82 | 8.52 | 10 |
| | | | | | | | | | |
| System Average | 1.62% | 3.35% | 26.53% | 9.01% | 1.92 | 1.93 | 4.89 | 5.06 | |
| Ethanol+ Pentane | | | | | | | | | |
| 372.7 | 2.3% | 4.9% | 2.8% | 1.4% | 0.96 | 1.71 | 1.02 | 1.12 | 10 |
| 397.7 | 2.1% | 3.6% | 5.5% | 1.9% | 1.28 | 1.81 | 2.21 | 2.61 | 12 |
| 422.6 | 2.2% | 3.1% | 9.7% | 2.6% | 0.55 | 0.99 | 3.31 | 4.38 | 11 |
| 465.4 | 2.2% | 3.1% | 9.7% | 2.6% | 0.31 | 0.07 | 5.11 | 7.32 | 7 |
| 500 | 1.4% | 1.6% | 52.6% | 4.8% | 0.24 | 0.23 | 4.98 | 10.14 | 3 |
| | | | | | | | | | |
| System Average | 2.02% | 3.25% | 16.07% | 2.64% | 0.67 | 0.96 | 3.33 | 5.12 | |
| Ethanol+Heptane | | | | | | | | | |
| 483.15 | 0.8% | 2.8% | 82.0% | 13.6% | 2.33 | 2.42 | 6.64 | 10.90 | 12 |
| 508.15 | 0.9% | 3.0% | 62.7% | 18.8% | 0.74 | 0.91 | 6.57 | 15.26 | 5 |
| 523.15 | 1.2% | 3.5% | 88.6% | 50.8% | 0.05 | 0.55 | 17.08 | 34.91 | 2 |

| | | | | | | | | | |
|---|---|---|---|---|---|---|---|---|---|
| System Average | 0.95% | 3.12% | 77.75% | 27.73% | 1.04 | 1.30 | 10.09 | 20.36 | |
| Ethanol+Hexane | | | | | | | | | |
| 473.15 | 0.7% | 2.9% | 72.4% | 9.2% | 0.91 | 1.50 | 4.75 | 8.37 | 14 |
| 483.15 | 0.6% | 2.2% | 69.2% | 9.9% | 1.28 | 0.91 | 4.81 | 9.20 | 11 |
| 493.15 | 0.2% | 1.2% | 57.7% | 11.9% | 0.58 | 0.87 | 9.19 | 13.78 | 6 |
| 503.15 | 0.1% | 0.1% | 24.4% | 8.7% | 0.11 | 0.08 | 6.14 | 10.38 | 5 |
| | | | | | | | | | |
| System Average | 0.40% | 1.59% | 55.93% | 9.92% | 0.72 | 0.84 | 6.22 | 10.43 | |
| **Polar / Non-Polar Av.** | **1.25%** | **2.83%** | **44.07%** | **12.33%** | **1.09** | **1.26** | **6.13** | **10.24** | **197** |
| **Non-Polar/Non-Polar** | | | | | | | | | |
| Benzene+Heptane | | | | | | | | | |
| 333.15 | 0.3% | 1.6% | 1.2% | 1.2% | 0.34 | 0.50 | 0.21 | 0.07 | 31 |
| 383.15 | 1.3% | 0.7% | 1.2% | 1.0% | 0.71 | 0.95 | 1.49 | 1.99 | 9 |
| 413.15 | 1.3% | 0.5% | 2.0% | 1.5% | 0.29 | 0.65 | 1.41 | 1.90 | 9 |
| 443.15 | 0.4% | 2.9% | 4.1% | 3.2% | 0.63 | 0.71 | 1.50 | 2.17 | 10 |
| 488.15 | 1.2% | 2.9% | 2.8% | 1.6% | 0.85 | 0.57 | 1.68 | 2.55 | 9 |
| | | | | | | | | | |
| System Average | 0.89% | 1.73% | 2.25% | 1.71% | 0.56 | 0.68 | 1.26 | 1.74 | |
| Hexane+Hexadecane | | | | | | | | | |
| 333.15 | 1.4% | 1.5% | 11.3% | 9.6% | * | * | * | * | 10 |
| 472.3 | 1.2% | 0.9% | 4.7% | 6.9% | 0.02 | 0.04 | 0.07 | 0.36 | 8 |
| 572.5 | 3.4% | 5.0% | 6.6% | 31.4% | 0.17 | 0.18 | 3.55 | 8.14 | 7 |
| 623 | 4.4% | 6.5% | 32.7% | 57.4% | 0.51 | 0.60 | 3.98 | 18.29 | 6 |
| | | | | | | | | | |
| System Average | 2.59% | 3.46% | 13.85% | 26.32% | 0.23 | 0.28 | 2.53 | 8.93 | |
| **Non-Polar / Non-Polar Av.** | **1.74%** | **2.59%** | **8.05%** | **14.02%** | **0.40** | **0.48** | **1.89** | **5.33** | **99** |

| Polar/Polar Ethanol+Water | | | | | | | | | |
|---|---|---|---|---|---|---|---|---|---|
| 423.15 | 1.5% | 2.7% | 5.2% | 4.6% | 0.54 | 1.62 | 1.56 | 2.16 | 17 |
| 473.15 | 1.1% | 2.2% | 8.7% | 6.8% | 0.30 | 1.09 | 3.32 | 4.83 | 17 |
| 523.15 | 1.1% | 0.9% | 48.8% | 7.7% | 0.41 | 0.60 | 7.26 | 5.42 | 17 |
| 573.15 | 1.9% | 0.6% | 64.5% | 11.2% | 2.25 | 2.21 | 4.95 | 12.79 | 7 |
| 598.15 | 2.6% | 0.5% | 58.1% | 13.0% | 0.83 | 0.29 | 4.06 | 15.53 | 5 |
| | | | | | | | | | |
| System Average | 1.64% | 1.39% | 37.06% | 8.67% | 0.87 | 1.16 | 4.23 | 8.15 | |
| **Polar / Polar Average** | **1.64%** | **1.39%** | **37.06%** | **8.67%** | **0.87** | **1.16** | **4.23** | **8.15** | **63** |
| | | | | | | | | | |
| **Average** | **1.54%** | **2.27%** | **29.73%** | **11.67%** | **0.79** | **0.97** | **4.09** | **7.91** | **359** |

*no experimental data was found

In the next section (6.2 Binary Mixtures) a few figures are presented to depict the differences between the chosen UGC VTPR Twu EoS and the already used UNIFAC model.

## 6.2. Binary Mixtures

The isothermal VLE of a binary mixture in a Pxy diagram is characterized by a dew point line and a bubble point line which limit the abutting vapour, liquid and vapour-liquid regions (see Figure 10).
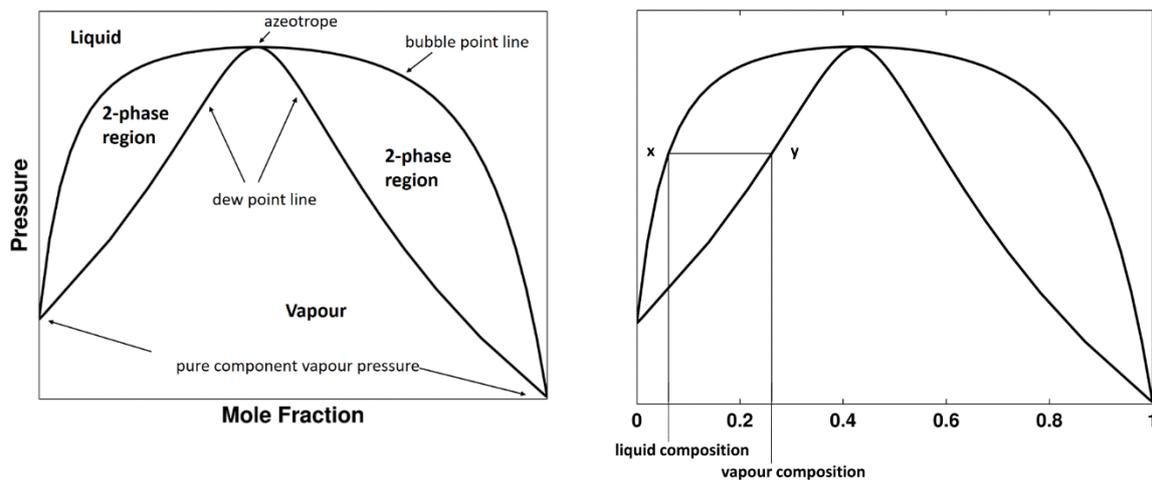


**Figure 10: Pxy diagram of a binary system (to the left); determining the vapour composition in equilibrium with the liquid composition (to the right)**

The dew point line represents the dew pressures and the bubble point line represents the bubble pressures for all possible mole fractions of the mixture. The limits of the diagram are the pure component vapour pressures. To determine the mole fraction in equilibrium in the vapour phase for a liquid composition x in saturated conditions, an isobaric line is drawn connecting the dew and bubble point line. For a given liquid molar fraction and temperature there is a unique solution of pressure and vapour molar fractions. The azeotrope that is due to the non-ideality of the mixture which is defined by identical composition of the liquid and the vapour phase.

The experimental vapour-liquid equilibrium data of the binary systems presented in Table 5 are shown in comparison with the UGC VTPR Twu EoS, abbreviated as VTPR UGC and UNIFAC model, abbreviated as UNIFAC, in Figure 11 to Figure 15.

Figure 11 shows the system of benzene-heptane that exhibits nearly ideal behavior (i.e. following Raoult-Dalton's law). For the low temperature of 333.15 K both models, the

UGC VTPR Twu EoS and UNIFAC, reproduce the experimental data well. Calculating the high temperature case and with pressure risen to approximately 6 - 9 bar the UNIFAC model clearly deviates from the experimental data with its bubble and dew points.
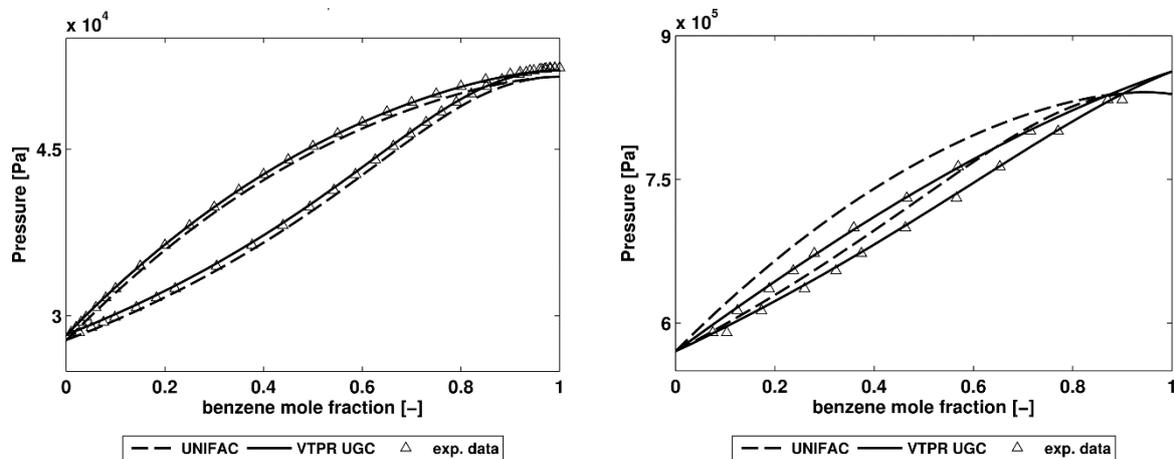


**Figure 11: Pxy diagram for an isothermal binary system of benzene-heptane. (to the left) 333.15K (to the right) 443.15K.**

Figure 12 shows the system of methanol-benzene, that exhibits non-ideal behavior (i.e. not following Raoult-Dalton's law) showing an azeotrope. At 318.15 K the UNIFAC model surpasses the UGC VTPR Twu EoS in accuracy. With increased temperatures and pressures risen to approximately 20-60 bar, the UNIFAC approach overpredicts the pressure for the bubble point line. It is interesting to note that the dew point line of the UNIFAC method reproduces the experimental data more accurately over a limited range of variable binary composition but is overall less accurate.
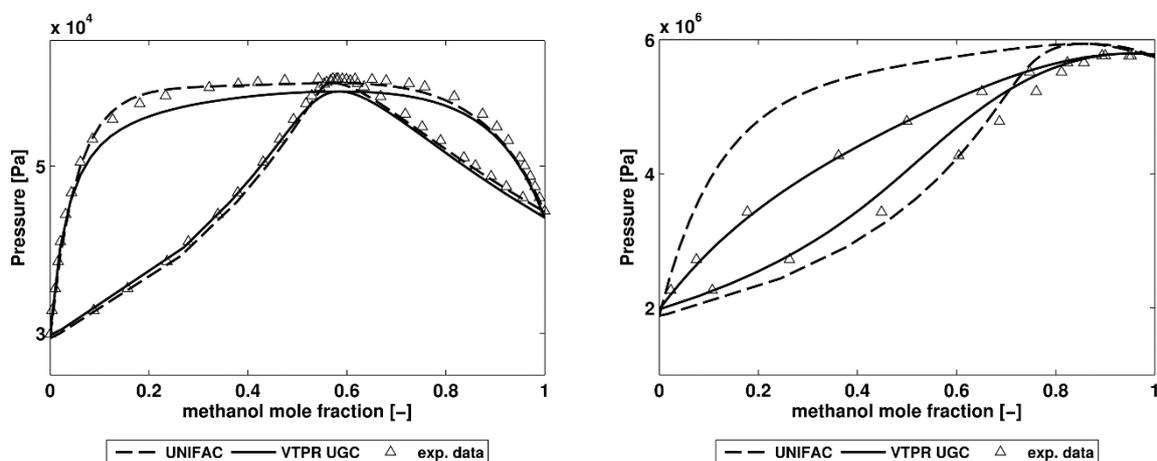


**Figure 12: Pxy diagram for an isothermal binary system of methanol-benzene. (to the left) 318.15 K (to the right) 493.15 K.**

Figure 13 shows the system of pentane-ethanol deviating considerably from ideal behavior. Both the UNIFAC method and the UGC VTPR Twu EoS provide an accurate representation of the experimental data at 372.7 K. With 500 K and pentane in an overcritical state the mixture reaches its critical state with a specific mole fraction of pentane of about 0.15 mole fraction. We see that the UNIFAC approach is unable to predict the change to the critical state of the mixture. Both dew point line and the bubble point line are over- / under predicted respectively.
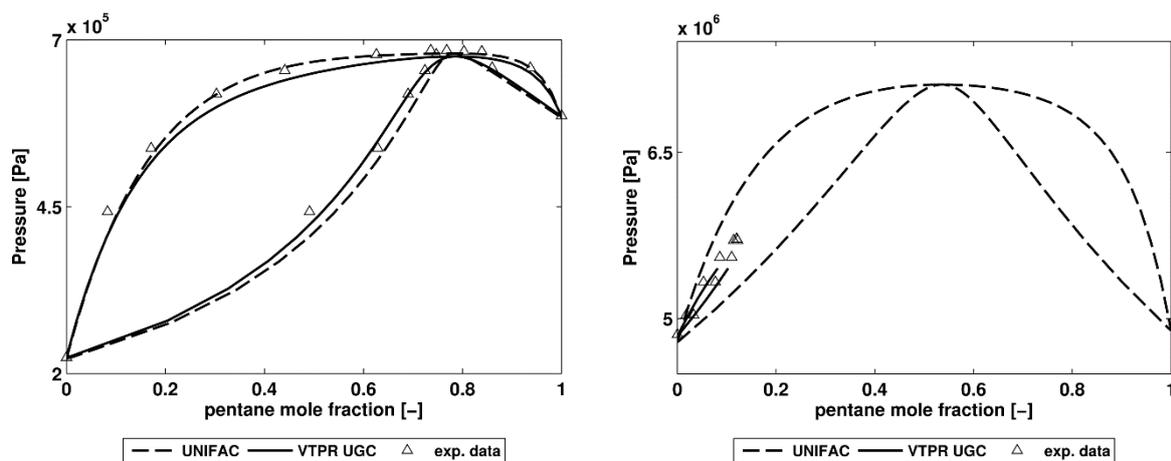


**Figure 13: Pxy diagram for an isothermal binary system of pentane-ethanol. (to the left) 372.7 K (to the right) 500 K.**

If the two components are very asymmetric in size a characteristic form for the binary Pxy bubble-/dew- line is encountered as seen in Figure 14 for the system of hexane-hexadecane. We can see the good agreement between calculated and experimental data for the UNIFAC model, as well as for the UGC VTPR Twu EoS at the temperature of 333.15 K.
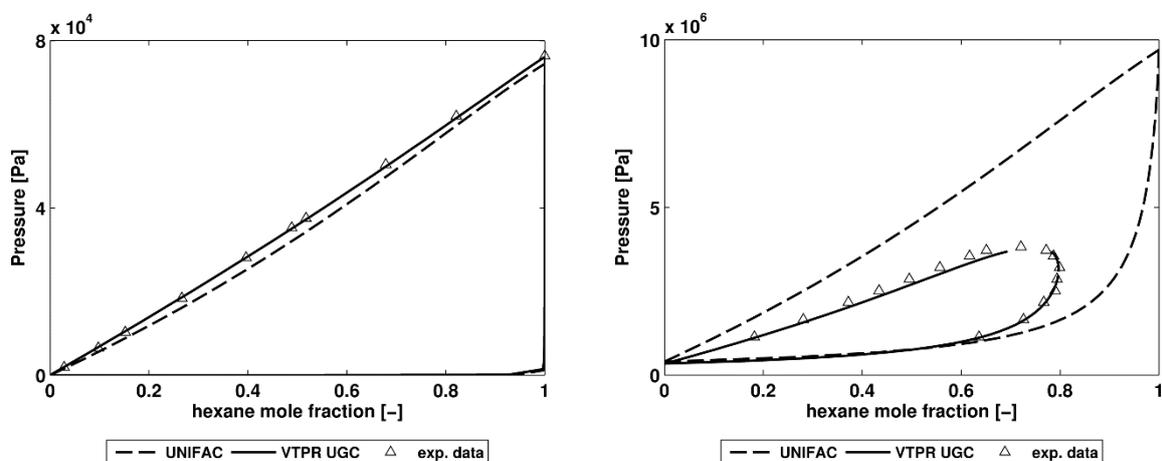


**Figure 14: Pxy diagram for an isothermal binary system of hexane-hexadecane. (to the left) 333.15 K (to the right) 623 K.**

Rising the temperature to 623 K results in hexane becoming overcritical, we again see the inability of the UNIFAC approach to predict critical mixture behavior. Whereas the UGC VTPR Twu represents the experimental data with good accuracy. It is interesting to note again that the dew line of the UNIFAC approach matches that of the UGC VTPR Twu over 2/3 of the variable binary composition.

Figure 15 depicts on the left hand side the system ethanol-hexane and on the right hand side the system ethanol-water. In both cases the UGC VTPR Twu surpasses the UNIFAC approach in reproducing the experimental data.
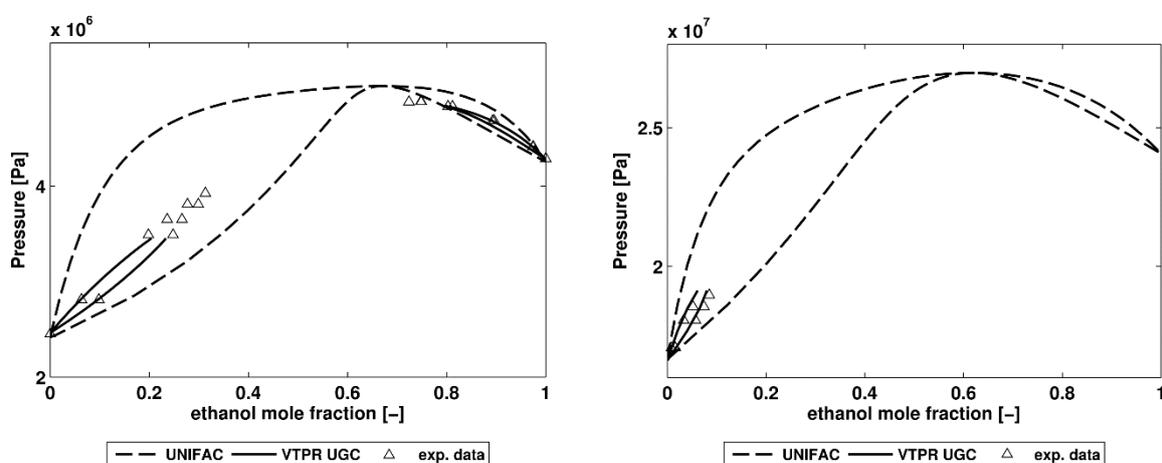


**Figure 15: (to the left) Pxy diagram for the binary system ethanol-hexane at 493.15 K. (to the right) Pxy diagram for the binary system ethanol-water at 623 K.**

Overall it can be said that due to the non-ideality of the vapour-phase at higher pressures (i.e. pressures higher than 5 to 10 bar) the UNIFAC approach strongly deviates from the experimental data in most of the examined systems. But in general it must be said that "low" or "high" pressure is dependent on the composition and temperature of the mixture [19].

## 6.3. Ternary Mixtures

A ternary mixture consist of three individual components. The usual way to visualize a ternary mixture is to use a ternary diagram. In Figure 16 a) b) c) a ternary 2D diagram is shown. With a) b) depicting a ternary mixture of A, B and C. The corners of a ternary diagram represent the pure components A, B and C respectively. By moving farther away from a corner the fraction of the associated component decreases. An example is shown in in Figure 16 c) with the

system Benzene-Ethanol-Heptane depicted. The mixture composition is marked as the black circle which reads $x_{Benzene}^{v,l} = 0.2$ , $x_{Ethanol}^{v,l} = 0.5$ and $x_{Heptane}^{v,l} = 0.3$ .



(a)

(b)



c)
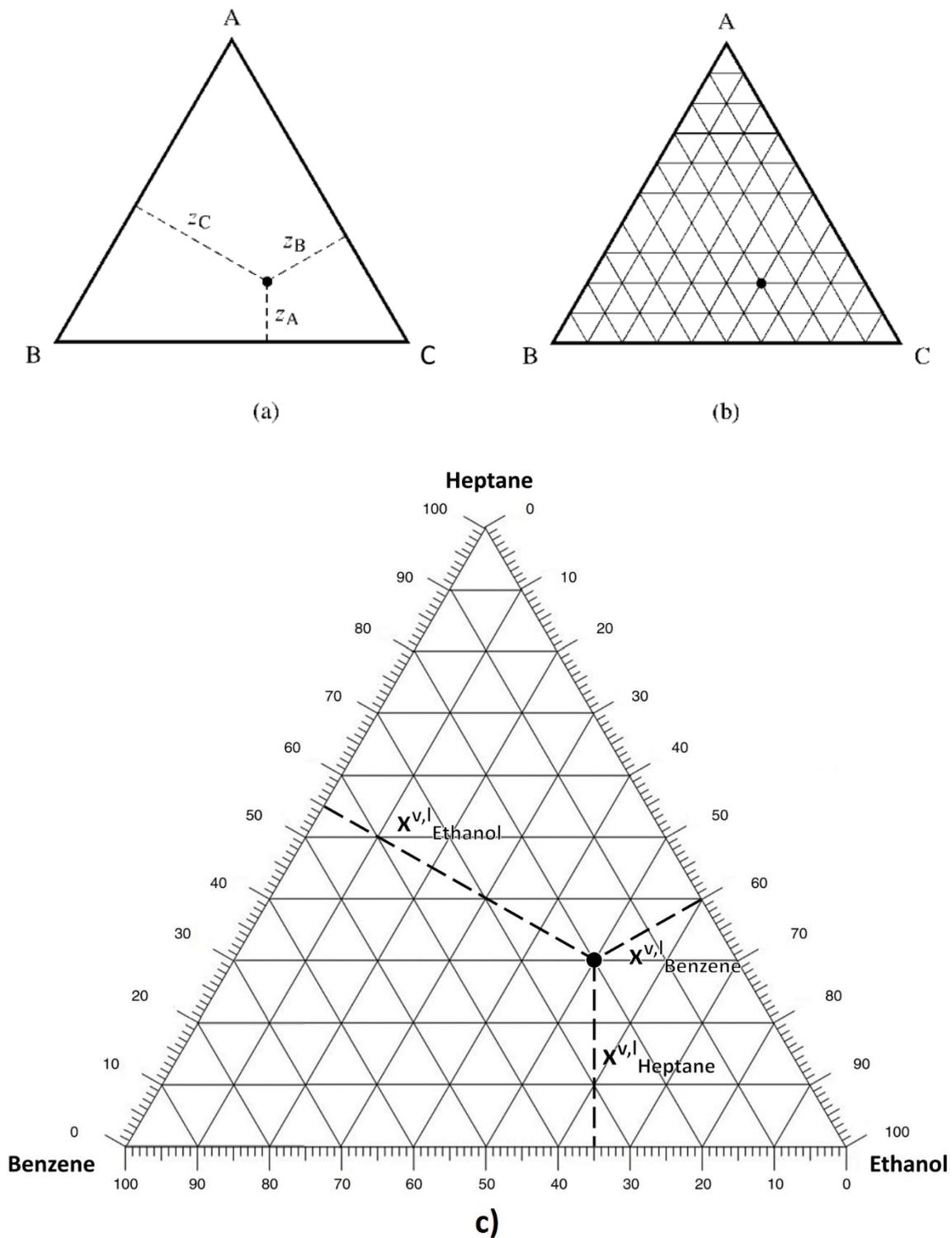
**Figure 16: a) b) Basic ternary diagrams to determine the fractions of the individual components in a Benzene-Ethanol-Heptane system. c) Example of a ternary mixture.** [48].

Adding an additional z- axis that reads pressure (isothermal VLE) or temperature (isobaric VLE) for the bubble or dew points of the mixture, a 3D ternary diagram can be constructed.
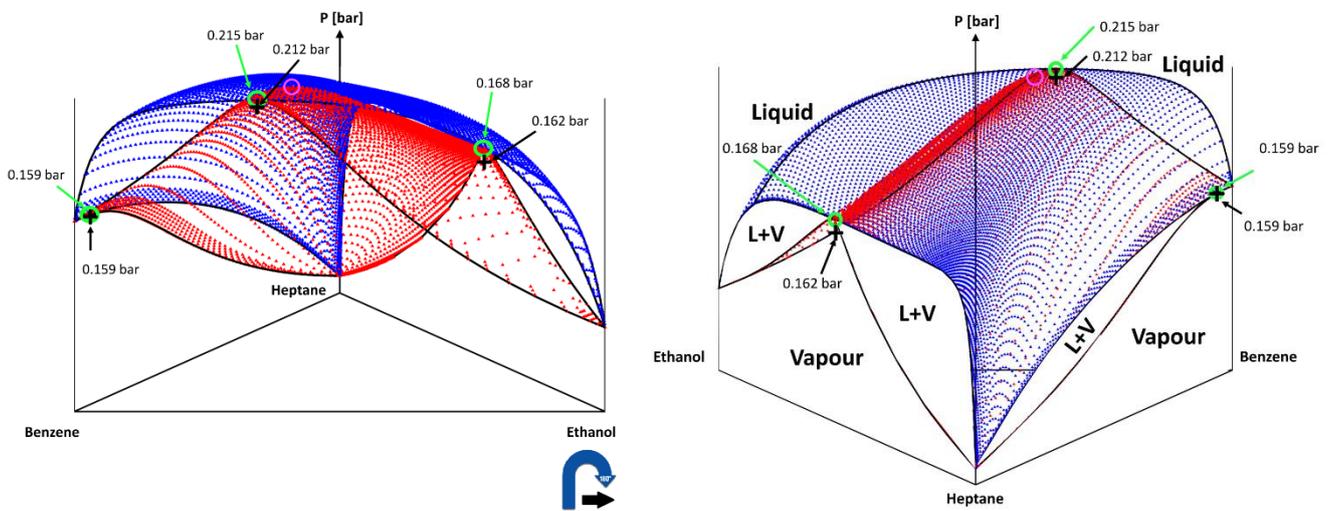


**Figure 17: Isothermal VLE of the system Benzene-Ethanol-Heptane predicted Δ dew points and Δ bubble points for 303.15 K calculated with UGC VTPR Twu EoS (a 0° and a 180° turned view). O = predicted binary azeotrope, + = calculated binary azeotrope data by Schmid** [49]**.**

A 3D isothermal VLE ternary diagram of the system Benzene-Ethanol-Heptane is shown in Figure 17. Two perspectives of the same system are used to better visualize the dew and bubble point progression with changing pressure of the ternary diagram. There are vapour-, liquid-, vapour-liquid regions similar to a binary mixture as seen in the depicted areas on the right hand side of Figure 17.

As no ternary experimental data, for the system decane (D)- hexadecane (HD)- nitrogen (N), could be found the binary experimental VLE data of only the systems decane-nitrogen and hexadecane-nitrogen are seen in Figure 18.
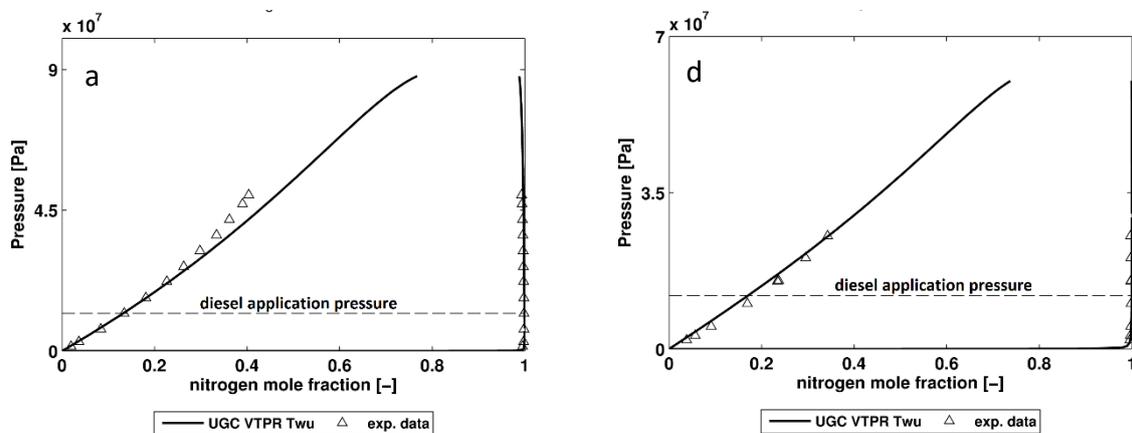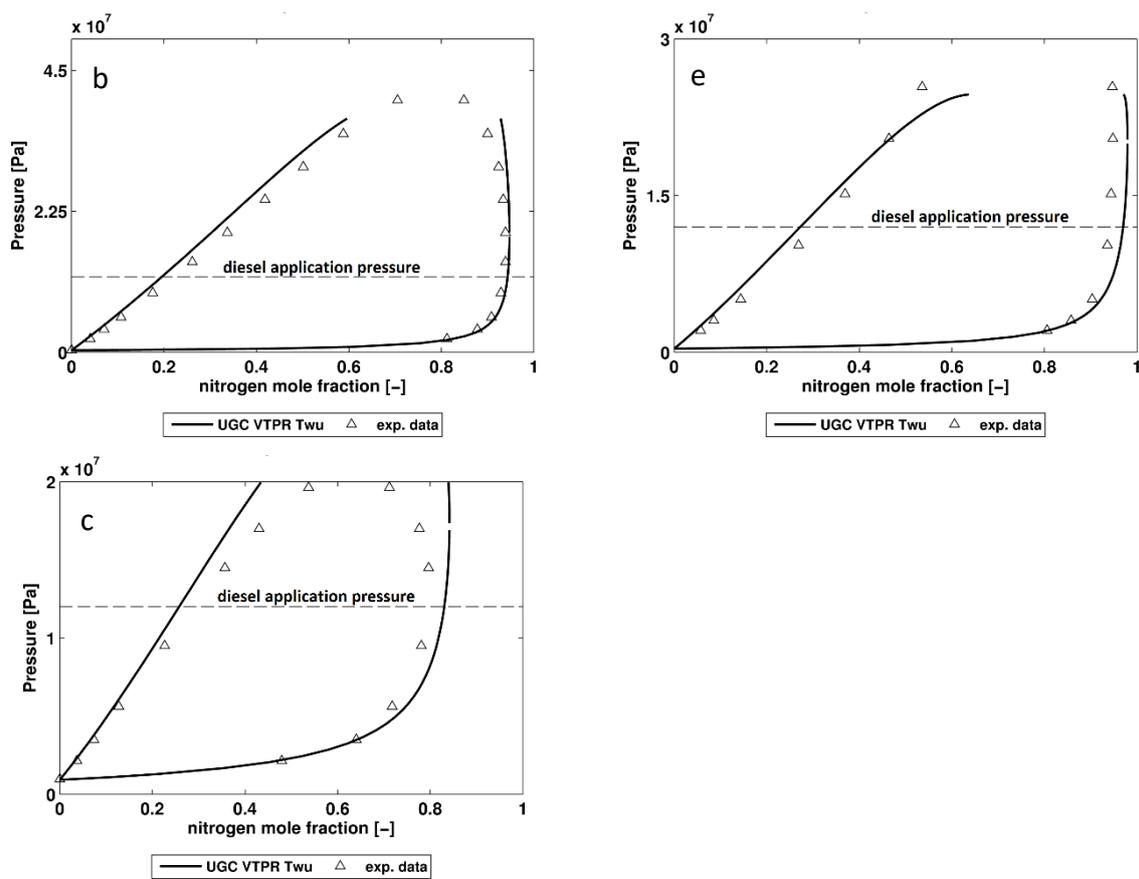
**Figure 18: Binary isothermal Pxy diagram for the system: decane-nitrogen:(a,b,c) T= 344.3 / 503 / 563.1 K**[50]**; hexadecane-nitrogen: (d,e) T= 462.7 / 623.7 K**[51]**.**

The UGC VTPR Twu EoS approach gives a good representation of the experimental data but the accuracy decreases with rising pressure. Figure 18 c/e shows the bubble and dew line increasingly deviating from the experimental data. However, as the maximum pressure in the IC diesel application is below 150 bar, it can be concluded that the UGC VTPR Twu model describes the solubility behavior of nitrogen in the fuel in the relevant pressure range with sufficient accuracy.

For Figure 18 a-e it was not possible to calculate the bubble and dew line for the UNIFAC approach used in the original multicomponent evaporation model as there is no $N_2$-group available in the original UNIFAC model.

Next the system decane – hexadecane – nitrogen, that will be used in the single droplet, spray box and engine sector simulations, is depicted in a 3D ternary isothermal VLE diagram for the

temperature of 600 K in Figure 19. It is seen that decane and nitrogen already reached their critical temperatures with only hexadecane in a subcritical state. As already seen in the chapter Binary Mixtures the bubble and dew line do not reach each other in the critical point of the mixture. This is believed to be the result of the used VLE algorithm and should be further investigated.
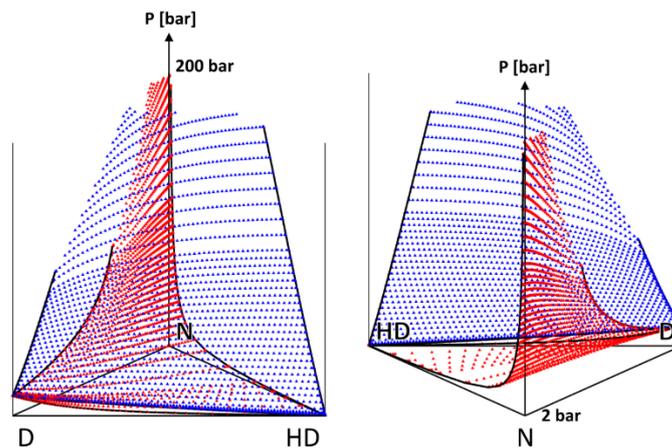


**Figure 19: 3D isothermal ternary VLE diagram for the system decane (D)-hexadecane (HD)-nitrogen (N) at 600 K predicted with the UGC VTPR Twu EoS.**

The determination of the unique vapour composition as the result of an unique liquid composition at the specified temperature is similar to binary mixtures. This time the individual fractions are evaluated by using the marked mixture composition of the liquid and vapour phase in the ternary diagram respectively as seen in Figure 20.
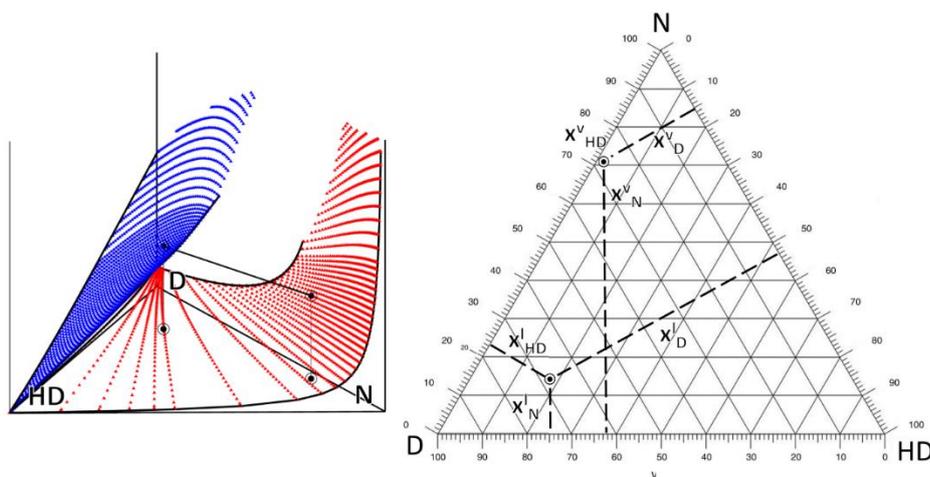


**Figure 20: Vapour-liquid equilibrium between a specific liquid composition $x^l$ and its vapour composition $x^v$.**

# 7.  Extension of the Multi- Component Droplet Evaporation Model

The EoS based VLE calculation method developed in this thesis was implemented into the AVL FIRE™ CFD Code extending an already available evaporation model based on Abramzon and Sirignano [4], which includes the multicomponent evaporation model by Brenn et al. [5] and the non-uniform heating model by Frolov [6].

Next these models will be briefly described and additionally the implementation and the basic modifications due to this thesis are presented.

From here on mass fractions will be denoted with $y^{v,l}$ and mole fractions with $x^{v,l}$ for mass/mole fractions in vapour and liquid respectively.

## 7.1.  Single Component Abramzon & Sirignano Evaporation Model

The model of Abramzon and Sirignano calculates the evaporation mass transfer rate from mass and heat balances integrated over the concentration and thermal boundary layers.

The model is characterized by the following features and assumptions:

- the condensation and evaporation takes place on a spherical droplet
- the droplet surface is uniform in temperature and vapour mass fractions
- the ambient gas does not dissolve in the droplet
- the heat and mass transfer are considered as quasi-steady, the pressure drop is negligible and the temperature dependent thermo-physical properties are calculated at some reference state inside the boundary layer surrounding the droplet

The model uses the 'film-theory' which introduces gas films of constant thicknesses surrounding the droplet. The heat and mass transport is not only affected by the diffusive transport process but also by the convective conditions in the proximity of the droplet surface. Convection enhances the transport, resulting in thicker films. The convective flow reduces the vapour concentration near the droplet surface resulting in a low vapour concentration. Thus, a flow away from the droplet is induced. This flow is called Stefan flow and is responsible for the increase of the film thickness

The vaporization rate utilizing the Nusselt and Sherwood number reads

$$\dot{m} = 2r_s \pi \bar{\rho}_f \bar{D}_{v,a} Sh^* \ln(1 + B_M) \tag{7.1}$$

$$\dot{m} = 2r_s \pi \frac{\bar{\lambda}_f}{\bar{c}_{p,v}} Nu^* \ln(1 + B_H) \tag{7.2}$$

where $r_s$ is the droplet radius, $\bar{\rho}_f, \bar{D}_{va}, \bar{\lambda}_f, \bar{c}_{p,v}$ the film density, the diffusion coefficient between vapour and ambient gas, the heat conductivity of the film and the isobaric heat capacity of vapour at a reference temperature/fuel concentration respectively.

The reference temperature/fuel concentration are defined by equally weighting the droplet surface and the ambient gas (½ - rule )[1]

$$\bar{T} = T_s + \frac{1}{2}(T_\infty - T_s) \quad \text{and} \quad \bar{Y} = Y_s + \frac{1}{2}(Y_\infty - Y_s) . \tag{7.3}$$

$Sh^*, Nu^*$ are modified Sherwood and Nusselt numbers through correction factors considering the deviating gas film thicknesses for spherical films

$$Nu^* = 2 + \frac{(Nu_0 - 2)}{F_H} \quad \text{with} \quad Nu_0 = 2 + 0.552\,Re^{1/2}\,Pr^{1/3} \tag{7.4}$$

$$Sh^* = 2 + \frac{(Sh_0 - 2)}{F_M} \quad \text{with} \quad Sh_0 = 2 + 0.552\,Re^{1/2}\,Sc^{1/3} \tag{7.5}$$

the correction factors $F_H, F_M$ are calculated through the same function

$$F(B) = (1 + B)^{0.7} \frac{\ln(1 + B)}{B} \tag{7.6}$$

using $B_H$ the Spalding heat transfer coefficient

$$B_H = \frac{\bar{c}_{p,v}(T_\infty - T_s)}{\dot{Q}_{l,d}/\dot{m} - \Delta h_v(T_s)} \tag{7.7}$$

[1]optionally the 1/3- rule can be used

and $B_M$ the Spalding mass transfer number

$$B_M = \frac{y_{v,s} - y_{v,\infty}}{1 - y_{v,s}} \quad .$$ (7.8)

This leads to a non-linear system of 3 equations (7.1), (7.2) and (7.7) for 3 unknowns $\dot{m}, B_H, \dot{Q}_{l,d}$ which is solved iteratively to finally calculate the diameter and the temperature change of the droplet from overall heat and mass balances for the droplet.

### 7.1.1. Multicomponent Modification of the Abramzon & Sirignano Evaporation Model

The multicomponent evaporation model applied in the AVL FIRE™ CFD code was developed by Brenn et al.[5] and is based on the Abramzon and Sirignano model described in previous chapter. The mass transfer is represented by the single component mass transfer rates $\dot{m}_i \, (i = 1,..,N)$, which add up to the total mass transfer rate

$$\dot{m} = \sum_i \dot{m}_i \quad ,$$ (7.9)

whereas the heat transfer remains global (see Figure 21).
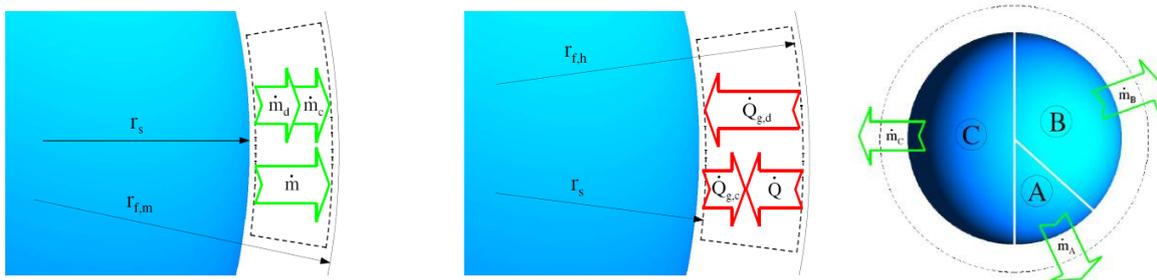


**Figure 21: Mass and heat fluxes for the multi-component droplet evaporation** [52]

For the multi-component mixture it is assumed for simplification that the components are homogeneously distributed inside the droplet.

[1]optionally the 1/3- rule can be used

The proposed individual mass transfer rates $\dot{m}_i$ result in individual gas film thicknesses for each species.

Similar to Eq.(7.1) the evaporation rate of the individual species reads

$$\dot{m}_i = 2r_s \pi \overline{\rho}_f \overline{\overline{D}}_{i,a} Sh_i^* \ln(1 + B_{M,i})$$ (7.10)

with the Spalding mass transfer number for each component

$$B_{M,i} = \frac{y_{i,s} - y_{i,\infty}}{1 - y_{i,s}} \; .$$ (7.11)

Variables $y_{i,s}, y_{i,\infty}$ denote the mass fractions of the species i at the droplet surface and in the ambient gas, respectively. $y_{i,s}$ is calculated through the vapour-liquid equilibrium at the interface of the evaporating droplet.

With the original model of Abramzon and Sirignano Raoult's law and Dalton's law are used to describe the vapour-liquid equilibrium yielding for the vapour mole fraction of component i at the droplet surface

$$x_{i,s} = x_{i,l} \frac{P_i^s}{P}$$ (7.12)

Brenn et al. [5] integrated the UNIFAC method to describe the state of equilibrium taking into account the activity coefficients $\gamma_i$

$$x_{i,s} = x_{i,l} \gamma_i \frac{P_i^s}{P}$$ (7.13)

This approach reproduces the vapour-liquid equilibria for an arbitrary number of non-ideal liquid mixtures reasonably well for pressures below 5-10 bar as already mentioned in 6.2 Binary Mixtures.

The general iteration algorithm for solving the heat/mass transfer of the presented model is depicted in Figure 22.

1. Evaluate $y_i$ at the droplet surface

2. Get the average physical properties $\bar{\rho}, \bar{c}_{p,l}, \bar{c}_{p,v}, \bar{k}_f, \bar{\mu}_f, \bar{\beta}_f$

3. Calculate $Nu_0$, $Sh_0$

4. Get $B_M, F_M, Sh^*, \dot{m}$

5. Guess the value of $B_H$ by using the value from the previous iteration or time step

6. Calculate the modified Nusselt number $Nu^*$

7. Calculate $B_H^+$ by

$$B_H^+ = \prod_i \left(1 + B_{M,i}\right)^{\psi_i} - 1 \qquad \text{with} \qquad \psi_i = \frac{c_{p,v} \rho_f \bar{D}_{i,a} Sh_i^*}{\bar{\lambda}_f Nu^*}$$

8. if $|B_H - B_H^+| < \varepsilon$ continue with step 9, else continue wit step 5

9. Calculate the heat transfer by

$$\dot{Q}_{l,d} = \dot{m}\left(\frac{\bar{c}_{p,v}\left(T_\infty - T_S\right)}{B_H} - \Delta h_v\left(T_S\right)\right)$$

**Figure 22: The final algorithm to calculate the heat and mass transfer** [53]

## 7.1.2. Non-uniform Heating of the Droplet Interior

As an alternative to the rapid mixing assumption causing homogeneous temperature and composition inside the droplet a simple approach to take into account a radial temperature profile is available in FIRE™ (see Frolov [6]). This approach calculates the droplet center temperature from a series evaluation and provides an estimate for the droplet surface temperature (see sketched profiles 1 to 5 in Figure 23).

This is especially important for cases where rapid mixing does not take place and a surface temperature higher than inside the droplet is established, which will affect the VLE calculations.
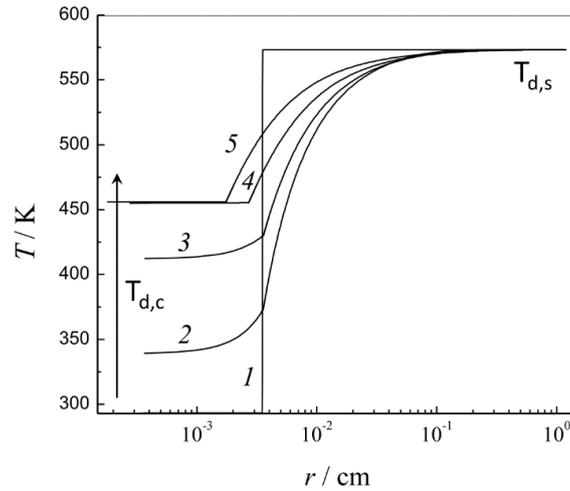
**Figure 23:** *Evaporation Dynamics of n-tetradecane (C14H30) droplet of initial diameter 70 µm in air at normal pressure and temperature of 573.15 K; Predicted temperature distributions: curve 1: t = 0 ms; curve 2: t= 5 ms; curve 3: t= 14 ms, curve 4: t= 39.2 ms and curve 5: t = 54 ms.*[53]

From the analytical solution for the temperature distribution inside the droplet one can describe the temperature evolution of the droplet center in time as

$$T_{d,c} = T_{d,s} + 2\left(T_{d,s} - T_{d,0}\right) \sum_{m=1}^{\infty} (-1)^m \exp\left(-m^2 \pi^2 \frac{a\,t}{r_d^2}\right) , \qquad (7.14)$$

with the thermal diffusity a and m the integer series variable.

Frolov further found a relation between the center, surface and average droplet temperature that reads

$$T_d \approx T_{d,c} + \frac{3}{4}\left(T_{d,s} - T_{d,c}\right) . \qquad (7.15)$$

With Eq. (7.14) and (7.15) the surface temperature can be calculated by

$$T_{d,s} \approx \frac{4}{3} T_d - \frac{1}{3} T_{d,c} . \qquad (7.16)$$

### 7.1.3. Real Gas Modifications in the VLE Calculation at the Droplet Surface

Using the UNIFAC-ideal gas method to calculate the liquid-vapour equilibrium during a compression cycle inside a combustion engine with gas pressures up to 120 bar may not be accurate enough, as has been shown in comparison of VLE calculations with experimental data in chapter 6.2 Binary Mixtures. Taking into account interactions between the fuel and ambient

gas molecules near the droplet surface, as well as the solubility of ambient gas inside the droplet can be expected to improve the evaporation model. The solubility of the ambient gas is most important to the outermost layer of the droplet, as the gas diffusing towards the droplet center does not affect the evaporation of the droplet [2].

As a simplification it is assumed that the ambient gas only consists of nitrogen, to determine the vapour-liquid equilibrium at the droplet interface (i.e. one droplet with a specific fuel composition, temperature and pressure is surrounded by its vapour components and nitrogen as representative for the inert gas contents).

To achieve the vapour-liquid equilibrium we already know that the conditions of Eq. (2.10) must be satisfied. These are

$$x_i^l \varphi_i^l \left( P, T, x_i^l, ..., x_{N+1}^l \right) = x_i^v \varphi_i^v \left( P, T, x_i^v, ..., x_{N+1}^v \right)$$

(7.17)

for N fuel components and component N+1 for nitrogen.

Overall Eq.(7.17) can be solved with the bubble point successive substitution VLE algorithm as sketched in Figure 9. As an additional condition now the dissolved mole fractions of ambient gas in the droplet surface layer are calculated from the VLE condition for i=N+1, in such a way that the given system pressure is reached.

The algorithm consists, at the time of this thesis, of following steps:

1. Read the ambient gas pressure $P$, the droplet/surface temperature $T$ and the liquid composition of the fuel $x_i^l$

2. Estimate the vapour mole fraction $x_i^v$

3. Check the droplet temperature and if available the difference between the old temperature and the current droplet temperature

    a. if the temperature or the temperature difference exceed a limit, no VLE is calculated, a flag is set and the last $x_i^v$ is reused

    b. otherwise move to step 4

4. Calculate $P_l$ utilizing only the fuel fractions without the ambient gas with the Antoine Equation

5. Check if there is a last calculation step available

    a. If not available: use an initial ambient gas mole fraction and the pressure of $P_1$ for the bubble point $P_2$ calculation estimate

    b. If available: use the pressure and the vapour fraction of the last calculation step for the bubble point $P_2$ calculation estimate

6. Calculate $P_2$

    a. If successful go to step 7

    b. If not successful use a different $x_i^v$ condition one time and go to step 6

    c. If not successful and a different $x_i^v$ condition was already used, no VLE is calculated, a flag is set and the last $x_i^v$ is reused

7. Calculate with $P$, $P_1, P_2, x_{1,N_2}^l, x_{2,N_2}^l$ through the secant method $x_{3,N_2}^l$, the nitrogen fraction solved inside the liquid droplet

8. The new mole fraction $x_{3,N_2}^l$ is considered which changes the fuel component fractions accordingly

9. Calculate $P_3$

    a. If successful go to step 10

    b. If not successful use a different $x_i^v$ condition one time and go to step 9

    c. If not successful and a different $x_i^v$ condition was already used, no VLE is calculated, a flag is set and the last $x_i^v$ is reused

10. Either $P_1$ or $P_2$ is exchanged with $P_3$ and $x_{1,N_2}^l$ or $x_{2,N_2}^l$ with $x_{3,N_2}^l$ respectively

11. While $|P_3 - P| \triangleright \varepsilon$ go to step 7

12. Save the droplet/surface temperature and the vapour mole fraction

13. Output $x_i^v$

The simplified algorithm is seen in Figure 24 a) which represents the calculation of the vapour-liquid equilibrium for the system decane (D)-hexadecane (HD)-nitrogen (N) with a given droplet temperature, pressure and composition. Figure 24 b) c) represent the steps 1 - 11 and Figure 24 d) represents the step 13 of the algorithm.
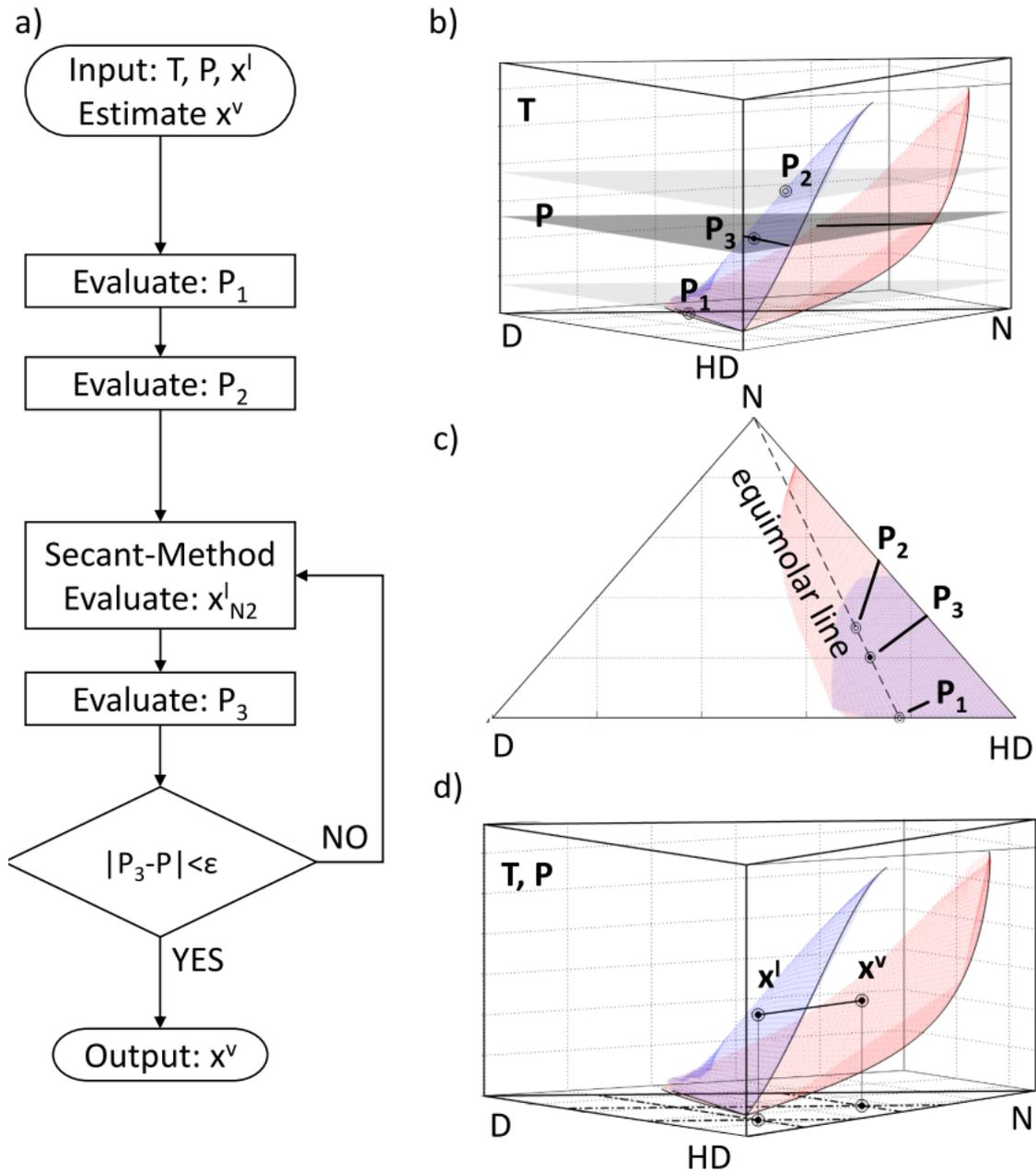
**Figure 24: Ternary mixture VLE algorithm with a secant method to determine the mole fraction of dissolved gas at the surface of the liquid mixture.**

# 8.   Application Studies

This chapter is focused on presenting the differences in prediction between the original multi-component (oMC) and the modified multi-component (mMC) evaporation model. The first section shows oMC and mMC single droplet evaporation differences using a variation of physical parameters. In the second section the behavior of the oMC and mMC model is tested in spray simulations. The simulations are compared to experimental data if available. In the third section a diesel engine sector geometry with a moving piston was considered and again compared to experimental data if available.

## 8.1.   Single Droplet

The mixtures studied are the octane-eicosane and decane-hexadecane systems with initial parameters used for the simulation listed in Table 7. The system octane-eicosane has been used to provide a system with very different volatilities of the components, while decane-hexadecane has been chosen since for this fuel blend experimental data from spray box cases are available. This allows direct comparability for single droplet on spray effects using the same fuel blend.

**Table 7: Initial simulation input parameters (single droplet)**

| Case | Liquid | Mass Fraction [%] | init. Droplet Diameter [μm] | Droplet Temperature [K] | Velocity [m/s] | Ambient Temperature [K] | Ambient Pressure [bar] | Non-uniform heating |
|------|--------|-------------------|-----------------------------|--------------------------|----------------|--------------------------|------------------------|---------------------|
| 1 a  | Octane | 50 | 80 | 353.3 | 0 | 600 | 50 | - |
| b    | Eicosane | 50 | 80 | 353.3 | 0 | 600 | 150 | - |
| c    |        |    | 80 | 353.3 | 0 | 900 | 50 | - |
| d    |        |    | 80 | 353.3 | 0 | 900 | 150 | - |
| 2 a  | Decane | 50 | 80 | 353.3 | 0 | 760 | 73 | - |
| b    | Hexadecane | 50 | 80 | 353.3 | 0 | 900 | 73 | - |
| c    |        |    | 80 | 353.3 | 100 | 760 | 73 | x |
| d    |        |    | 80 | 353.3 | 100 | 900 | 73 | x |

Figure 25 to Figure 32 and Figure 34 a) show the surface decay of a droplet as a function of time, in b) evaporation rates of the individual species are shown and c) the droplet temperature as a function of time. The solid lines represent the evaporation model with the original vapour-liquid equilibrium and the dashed lines represent the evaporation model with

the modified real gas based vapour-liquid equilibrium. These models will be called oMC model and mMC model in the remainder of this work.

Figure 25 shows the system octane-eicosane with a mass fraction of 50% each with an ambient temperature of 600 K and gas pressure of 50 bar. a) a split up of the d² progression can be observed as the volatilities differ strongly between the components. The first slope which is steeper represents the more volatile component that evaporates first. The second slope, which is more flat, is defined by the less volatile component and is in the end determining the droplet lifetime. b) the evaporation rates of the two components are compared. With the more volatile component reaching a maximum value sooner, whereas the evaporation rate of the less volatile component reaches its maximum later. The differences in evaporation rate between the multi-component evaporation model with the original VLE (oMC) and the multi-component evaporation model with the modified VLE (mMC) of the more volatile component are, at the case specific conditions, minimal. While for the less volatile component the mMC model reaches a higher evaporation rate. The increase in diameter at the first few time-steps can either be explained through condensation or thermal expansion due to heat transfer into the droplet and the rise of its temperature resulting in a change of the droplet density. Condensation would result in a negative mass flow rate, which does not occur. c) shows that the droplet temperatures are limited through the ambient temperature. Both models reach a similar droplet temperature.
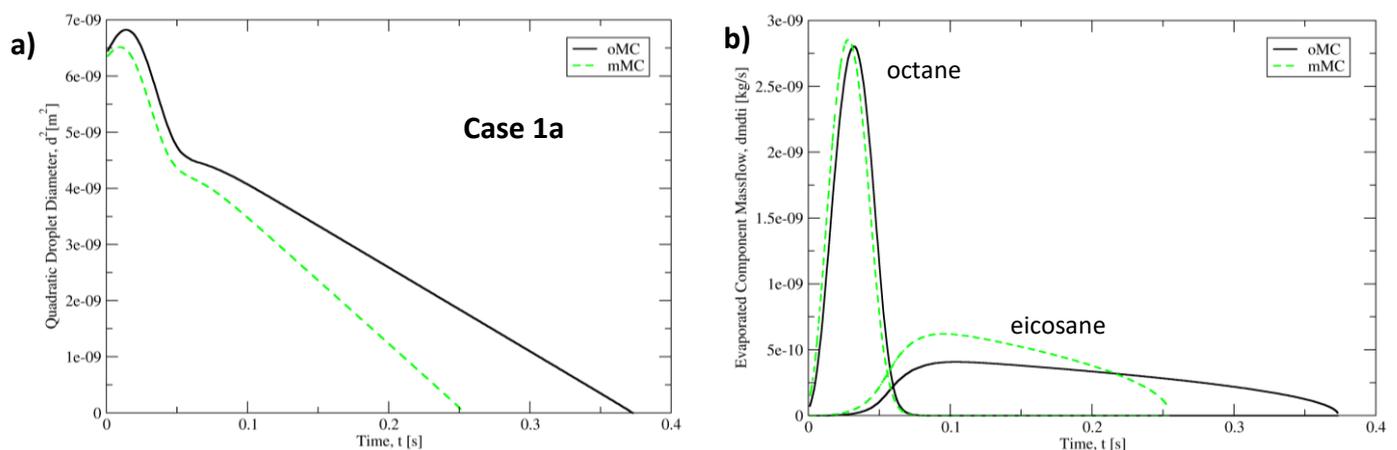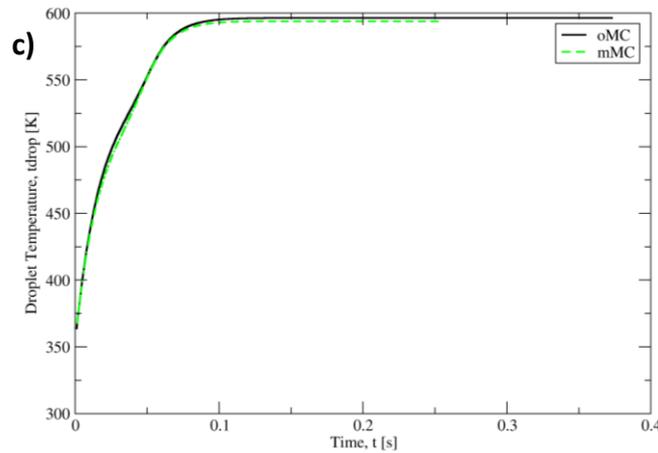
**Figure 25: a) Surface decay and b) evaporation rates c) droplet temperatures for Case 1a (50 bar / 760 K)**

Figure 26 shows the same system with the gas pressure increased to 150 bar. In this case the differences in the decrease of the droplet surface area between the oMC and mMC are severe. Again two separate slopes can be seen separating the component that is more volatile, octane, and the component that is less volatile, eicosane. Comparing the evaporation rates in Figure 26 b) the enhanced evaporation rates due to the modified evaporation model can clearly be seen as octane and eicosane reach a higher evaporation rate. It is interesting to note that comparing the evaporation rates at 50/150 bar especially for eicosane we see that they are strongly reduced using the oMC model, whereas the evaporation rate changes to a much smaller extend by using the mMC model. The reason is the use of the low pressure UNIFAC model VLE formula $x_i^v = x_i^l \dfrac{P_i^s(T)}{P} \gamma_i(T,x)$ . As can be seen for the same temperature the values $\gamma_i$ and $P_i^s$ are the same as they are non-depended on pressure. With triple ambient gas pressure
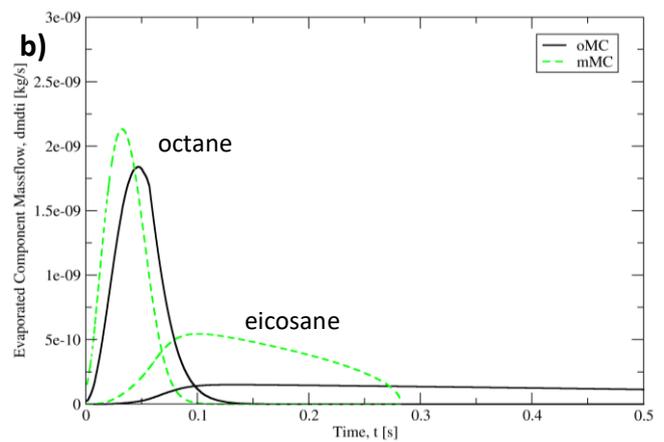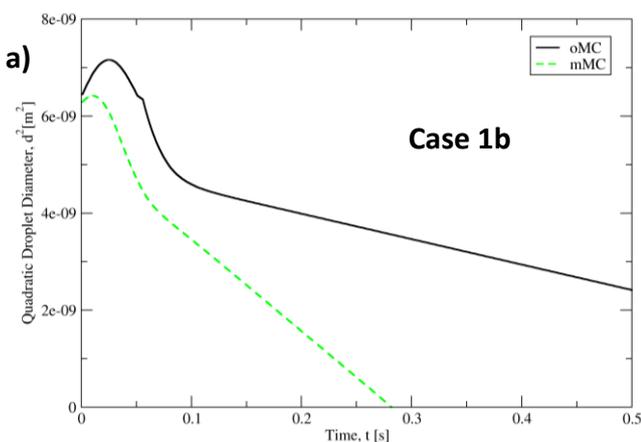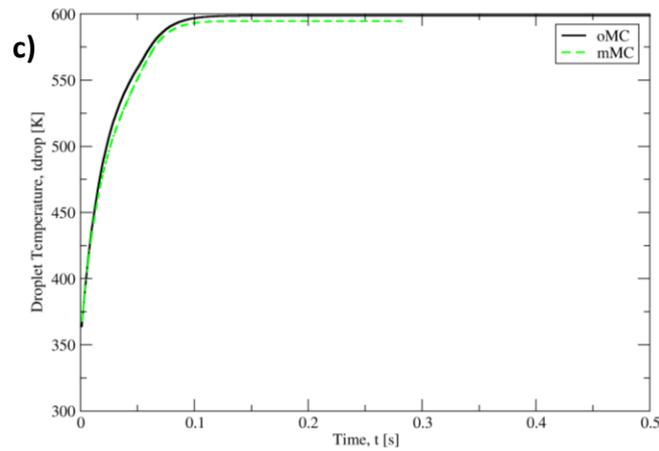
**Figure 26: a) Surface decay and b) evaporation rates c) droplet temperatures for Case 1b (150 bar / 760 K)**

and the droplet temperature limited by the ambient temperature the $x_i^v$ values can be reduced up to 1/3 of the value at 50 bar ambient gas pressure as the pressure influence on the VLE is neglected on both the liquid and vapour phase using the original multicomponent evaporation model.



**Figure 27: a) Surface decay and b) evaporation rates c) droplet temperatures for Case 1c (50 bar / 900 K)**

**Figure 28: a) Surface decay and b) evaporation rates c) droplet temperatures for Case 1d ( 150 bar / 900 K )**

Figure 27 and Figure 28 again show the system octane-eicosane but with an increased ambient temperature of 900 K and gas pressures 50 and 150 bar respectively. The increased temperature reduces the droplet evaporation time with increased and more similar evaporation rates of both components such that different d² slopes can hardly be seen. In Figure 27 a) the sudden droplet in surface decay at approximately 30 ms for the oMC model is encountered due to reaching the critical temperature of the mixture and the conversion of the remaining droplet into vapour. This is not the case for the mMC model for which the critical temperature of the mixture is not reached. The evaporation rate for Figure 27 and Figure 28 b) is again, at the lower pressure, similar for the component octane and higher for the component eicosane. Octane with the oMC model reaches a higher maximum evaporation rate due to a higher droplet temperature seen in Figure 27 and Figure 28 c). The kinks visible in the diameter evolutions and mass transfer rates using the oMC approach are due to the mixing rules for the thermophysical properties applied at temperatures where one of the components is already in supercritical state. In this case the property values at critical state

are used anyway. This causes kinks (e.g., in the density calculation of the liquid phase). The new mMC avoids this disadvantage by using UGC VTPR Twu EoS results for the liquid density.

In Figure 28 for the elevated gas pressure of 150 bar we experience the same sudden drop in surface decay as the droplet temperature reaches the linear mixture of the critical component temperatures at approximately 17 ms as the evaporation rate is reduced in consequence of the higher gas pressure and therefore the droplet heat up is increased.

Again for the evaporation rate b) the enhancement due to the mMC model can clearly be seen. The oMC model reaches the critical droplet temperature sooner and thus the droplet evaporates faster.

Next for the cases 2a and 2b the single droplet system decane-hexadecane is simulated with the same binary mixture of 50% mass-fraction decane and hexadecane as used in the spray box cases discussed below. Figure 29 and Figure 30 depict the surface decay a) and the evaporation rate b) using ambient temperatures of 760 and 900 K at a gas pressure of 73 bar. No separation of slopes but a parabolic surface decay can be seen. The mMC leads to a faster evaporation of the droplet liquid and again to similar evaporation rates for the more volatile component, decane and slightly enhanced evaporation rates for the less volatile component, hexadecane. In the case of 900 K ambient temperature the oMC model reaches the critical temperature of the mixture before the mMC model resulting in a faster evaporation.
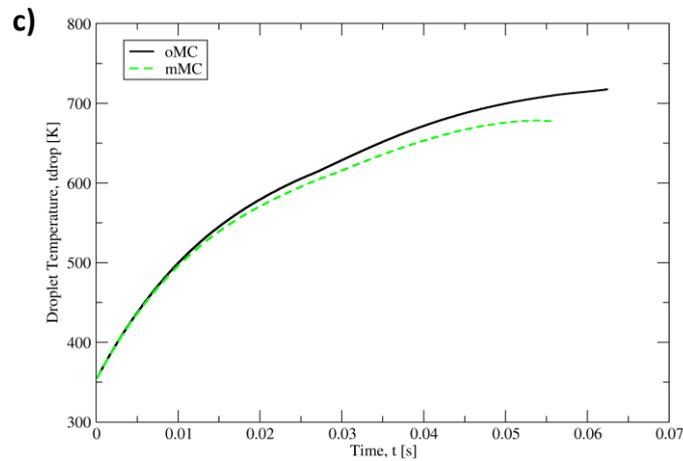
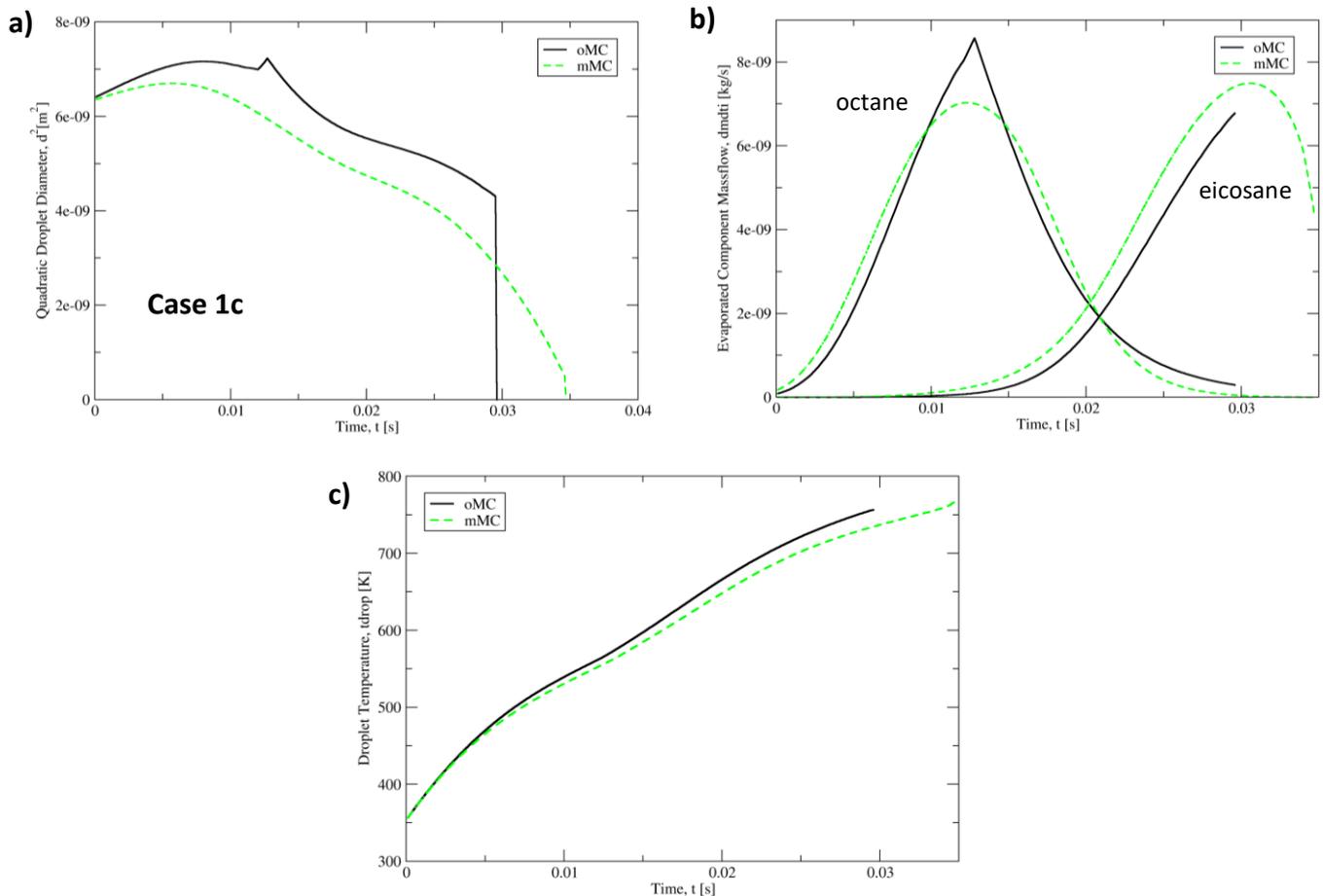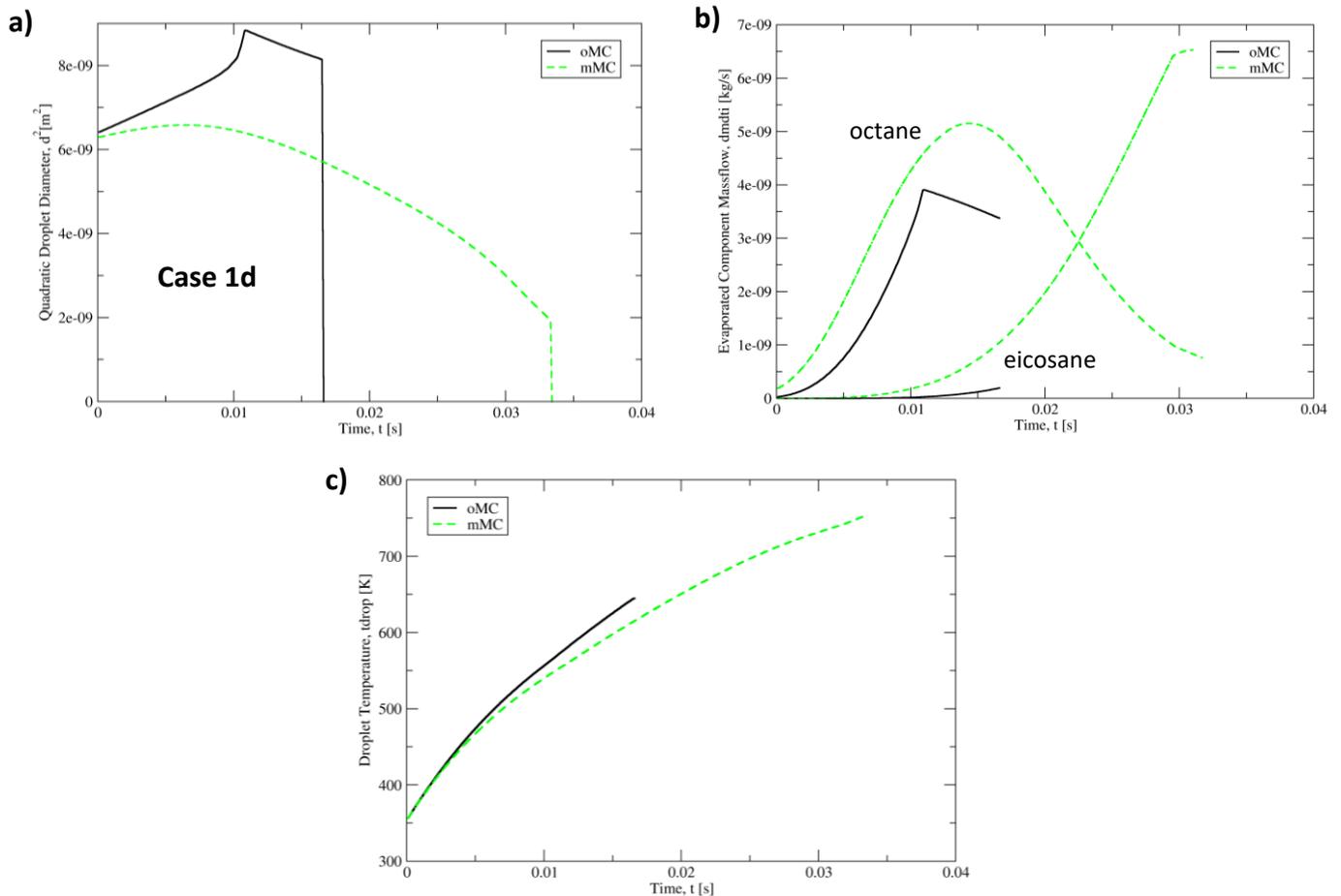**Figure 29: a) Surface decay and b) evaporation rates c) droplet temperatures for Case 2a (73 bar / 760 K)**



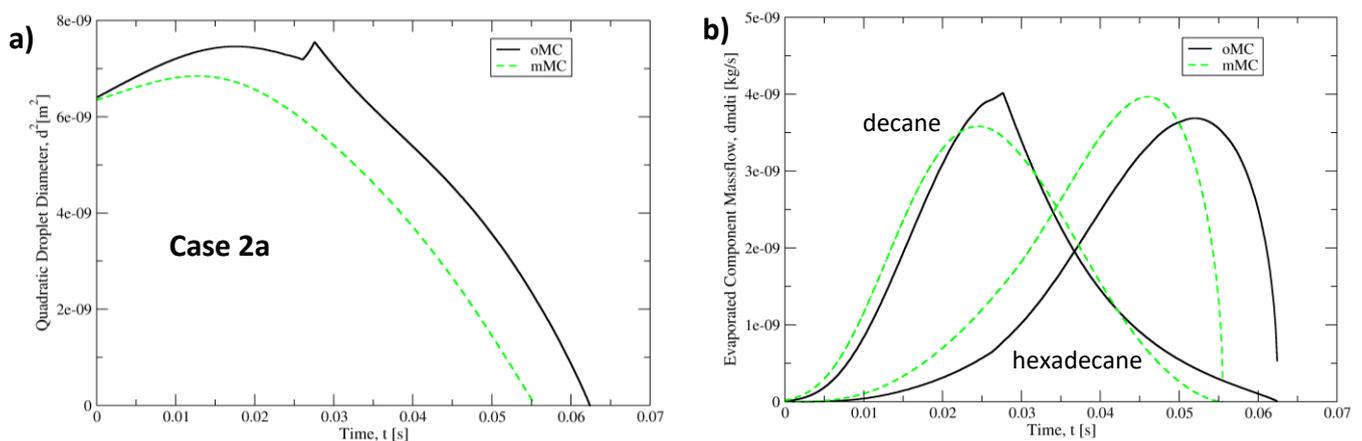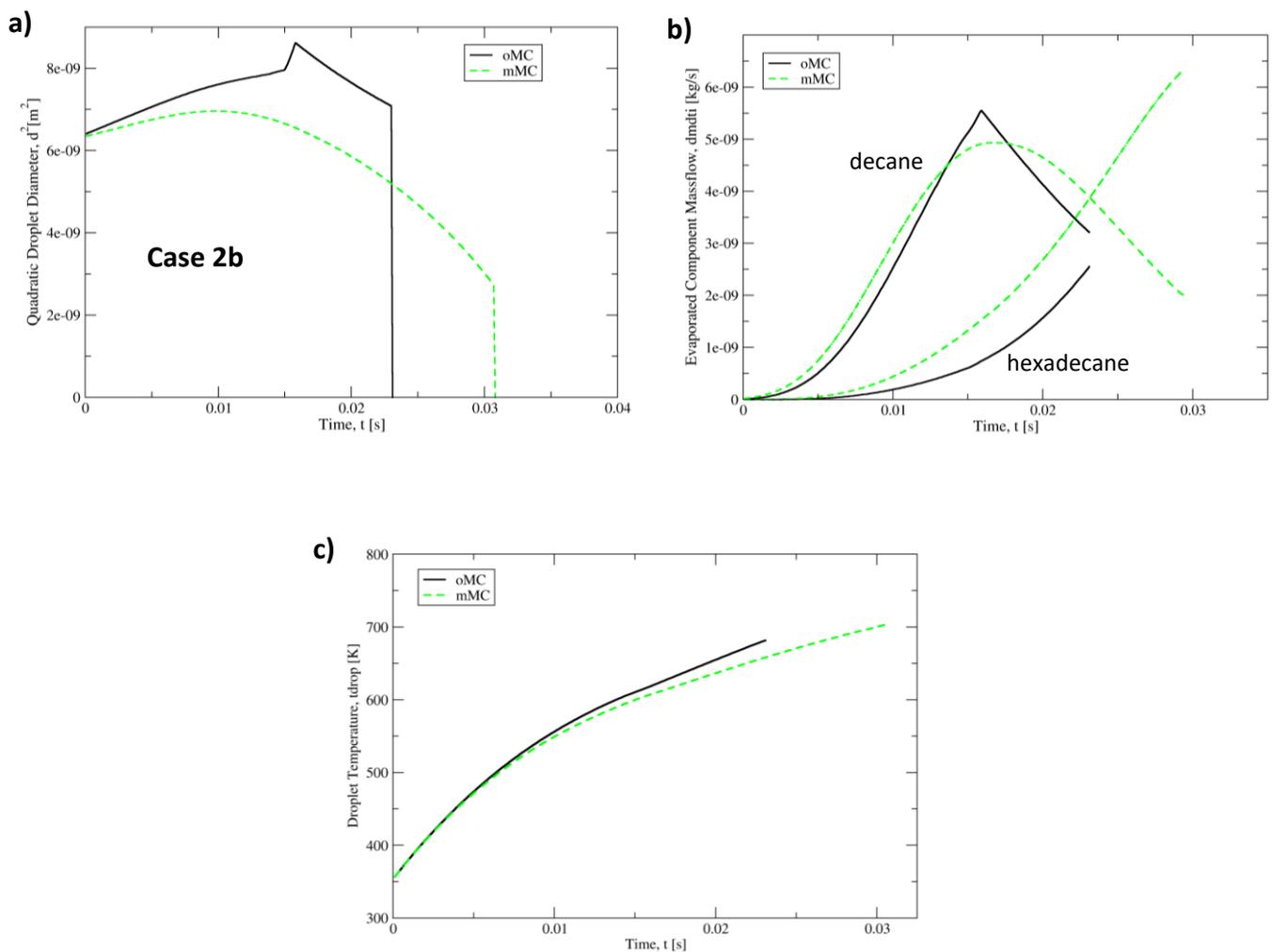**Figure 30: a) Surface decay and b) evaporation rates c) droplet temperatures for Case 2b (73 bar / 900 K)**

In addition Figure 31 and Figure 33 of system decane and hexadecane are shown with the non-uniform heating model and a normal velocity of 100 m/s.

The single droplet cases 2c and 2d got similar initial physical condition as the cases 2a and 2b respectively but the non-uniform heating model and a normal velocity of 100 m/s in cross-direction is additionally used. In the 760 K case (2c) the evaporation time is halved with a similar quantitative surface decay. However differences between the oMC and mMC approach can still be seen in Figure 31 a). As the surface temperature deviates from the mean droplet temperature up to 100 K (see Figure 32 ) the evaporation rates with the non- uniform heating model are enhanced for both the oMC and mMC approach. Again with higher evaporation rates the mMC model reaches lower surface temperatures.
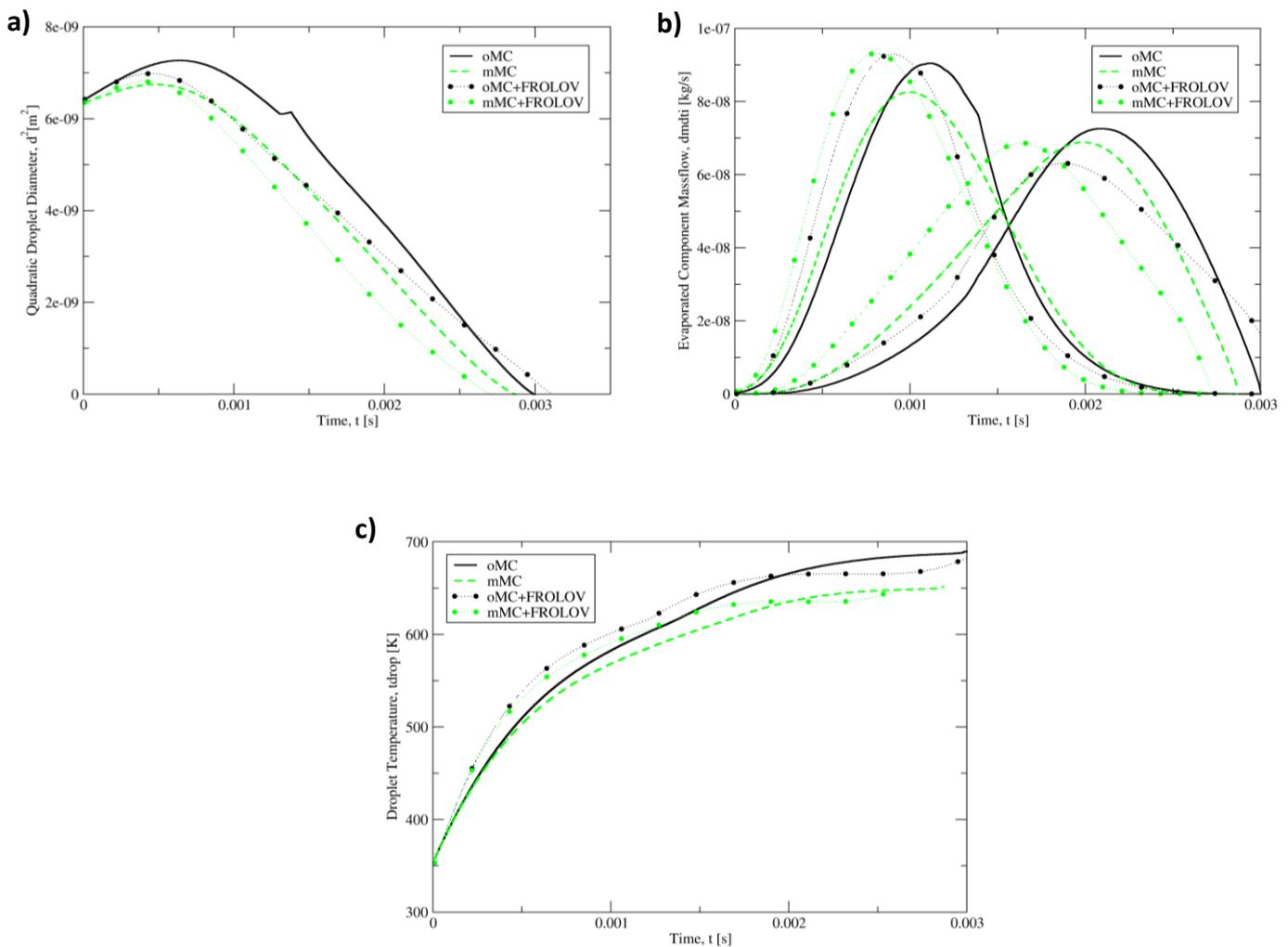


**Figure 31: a) Surface decay and b) evaporation rates c) droplet temperatures for Case 2c (73 bar / 760 K / 100 m/s).**
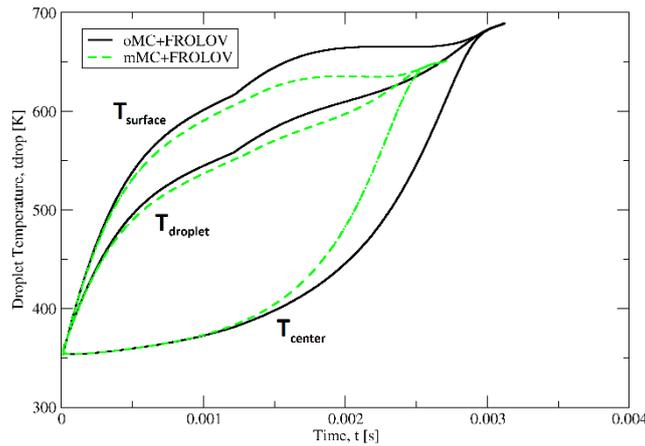
**Figure 32: Non- uniform heating model surface, droplet and center temperature for Case 2c (73 bar / 760 K / 100 m/s).**

Increasing the ambient temperature to 900 K (case 2d) only the oMC reaches the critical mixture temperature of the droplet. The reason is the overall reduced evaporation rate of decane and hexadecane (e.g. as was already seen in chapter 6.3 Ternary Mixture, decane reduces the critical mixture temperature).  As seen in Figure 33 b) the oMC reaches the highest evaporation rates for the component hexadecane. This is caused by the combination of two effects:

1.  a higher mass fraction decane inside the fuel droplet and
2.  a higher droplet temperature.
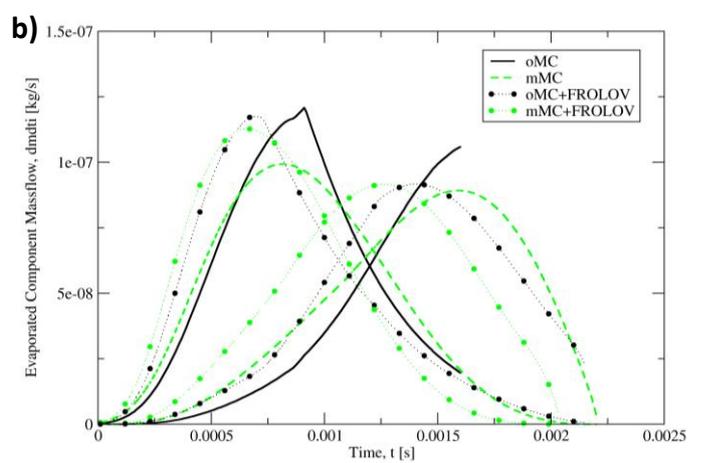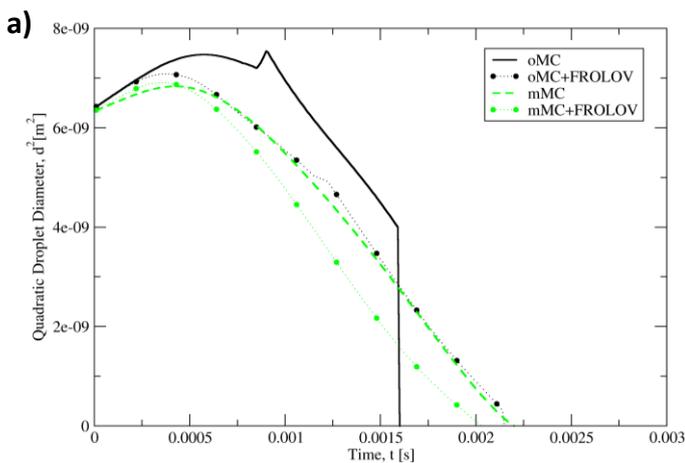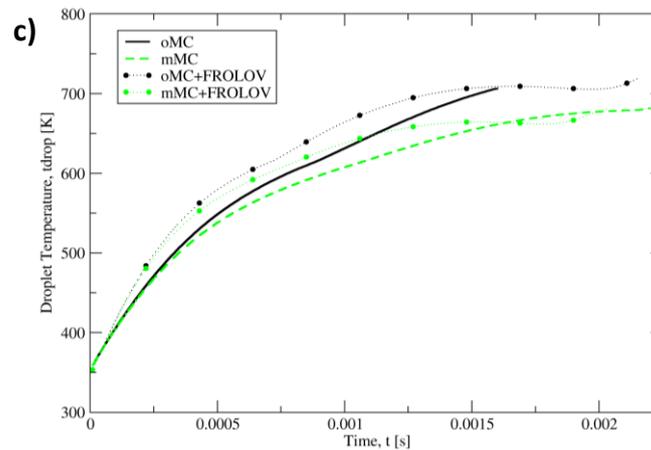
**Figure 33: a) Surface decay and b) evaporation rates c) droplet temperatures for Case 2d (73 bar / 900 K / 100 m/s)**
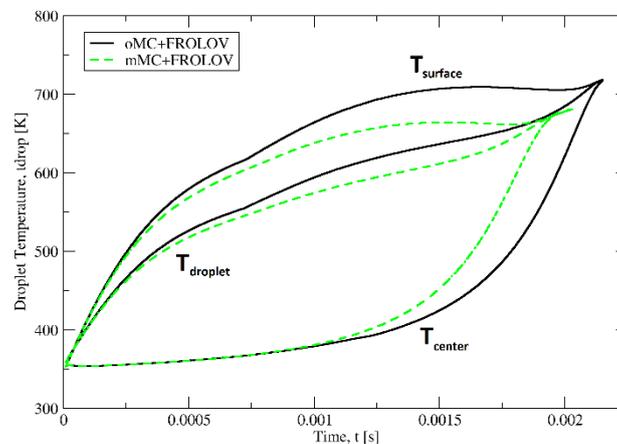


**Figure 34: Non- uniform heating model surface, droplet and center temperature for Case 2d (73 bar / 900 K / 100 m/s)**

### 8.1.1. Summary

For the octane-eicosane system a clear linear surface decay for the ambient temperature of 600 K with different slopes for the different components can be seen. The enhancement of the eicosane evaporation and the exaggerated reduction of the evaporation rate with the oMC model at high pressures has been detected. With rising temperature, the oMC model is not bounded by a low ambient temperature anymore and reaches higher temperatures at the droplet surface.

The non-uniform heating model describes the heating of the droplet more realistic. It provides three temperatures: surface (used for the VLE calculation), average droplet and center (see Figure 32 and Figure 34).  Which can be compared to the default rapid mixing model which uses the average droplet temperature for the VLE calculation.

In general it can be concluded that the mMC model by calculation of the VLE with the droplet surrounding nitrogen generally enhances the droplet evaporation especially of the less volatile component.

## 8.2. Spray Box

This section contains the description and discussion of the simulations of spray box cases under conditions typical for fuel injection in diesel engines. The simulation results are compared with experimental data gained from tests with a modified single cylinder engine at CMT Valencia [54]. The modified 2-stroke direct injection diesel engine (Jenbacher JW50) allows for studies under Diesel like thermodynamic conditions.

The research engine with its four orthogonal openings in the added combustion chamber with an example of a typical Schlieren image can be seen in Figure 35.
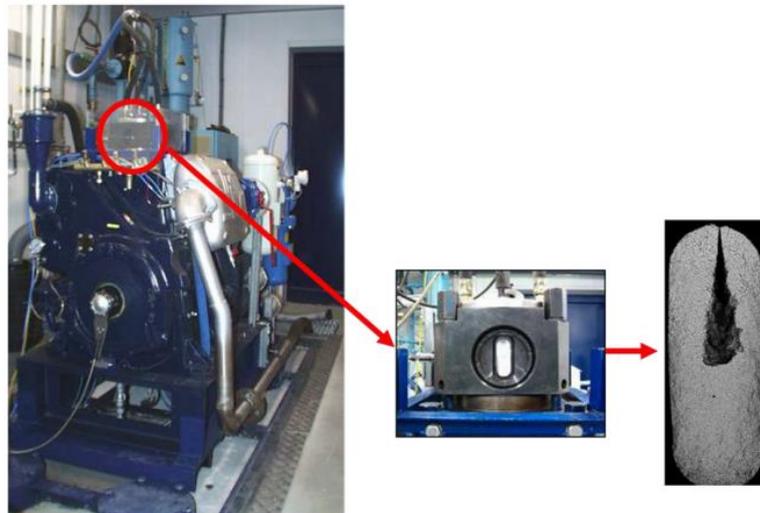


**Figure 35: Optical accessible research engine JW50 [54]**

The spray liquid length was measured by Mie scattering (i.e. light scattered by liquid droplets) that is imaged by a digital high speed camera [55]. For the vapour phase penetration length a transmission Schlieren setup is used [56]. The experimental arrangement is depicted in Figure 36.
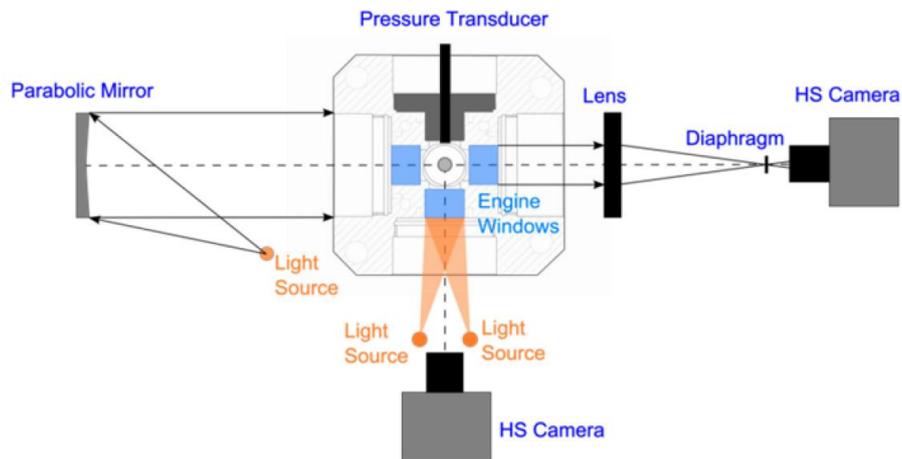
**Figure 36: Experimental setup spray penetration measurements [54]**

### 8.2.1. Input Parameters and Geometry

For the computational domain of the spray box geometry a cylindrical shape has been chosen. Due to the axial and radial symmetry of the spray finally a 90 degree cylinder sector has been used for the computational grid (see Figure 37). The cylinder dimensions are: h= 0.0858m, r= 0.023m, α= 90°. The number of cells is 576000. The grid is refined near the injection point.
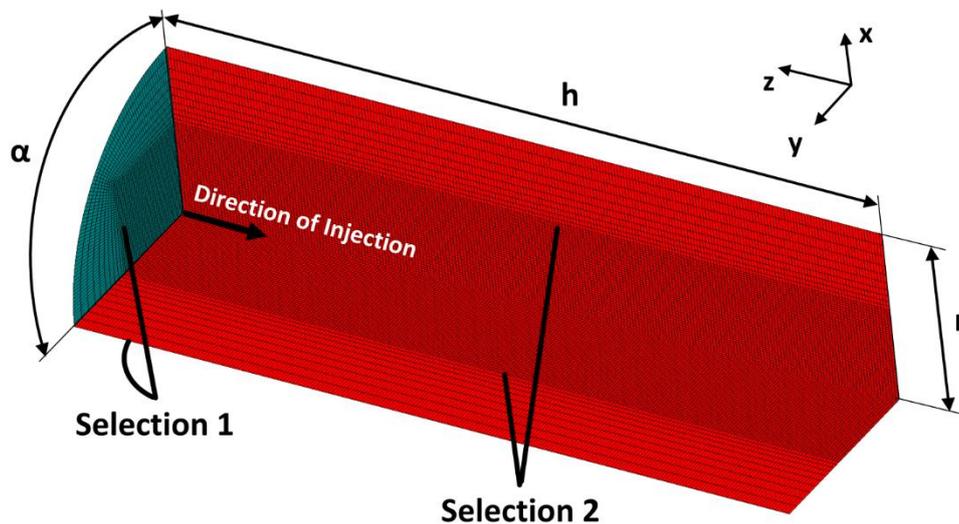


**Figure 37: Computational grid of the spray box**

The boundary conditions

- Selection 1: wall with $\vec{v}_{wall} = 0$ and $T_{wall} = T_{a,init}$

- Selection 2: symmetry planes

The simulation time step $\Delta t$ is $10^{-5}$ s.

Besides the Abramzon/Sirignano MC evaporation model in the simulations the aerodynamic WAVE droplet breakup model, the Schiller-Naumann drag model and the Gosman-Ioannides model for turbulent dispersion of the drops has been used. More details about the models can be found in the FIRE™ spray manual [53].

The initial fuel conditions are presented in Table 8.

**Table 8: Initial droplet parameters spray box cases**

| Case | Liquid | Mass Fraction [%] | init. Droplet Diameter [µm] | Droplet Temperature [K] | Velocity[1] [m/s] | Ambient Temperature [K] | Ambient Pressure [bar] |
|------|--------|-------------------|------------------------------|--------------------------|-------------------|-------------------------|-------------------------|
| 1 a | Decane | 50 | 140 | 353.3 | var | 760 | 73 |
| b | Hexadecane | 50 | 140 | 353.3 | var | 900 | 73 |

### 8.2.2. Investigation of the Vapour Mass Fractions

The focus of the analysis lies on the region where droplet evaporation happens. This is the region between nozzle orifice and liquid penetration depth of the fuel droplets. Here the vapour mass- fraction is shown as a colormap. Additionally, radial cuts are shown at the axial positions z= 5, 10 mm and 10, 20 mm and further an axial cut along the spray centerline. These will allow quantitative comparisons of the vapour mass-fraction in radial and axial direction respectively.

Besides the standard assumption of homogeneous droplet temperature (raping mixing approach) also the model for non-uniform droplet heating of Frolov, described in chapter 7.1.2, was activated and is compared with the rapid mixing model.

Figure 38 a) b) shows the evaporated mass- fraction of decane for the spray box case 1a for the old and modified real gas MC evaporation model. Only marginal differences in the mass-fraction can be seen in the colormap representation. This corresponds to the findings in the corresponding single droplet test shown in Figure 29 b) and Figure 30 b), where no significant differences occurred for the evaporation rate of decane.

[1]calculated from the injection rate diagram, needle diameter and fuel density

Highest mass-fractions are observed near the injection axis decreasing in radial direction. However, looking into more detail at the axial evolution of the decane vapor fraction in Figure 38 C-C, it can be observed that the decane mass-fraction is higher at the beginning for the mMC model. This is consistent with the finding in Figure 29, Figure 30, Figure 31 and Figure 33 for the single droplet test cases. Through the activation of the non-uniform droplet heating we expect higher temperatures at the droplet surface resulting in a higher evaporation rate and therefore higher mass fractions in vapour. This expectation was satisfied as the decane mass- fraction is higher. Also with the Frolov model differences between the oMC and mMC model are small.
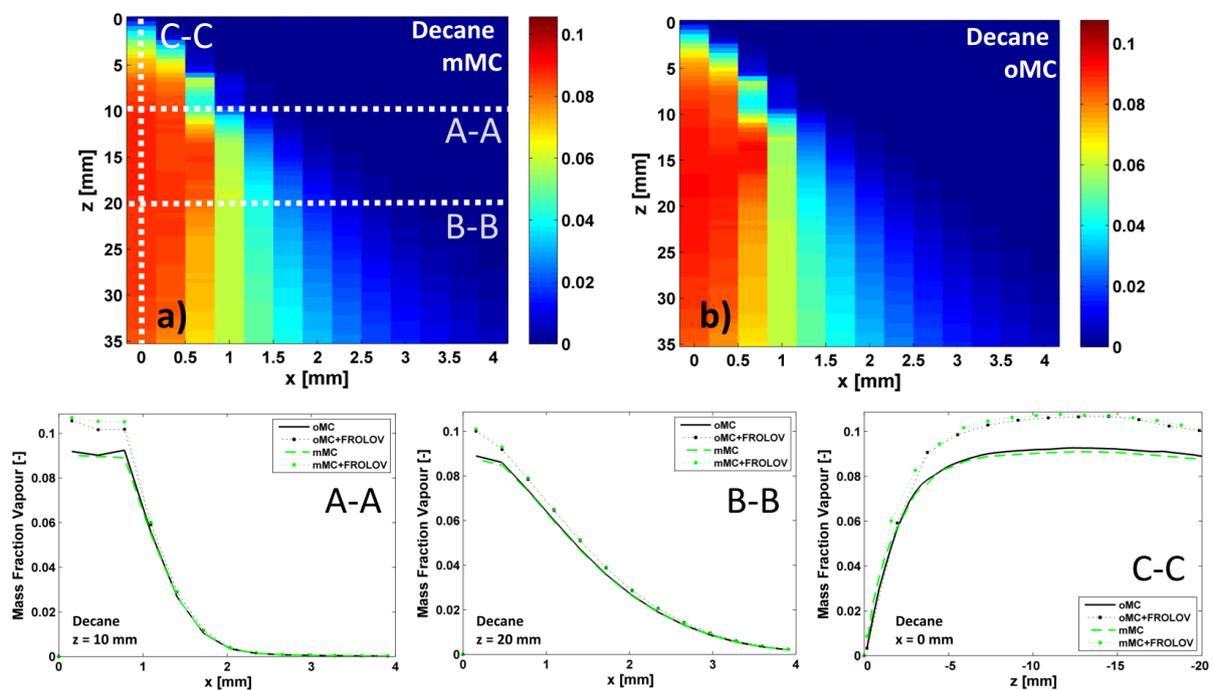


**Figure 38: Colormap for the decane vapour mass- fraction a) of the mMC and b) of the oMC model with cut planes z= 10 mm (A-A), z= 20 mm (B-B), x= 0 mm (C-C) at 760 K and 73 bar**

In Figure 39 a) b) the hexadecane mass- fraction is depicted for the same spray box case. The colormap representation of the relevant region shows a change that is due to the usage of the mMC model. Especially in the cuts (A-A, B-B, C-C) the overall higher mass-fractions of hexadecane can be seen. This is again similar to the single droplet cases where the less volatile component evaporation rate is significantly enhanced. For the non-uniform heating model the

differences between the oMC and mMC are significantly increased with even higher mass-fractions of hexadecane in vapour.
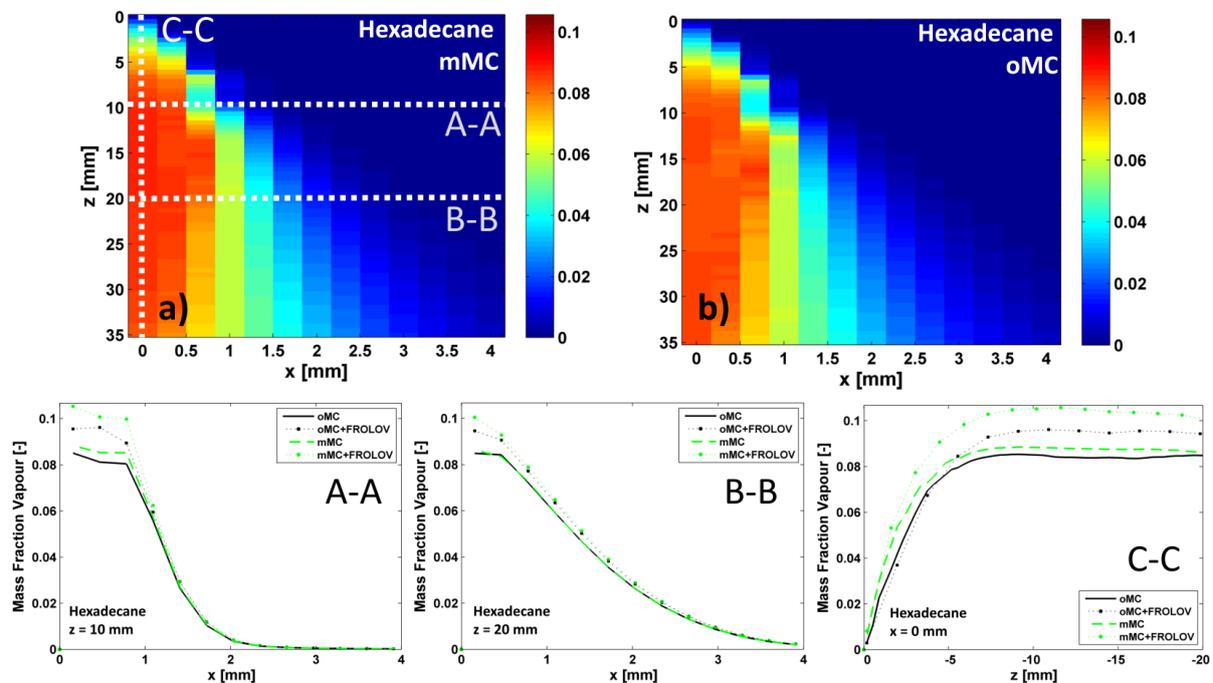


**Figure 39: Colormap for the hexadecane vapour mass- fraction a) of the mMC and b) of the oMC model with cut planes z= 10 mm (A-A), z= 20 mm (B-B), x= 0 mm (C-C) at 760 K and 73 bar**

Figure 40 displays the decane mass fraction for the spray box case 1b with an increased temperature at 900K. It can be seen that the mass- fractions are higher as generally the evaporation rate rises with increased temperature. In Figure 40 for the cuts z = 5 (A-A) and 10 mm (B-B) the decane vapour mole fraction of the oMC model is higher than that of the mMC model. With the non-uniform heating model for both decane and hexadecane with the mMC approach the vapour mass- fraction is higher than with the oMC approach.

Furthermore, in Figure 41 a) b) we can see the colormap of the mMC and oMC approach for the hexadecane mass-fractions. It is clearly visible that the hexadecane mass- fraction is elevated for the mMC approach along the direction of injection of the liquid fuel.
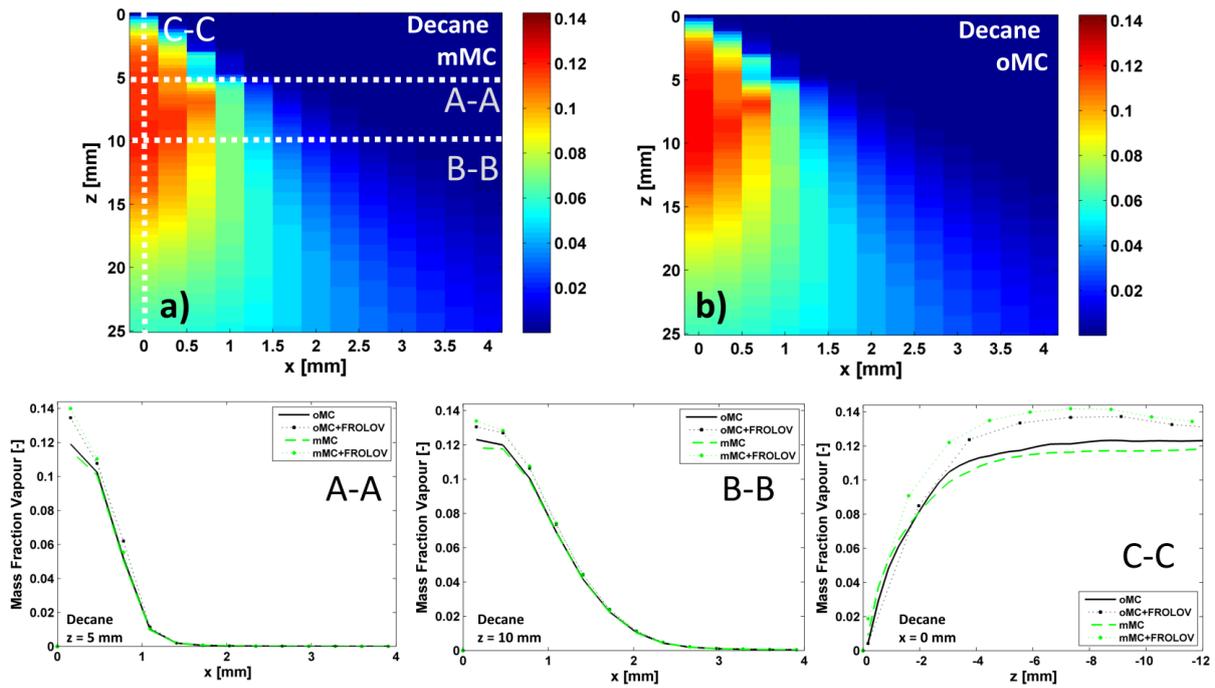
**Figure 40: Colormap for the decane vapour mass- fraction a) of the mMC and b) of the oMC model with cut planes z= 10 mm (A-A), z= 20 mm (B-B), x= 0 mm (C-C) at 900 K and 73 bar**
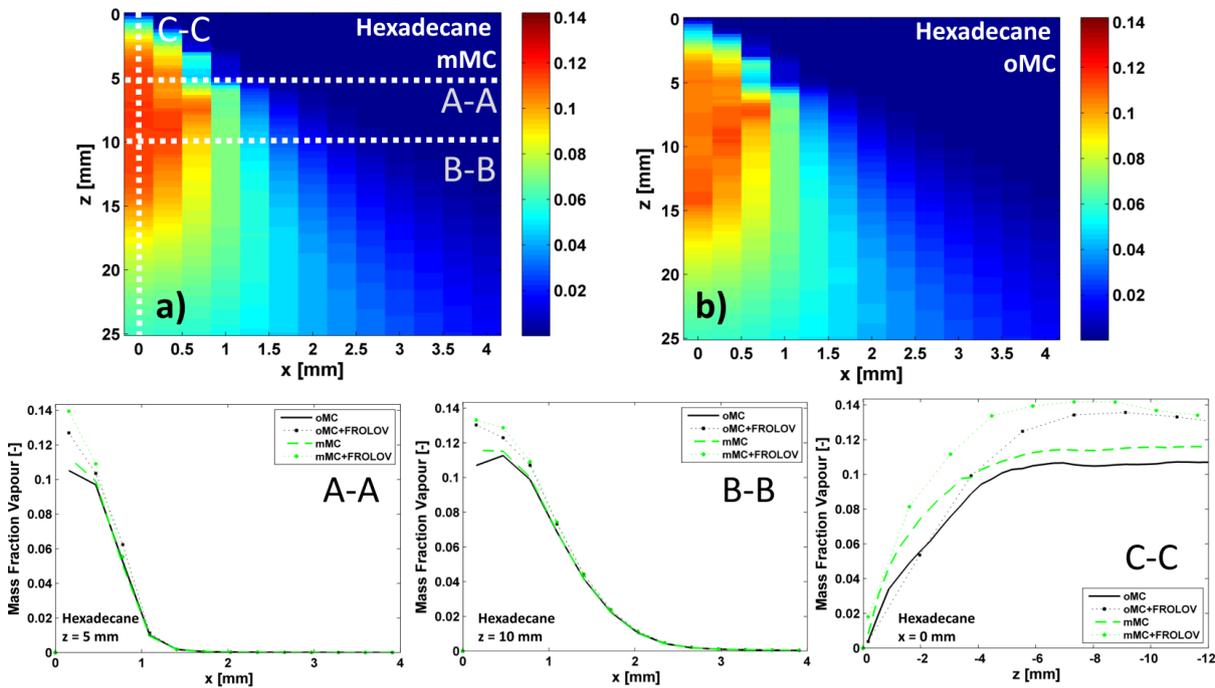


**Figure 41: Colormap for the decane vapour mass- fraction a) of the mMC and b) of the oMC model with cut planes z= 10 mm (A-A), z= 20 mm (B-B), x= 0 mm (C-C) at 900 K and 73 bar**

### 8.2.3. Penetration Lengths

The liquid and vapour penetrations for the two cases (1a and 1b) with the oMC and mMC model are investigated. The experimental data are taken from spray box tests at CMT Valencia [57]. The threshold value for the vapour penetration is $y_{v,\infty,\text{thres}} = 0.001$ for Figure 42 and Figure 43. The liquid penetration in the simulation is defined as average progression of 1% of the total mass at the leading edge of the spray cloud. The experimental data are gained from Schlieren and Mie-Scattering techniques for vapour and liquid respectively.

Figure 42 and Figure 43 show the liquid and vapour penetration for 760 K/ 900 K chamber temperature and 73 bar chamber pressure respectively. The experimental data are compared with the two models, oMC and mMC. Up to 250 µs after the start of injection the liquid penetration starts to deviate from the experimental data. The difference between the oMC and mMC model is minimal but still visible. Due to the overall higher evaporation rates the liquid and vapour penetration lengths are minimally reduced. The simulation overpredicts the liquid and vapour penetration lengths. For the non- uniform heating model the liquid penetration matches the experimental data, although again the differences between the oMC and mMC approach are small.
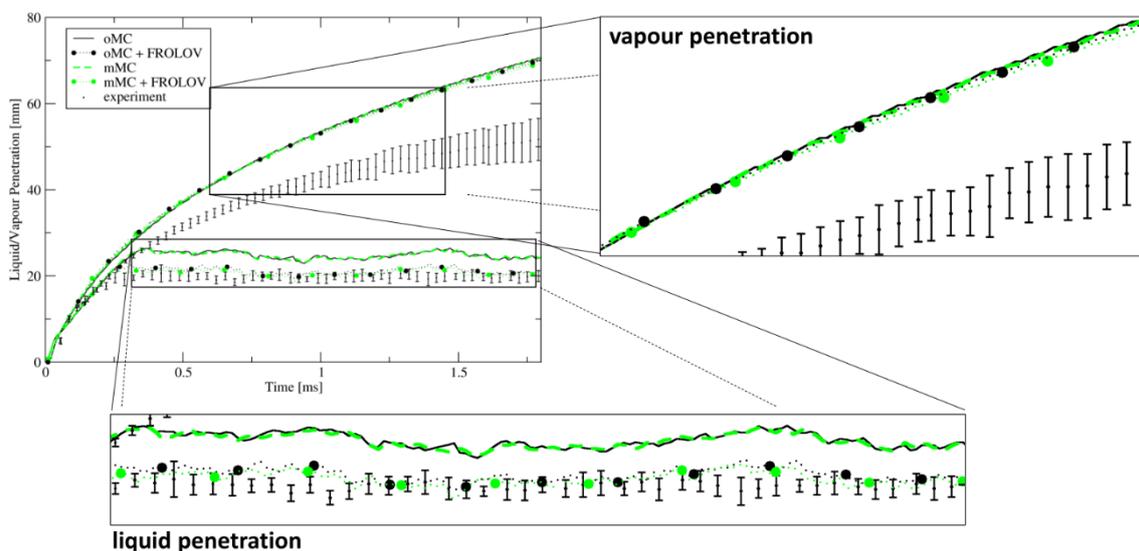


**Figure 42: Penetration of liquid and vapour of oMC, mMC model for 760 K and 73 bar**

A possible reason for these small differences is the integral nature of the penetration data, which levels out the local differences seen in the analysis of the vapour mass-fractions close to the injector.

In Figure 43, showing the high temperature case $T_a$ = 900 K, it can be observed that the simulation still overpredicts the experimental liquid and vapour penetration data, but the deviation is reduced for the liquid penetration. As the non-uniform heating is enabled, the simulation under predicts the liquid penetration of the experimental data. For both cases the vapour penetration length is only minimally influenced, as the vapour penetration is mainly dependent on the injection pressure/injection velocity which is the same for both cases.
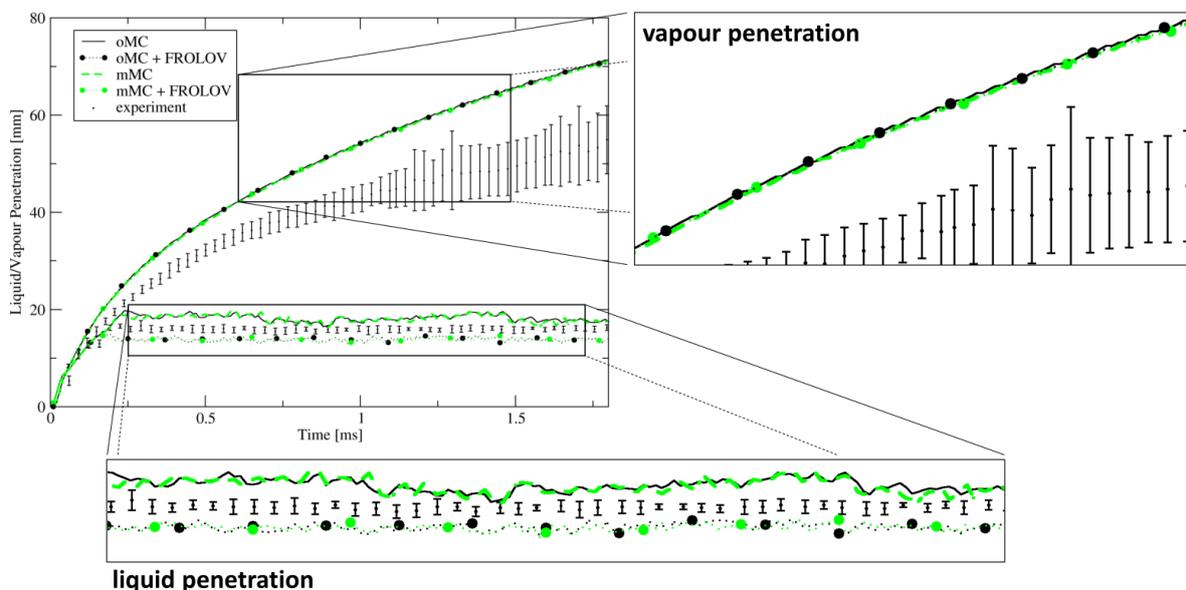


**Figure 43: Penetration of liquid and vapour of oMC, mMC model for 900 K and 73 bar**

### 8.2.4. Summary

The results seen in the vapour mass- fraction distribution correspond to the behavior as found in the single droplet simulations. The evaporation of the less volatile hexadecane is clearly enhanced. The evaporation of the more volatile component, decane is especially influenced by the higher droplet temperatures reached using the oMC model. Resulting in higher

evaporation rates for decane. However, overall the effects of the mMC model seem to be reduced in comparison with the single droplet simulations.

## 8.3. Engine Sector

This section contains the description and discussion of a simulation conducted under realistic engine conditions. A Volvo passenger car engine I5D with five cylinders operated at TU Graz (IVT) (see Figure 44) is used.
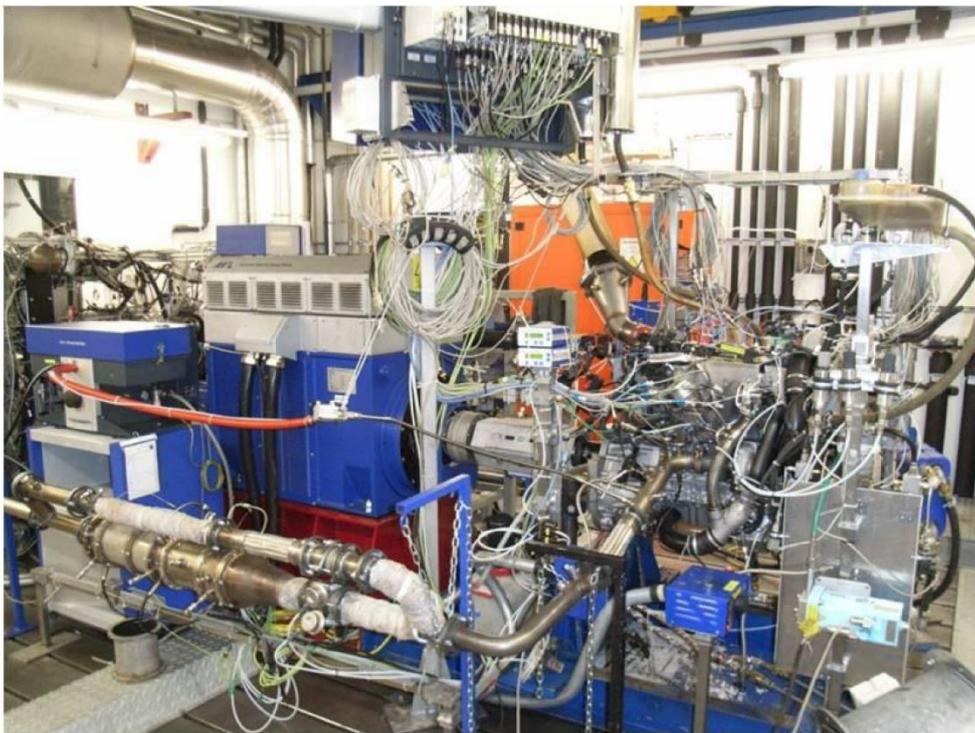


**Figure 44: Experimental setup Volvo I5D**

Engine cycles for a single cylinder have been simulated under various load conditions and for various real diesel fuels and surrogate fuels.

The calculations are made with a binary and a six-component diesel surrogate fuel determined by the CEET institute TU Graz seen in Table 9.

**Table 9: Initial droplet parameters engine sector case**

| Case | Liquid | mass fraction [%] | bore diameter [µm] | init. fuel temperature [K] |
|------|--------|-------------------|--------------------|----------------------------|
| 1 | Decane | 50 | 125 | 317.11 |
|   | Hexadecane | 50 | | |
| 2 | Toluene | 3 | 125 | 317.11 |
|   | Dodecane | 10 | | |
|   | Methylnapthalene | 25 | | |
|   | Hexadecane | 29 | | |
|   | Octadecane | 20 | | |
|   | Eicosane | 13 | | |

Case 1 has been selected for direct comparison with the single droplet and spray box tests, for which case 2 uses a more realistic diesel fuel surrogate.

### 8.3.1. Input Parameters and Geometry

As a rotationally symmetric seven hole injector has been used, the cases were simulated using a seventh part of an engine cylinder with periodic boundary conditions, which can be seen in Figure 45.
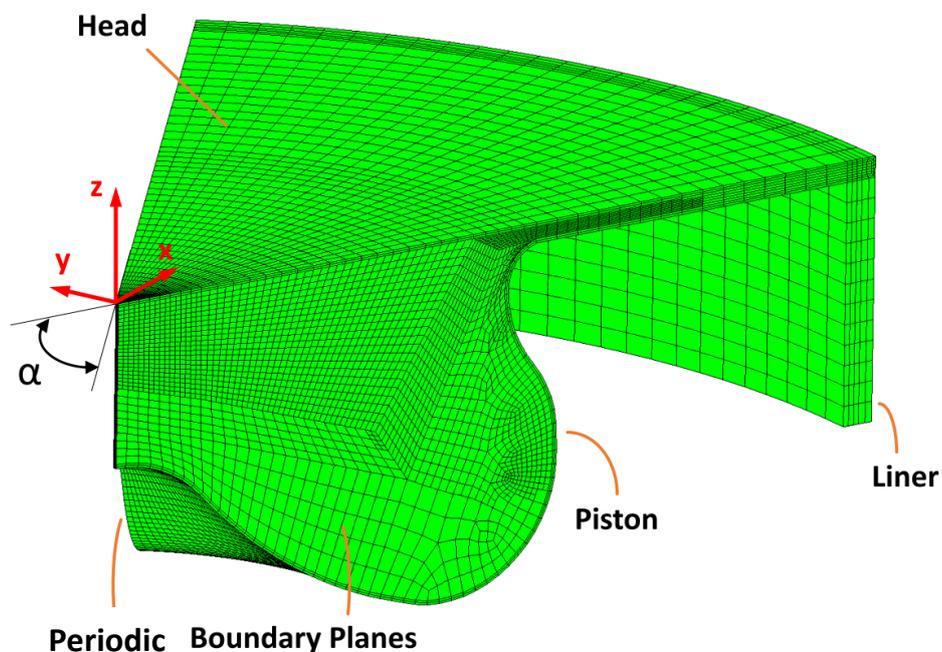


**Figure 45: Computational grid, diesel engine sector**

The boundary conditions are set to

- Piston: wall with $T_{wall} = 473K$ , moving mesh in z-direction

- Liner: wall with $T_{wall} = 423K$

- Head: wall $T_{wall} = 443K$

- Periodic Boundary Planes: Inlet/Outlet

The engine speed is set to 2000 1/min. The simulation starts at 585° CA (Crank Angle), for which the piston is at the bottom dead center and finishes at 855° CA. The injection is split into a pilot and main injection. The pilot injection starts at 702.1° CA and stops at 706.1 CA and the main injection starts at 718.5° CA and finishes at 730.1° CA. The geometrical data characterizing bore position and direction of injection are described in Figure 46.
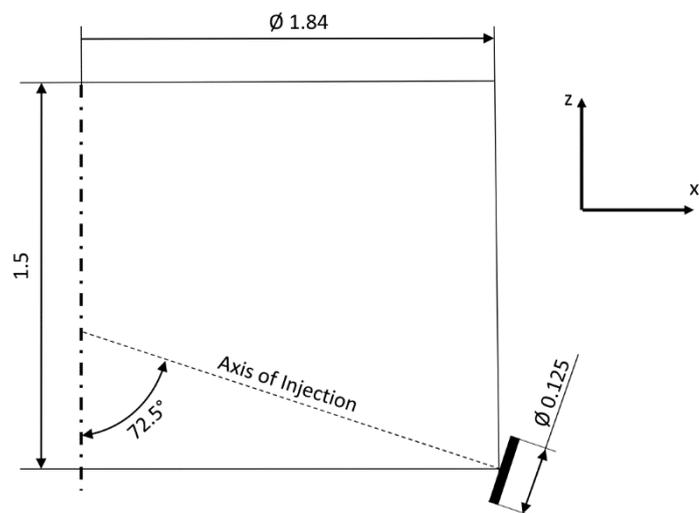


**Figure 46: Nozzle hole position [mm]**

The injected mass is 0.156 / 3.972 mg for the pilot and main injection respectively with the initial fuel temperature of 317.11 K.

For the simulation of the combustion and pollution formation the actual standard FIRE models have been used. These are the ECFM3Z multi-zone combustion model, the extended Zeldovich NOx formation model and the Kinetic SOOT model [53].

### 8.3.2. Results and Discussion

The results for the distribution of the vapour mass fraction of hexadecane in the direction of injection in case 1 are shown in Figure 47 and Figure 48. The vapour spray cloud at two crank

angle steps of 719.8° and 721° is depicted through a cut in the x-y plane a), b) and a profile along a polyline in the direction of injection c).

Immediately after the start of injection at 719.8° CA the less volatile hexadecane for the oMC approach, does not evaporate as quickly as with the mMC approach. The produced vapour of the mMC model exceeds the oMC model vapour production and the spatial expansion is reduced for the mMC model.
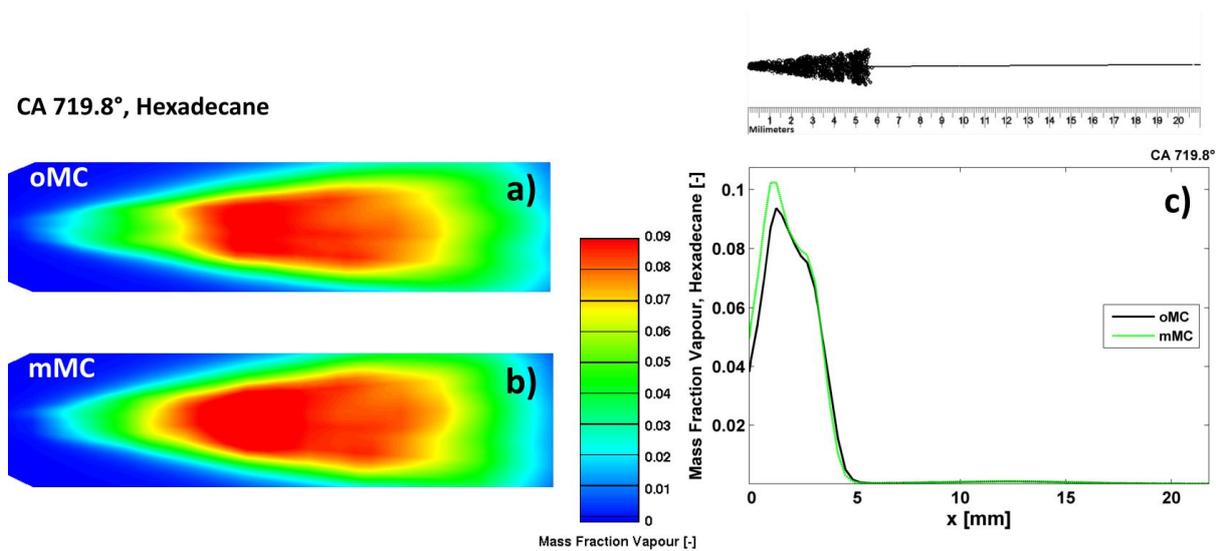


**Figure 47: Vapour mass fraction in a diesel engine sector from the oMC and mMC simulations a) old multicomponent model b) modified multicomponent model c) spray cloud and vapour mass fraction profiles along DOI**
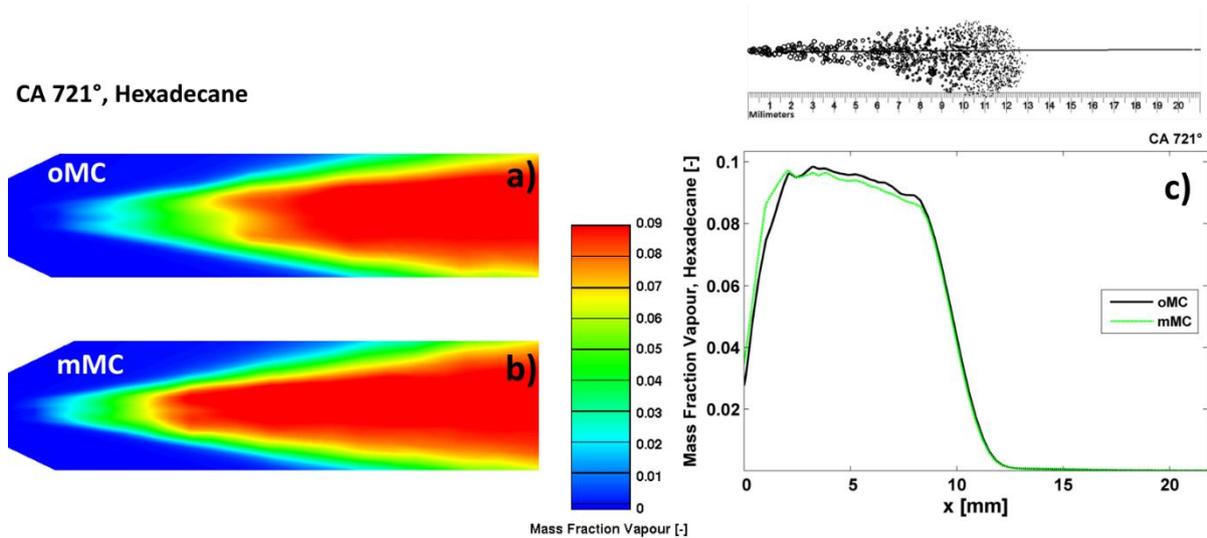


**Figure 48: Vapour mass fraction in a diesel engine sector from the oMC and mMC simulations a) old multicomponent model b) modified multicomponent model c) spray cloud and vapour mass fraction profiles along DOI**

At 721° CA the same characteristic as in 718.8° CA can be seen. Hexadecane vapour production is enhanced due to the mMC model a) and b). The main differences can be seen shortly after injection, with the differences decreasing in direction of the injection c). These temporally and spatially different vapour distributions shortly after injection can produce differences in the local ignition and combustion conditions.

However the deviations between most of the simulation results, over the whole computational domain of the oMC and mMC model, are negligible as seen in Figure 49 and Figure 50. With Figure 49 a) depicting the mean pressure inside the combustion chamber, b) the temperature of the combustion chamber and c) the rate of heat released by the diesel engine sector. Figure 50 a) shows a decline in the mean NOx mass fraction for the calculated mMC approach due to the different local temperatures which result in a somewhat lower average temperature level as can be in Figure 49 b) magnified region. In Figure 50 b) a similar mean SOOT mass fraction progression can be seen.
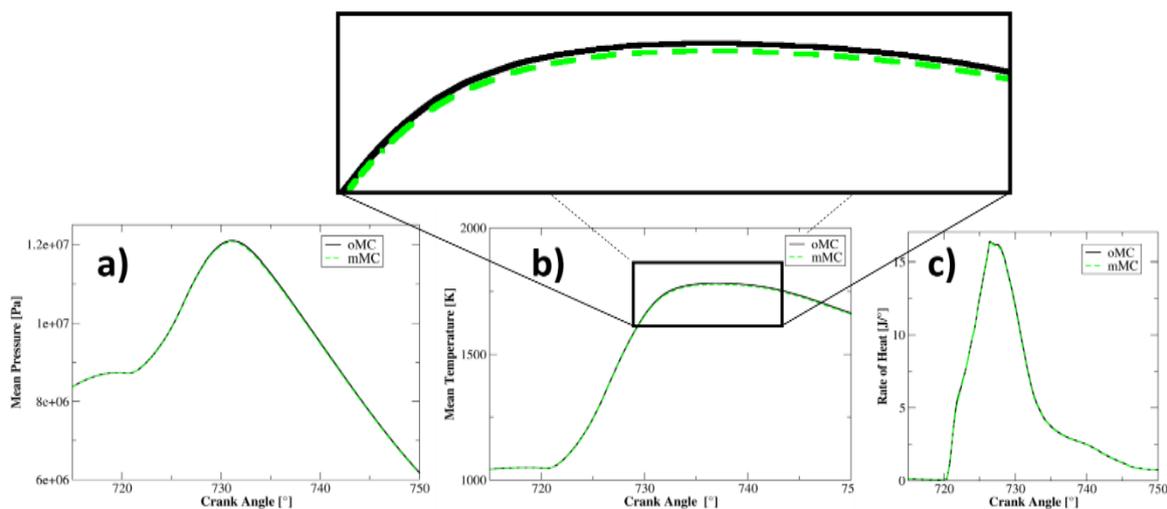


**Figure 49: (a) Mean pressure, (b) mean temperature, (c) rate of heat release in a diesel engine sector calculated with the oMC and mMC for case 1**
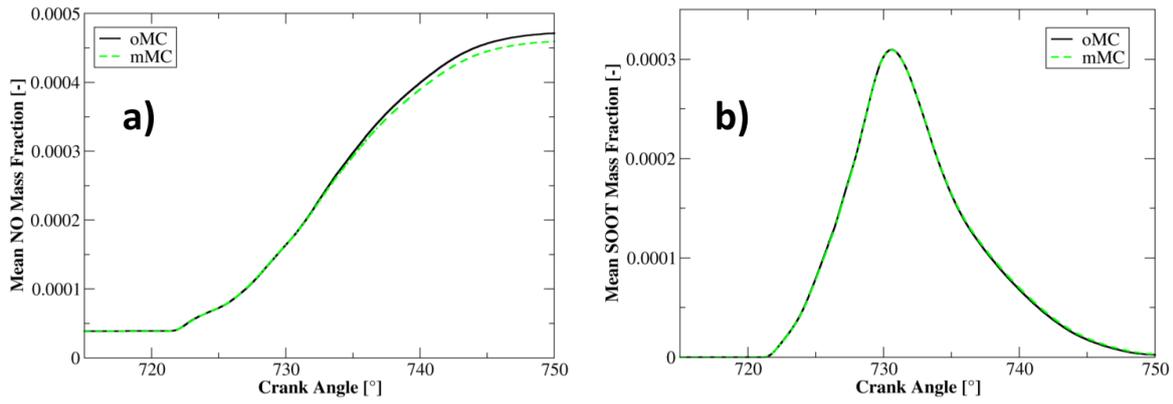
**Figure 50: (a) Mean NOx mass fraction, (b) mean SOOT mass fraction in a diesel engine sector calculated with the oMC and mMC for case 1**

For case 2, the six- component surrogate diesel fuel, experimental data are available [58]. Therefore the mean pressure, mean temperature and the rate of heat release can be compared with measured data. For case 2 the simulation was conducted with and without the non-uniform droplet heating model of Frolov. As can be seen in Figure 51 the oMC and mMC model without Frolov are almost identical although somewhat predicting the mean pressure and the mean temperature in comparison to the experimental data. With the non-uniform heating approach the oMC/ mMC model deviates further from the experimental results at the beginning of the main injection with the oMC and mMC model again very similar to each other. The increased evaporation temperature from the non-uniform heating model increases the mean temperature and therefore the pressure seen in Figure 52
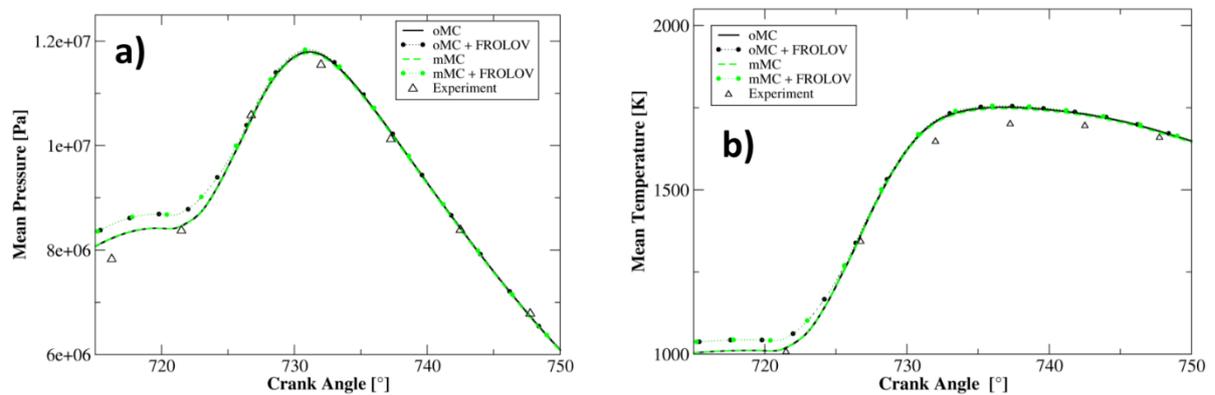


**Figure 51: (a) Mean pressure, (b) mean temperature in a diesel engine sector from the oMC and mMC for case 2**

The rate of heat release seen in Figure 52 is also almost identical for all models. The simulation data overpredicts the maximum of heat released during the injection, but underpredicts the rate of heat release after the injection. Furthermore the ignition detectable by the steep slope of the rate of heat release is delayed approximately 1° CA in comparison to the experimental data.
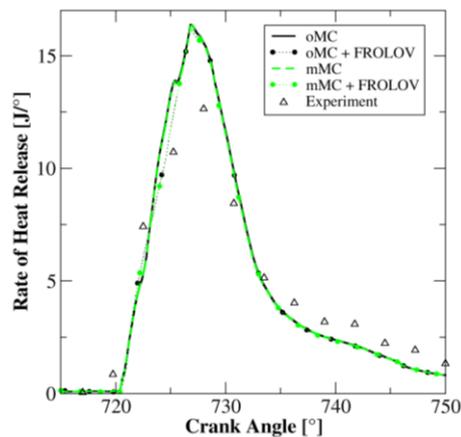


**Figure 52: Rate of heat release in a diesel engine sector from the oMC and mMC for case 2**

Figure 53 a) depicts the mean NOx mass fraction inside the combustion chamber. The mass fraction for the mean thermic NOx rises until the temperatures are too low for a further oxidation of nitrogen. With the non-uniform heating model the oMC and mMC approaches produce vapour more rapidly and are overall at a higher temperature at the beginning of the main injection. Predicting higher NOx mean mass fractions near the end of the combustion cycle. In case of the mMC model the NOx mean fraction is finally somewhat reduced as compared with the oMC model. This corresponds to the findings from Figure 50 a) for the binary surrogate. In Figure 53 b) the mean SOOT mass fraction is shown. Here the mMC and the oMC models with and without non-uniform heating are again practically identical. With non-uniform heating higher mean SOOT mass- fractions are reached.
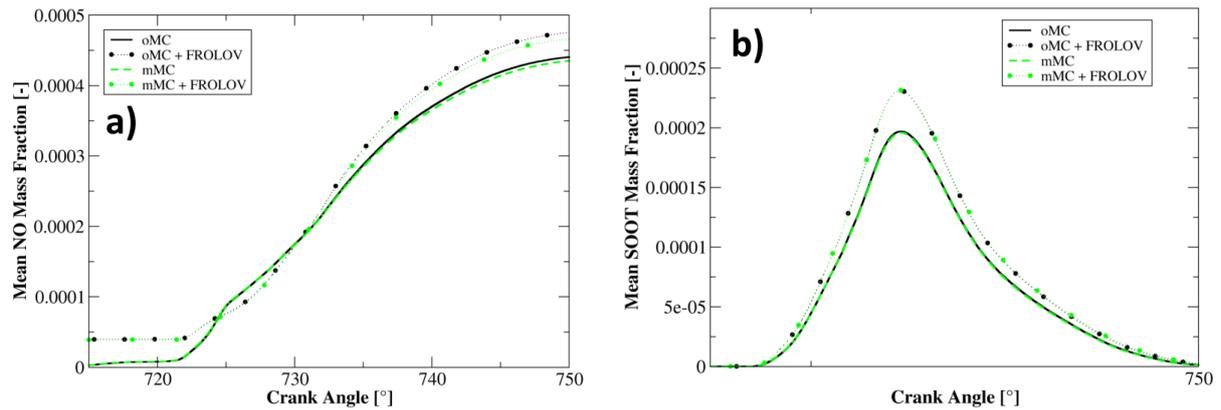
**Figure 53: (a) Mean NOx mass fraction, (b) mean SOOT mass fraction in a diesel engine sector from the oMC and mMC for case 2**

## 8.4. Summary

At the single droplet cases with different binary systems and a variation of physical parameters (pressure and temperature) it was observed that the droplet life time strongly depends on the evaporation rate of the less volatile component. Increased pressure extends the droplet evaporation time for both models which agrees with [1]. However, the mMC model gives smaller evaporation times for the low temperature test cases at 600 and 760 K for all pressure levels compared to the oMC model. For the high temperature test cases at 900 K the d²-curves show a trend for faster evaporation with the mMC model . Due to reaching critical mixture temperature earlier in the oMC case the evaporation of the oMC is higher than for the real gas mMC model.

Further, at least initially, enhanced evaporation rates could be found for the mMC model. Especially for the low volatility component also the maximum evaporation rate is enhanced in the new mMC approach.

The liquid and vapour penetrations and as well the vapour distribution of the spray box for the two presented cases have been investigated with and without the non-uniform heating model of Frolov, especially in regard to the evaporated mass-fractions of the used components. We have seen results similar to the single droplet studies, as the vapour production of the less volatile component is increased close to the injector and accordingly the overall vapour production in the mentioned region is increased. This is in agreement with results that were found for real gas/ ideal gas comparisons of single component systems in [2]

and [1]. However, overall penetration results for liquid and vapour are only marginally different due to the integral character of these entities.

A real engine case in form of a diesel engine sector with a moving piston, an initial swirl and a realistic time evolution of the pilot and main injection rate was simulated. Two fuels, a binary mixture and a six component diesel surrogate have been used in the simulations and compared with experimental data for the surrogate case. For the vapour mass-fraction along a polyline the same enhancement of the less volatile component was encountered near the nozzle. The integral values of the results, like pressure and temperature are very similar between the oMC and mMC model with no drastic changes seen. However, the NOx mass fractions show small, but anyway noticeable differences between the oMC and the mMC model. The SOOT mean mass- fractions show nearly no differences between oMC and mMC model, but are remarkably different with the non-uniform heating model. However, no final conclusion on the overall impact of the new model can be drawn, since a comprehensive testing over relevant load cases and various surrogate fuels still needs to be done.

Despite the small differences in overall combustion results between the oMC and mMC model, it is expected that the consideration of real gas effects will be an important precondition for more elaborate combustion and pollution formation models, which take into account the detailed vapour composition in thorough combustion chemistry. The present standard ECM3Z combustion model and the kinetic soot model do not yet treat the various fuel components separately, which might explain the small impact of the new approach on the global results.

# 9. Conclusion

This thesis has shown the effects from the departure of ideal gas behavior in the phase equilibrium relationship for single droplets and fuel sprays under engine conditions. The UGC VTPR EoS was implemented for this task using the latest parameters available in literature. The model can be easily extended for further parameters that might be released in the future. Validation of the VLE- implementation with published experimental data showed good agreement.

For high pressures, multi-component droplet evaporation experiments are rare. Experimental data from spray box and engine cases are used instead. In all cases analyzed for vapour mass fractions it was shown that the less volatile component evaporation rates are enhanced with the use of the mMC model.

Concerning the model efficiency, the mMC model and oMC differ in calculation time of approximately a magnitude of 2-10 dependent on the temperature and pressure used. I.e. for temperatures near the critical temperature the successive substitution technique becomes slow to reach the targeted accuracy. For the Diesel engine sector case the computational time is increased by approximately 20% per piston cycle.

To gain more insight on the overall real gas effects in the future, it would be interesting to focus on

- taking into account real gas effects in the gaseous phase inside the residence cell of the droplet (excess enthalpies and excess specific heat capacities)
- calculation of thermophysical properties, e.g. latent heats, densities from EoS data, if proper mixing parameters are available
- the diffusion inside the droplet. Highly volatile components evaporate faster and the less volatile components enrich the outer layer of the droplet. Therefore the limitation of the mass-transfer of the various components might additionally change the evaporation characteristics of the droplets.

Further the implementation of the real gas behavior in the gas- phase surrounding the droplet and in the overall gas flow solver should be a goal.

Additionally the numerical methods how the VLE is solved can be further improved by more optimized and advanced calculation algorithms. (E.g. Accelerated Successive Substitution, the Nelder-Mead Simplex or a quasi-Newton methods).

Based on the differences in local vapour concentration, it will become even more interesting if various fuel components are also taken into account in the chemical reactions of combustion as the present standard ECM3Z combustion model does not treat the various fuel components separately. The implementation of corresponding chemical reactions would also allow for a more precise exhaust gas calculation.

For these future developments the new evaporation model can be especially useful by providing a more accurate information about the local distribution of the various fuel components.

# 10. References

[1]    M.F. Trujillo, D.J. Torres, P.J. O'Rourke, High-pressure multicomponent liquid sprays: departure from ideal behaviour, Int. J. Engine Res. 5 (2004) 229–246.

[2]    K. Prommersberger, J. Stengele, K. Dullenkopf, J. Himmelsbach, S. Wittig, Investigations of Droplet Evaporation at Elevated Pressures, in: High Intensity Combustors – Steady Isobaric Combust., Wiley-VCH Verlag GmbH & Co. KGaA, 2005: pp. 54–72. doi:10.1002/3527601996.ch3.

[3]    H. Nomura, Y. Ujiie, H.J. Rath, J. Sato, M. Kono, Experimental study on high-pressure droplet evaporation using microgravity conditions, in: Symp. Combust., Elsevier, 1996: pp. 1267–1273.

[4]    B. Abramzon, W.A. Sirignano, Droplet vaporization model for spray combustion calculations, Int. J. Heat Mass Transf. 32 (1989) 1605–1618. doi:http://dx.doi.org/10.1016/0017-9310(89)90043-4.

[5]    G. Brenn, L.J. Deviprasath, F. Durst, Computations and experiments on the evaporation of multi-component droplets, in: Proc. Ninth Int. Conf. Liq. At. Spray Syst. (ICLASS), Sorrento, Italy, 2003.

[6]    S.M. Frolov, F.S. Frolov, B. Basara, Simple model of transient drop vaporization, J. Russ. Laser Res. 27 (2006) 562–574. doi:10.1007/s10946-006-0035-7.

[7]    J.M. Prausnitz, R.N. Lichtenthaler, E.G. de Azevedo, Molecular thermodynamics of fluid-phase equilibria, Pearson Education, 1998.

[8]    J.M. Smith, H.C. Van Ness, M.M. Abbott, Introduction to chemical engineering thermodynamics., McGraw-Hill, Boston, 2005.

[9]    G.N. Lewis, The law of physico-chemical change, in: Proc. Am. Acad. Arts Sci., 1901: pp. 49–69.

[10]    R. Dohrn, Berechnung von Phasengleichgewichten : mit 14 Tabellen, Vieweg, Braunschweig; Wiesbaden, 1994.

[11]    S.I. Sandler, Models for Thermodynamic and Phase Equilibria Calculations, Taylor & Francis, 1993.

[12]    J. Gmehling, B. Kolbe, M. Kleiber, J. Rarey, Chemical thermodynamics for process simulation, John Wiley & Sons, 2012.

[13]    J.D. der Waals, Over de Continuiteit van den Gas-en Vloeistoftoestand, Sijthoff, 1873.

[14]    O. Redlich, J.N.S. Kwong, On the thermodynamics of solutions. V. An equation of state. Fugacities of gaseous solutions., Chem. Rev. 44 (1949) 233–244.

[15]    G. Soave, Equilibrium constants from a modified Redlich-Kwong equation of state, Chem. Eng. Sci. 27 (1972) 1197–1203.

[16]    D.-Y. Peng, D.B. Robinson, A new two-constant equation of state, Ind. Eng. Chem. Fundam. 15 (1976) 59–64.

[17]    E.W. Lemmon, M.O. McLinden, D.G. Friend, Thermophysical properties of fluid systems, NIST Chem. Webbook, NIST Stand. Ref. Database. 69 (2016).

[18]    G.M. Wilson, Calculation of enthalpy data from a modified Redlich-Kwong equation of

state, in: Adv. Cryog. Eng., Springer, 1966: pp. 392–400.

[19]    B.E.. Poling, The Properties Of Gases And Liquids, McGraw-Hill New York, 2001.

[20]    R. Stryjek, J.H. Vera, PRSV: An improved Peng-Robinson equation of state for pure compounds and mixtures, Can. J. Chem. Eng. 64 (1986) 323–333.

[21]    C.H. Twu, J.E. Coon, J.R. Cunningham, A new generalized alpha function for a cubic equation of state Part 2. Redlich-Kwong equation, Fluid Phase Equilib. 105 (1995) 61–69.

[22]    K.S. Pitzer, Corresponding states for perfect liquids, J. Chem. Phys. 7 (1939) 583–590.

[23]    B. Schmid, J. Gmehling, The universal group contribution equation of state VTPR present status and potential for process development, Fluid Phase Equilib. 302 (2011) 213–219.

[24]    J. Ahlers, J. Gmehling, Development of an universal group contribution equation of state: I. Prediction of liquid densities for pure compounds with a volume translated Peng–Robinson equation of state, Fluid Phase Equilib. 191 (2001) 177–188. doi:http://dx.doi.org/10.1016/S0378-3812(01)00626-4.

[25]    U.K. Deiters, Calculation of densities from cubic equations of state, AIChE J. 48 (2002) 882–886.

[26]    J.P. O'Connell, J.M. Haile, Thermodynamics: Fundamentals for Applications, Cambridge University Press, 2005.

[27]    E.A. Guggenheim, Mixtures: the theory of the equilibrium properties of some simple classes of mixtures, solutions and alloys, Clarendon Press, 1952.

[28]    D.S. Abrams, J.M. Prausnitz, Statistical thermodynamics of liquid mixtures: a new expression for the excess Gibbs energy of partly or completely miscible systems, AIChE J. 21 (1975) 116–128.

[29]    P. Stephan, K. Schaber, K. Stephan, F. Mayinger, Thermodynamik - Grundlagen und technische Anwendungen Band 2: Mehrstoffsysteme und chemische Reaktionen, 15th ed., Springer-Verlag Berlin Heidelberg, 2010. doi:10.1007/978-3-540-36855-7.

[30]    A. Fredenslund, R.L. Jones, J.M. Prausnitz, Group-contribution estimation of activity coefficients in nonideal liquid mixtures, AIChE J. 21 (1975) 1086–1099.

[31]    Dortmund Data Bank, (2015). www.ddbst.de.

[32]    U. Weidlich, J. Gmehling, A modified UNIFAC model. 1. Prediction of VLE, hE, and. gamma.. infin., Ind. Eng. Chem. Res. 26 (1987) 1372–1381.

[33]    T. Holderbaum, J. Gmehling, PSRK: A group contribution equation of state based on UNIFAC, Fluid Phase Equilib. 70 (1991) 251–265.

[34]    B. Schmid, A. Schedemann, J. Gmehling, Extension of the VTPR group contribution equation of state: group interaction parameters for additional 192 group combinations and typical results, Ind. Eng. Chem. Res. 53 (2014) 3393–3405.

[35]    G.M. Kontogeorgis, P. Coutsikos, Thirty Years with EoS/GE Models? What Have We Learned?, Ind. Eng. Chem. Res. 51 (2012) 4119–4142.

[36]    G. Kontogeorgis, G. Folas, Thermodynamic Models for Industrial Applications From Classical and Advanced Mixing Rules to Association Theories, n.d.

[37]    J.-N. Jaubert, F. Mutelet, VLE predictions with the Peng–Robinson equation of state and temperature dependent kij calculated through a group contribution method, Fluid Phase Equilib. 224 (2004) 285–304. doi:http://dx.doi.org/10.1016/j.fluid.2004.06.059.

[38]    C. Boukouvalas, N. Spiliotis, P. Coutsikos, N. Tzouvaras, D. Tassios, Prediction of vapor-liquid equilibrium with the LCVM model: a linear combination of the Vidal and Michelsen mixing rules coupled with the original UNIF, Fluid Phase Equilib. 92 (1994) 75–106. doi:http://dx.doi.org/10.1016/0378-3812(94)80043-X.

[39]    J. Seo, J. Lee, H. Kim, Isothermal vapor-liquid equilibria for the system ethanol and n-hexane in the near critical region, Fluid Phase Equilib. 182 (2001) 199–207. doi:10.1016/S0378-3812(01)00395-8.

[40]    R.A. Heidemann, M.L. Michelsen, Instability of Successive Substitution, Ind. Eng. Chem. Res. 34 (1995) 958–966. doi:10.1021/ie00042a032.

[41]    K.L. Butcher, M.S. Medani, Thermodynamic properties of methanol–benzene mixtures at elevated temperatures, J. Appl. Chem. 18 (1968) 100–107. doi:10.1002/jctb.5010180402.

[42]    Jungha Seo, Sanghak Lee, and Hwayong Kim*, Measurement and Correlation of Vapor–Liquid Equilibria for the Ethanol + n-Heptane System near the Critical Region, J. Chem. Eng. Data. 47 (2002) 974–977. doi:10.1021/je0200057.

[43]    J. Seo, S. Lee, H. Kim, Measurement and correlation of vapor-liquid equilibria for the ethanol+ n-heptane system near the critical region, J. Chem. Eng. Data. 47 (2002) 974–977.

[44]    K.L. Butcher, K.R. Ramasubramanian, M.S. Medani, Thermodynamic properties of the benzene and n-heptane system at elevated temperatures, J. Appl. Chem. Biotechnol. 22 (1972) 1139–1155. doi:10.1002/jctb.5020221103.

[45]    M.L. McGlashan, A.G. Williamson, Thermodynamics of mixtures of n-hexane+ n-hexadecane. Part 2.Vapour pressures and activity coefficients, Trans. Faraday Soc. 57 (1961) 588–600. doi:10.1039/TF9615700588.

[46]    P.C. Joyce, M.C. Thies, Vapor-liquid equilibria for the hexane+ hexadecane and hexane+ 1-hexadecanol systems at elevated temperatures and pressures, J. Chem. Eng. Data. 43 (1998) 819–822. doi:10.1021/je980037n.

[47]    F. Barr-David, B.F. Dodge, Vapor-Liquid Equilibrium at High Pressures. The Systems Ethanol - Water and 2-Propanol - Water, J. Chem. Eng. Data. 4 (1959) 107–121. doi:10.1021/je60002a003.

[48]    R.F. Rodrigues, I.C. Costa, F.B. Almeida, R.A.S. Cruz, A.M. Ferreira, J.C.E. Vilhena, et al., Development and characterization of evening primrose (Oenothera biennis) oil nanoemulsions, Rev. Bras. Farmacogn. 25 (2015) 422–425. http://www.scielo.br/scielo.php?script=sci_arttext&pid=S0102-695X2015000400422&nrm=iso.

[49]    B. Schmid, Einsatz einer modernen Gruppenbeitragszustandsgleichung für die Synthese thermischer Trennprozesse, Carl von Ossietzky Universität Oldenburg, 2011.

[50]    F. García-Sánchez, G. Eliosa-Jiménez, G. Silva-Oliver, B.E. García-Flores, Vapor–Liquid Equilibrium Data for the Nitrogen + n-Decane System from (344 to 563) K and at Pressures up to 50 MPa, J. Chem. Eng. Data. 54 (2009) 1560–1568.

doi:10.1021/je800881t.

[51]   H.-M. Lin, H. Kim, K.-C. Chao, Gas-liquid equilibria in nitrogen + n-hexadecane mixtures at elevated temperatures and pressures, Fluid Phase Equilib. 7 (1981) 181–185. doi:http://dx.doi.org/10.1016/0378-3812(81)85020-0.

[52]   C. Fink, A multi-component evaporation model for 3D CFD-code Fire 8: development and validation with experimental data, TU Graz, 2005.

[53]   AVL-AST, FIRE Manual v2014.2, AVL List GmbH, Graz. (2016).

[54]   V. Bermúdez, J.M. Garcia, E. Juliá, S. Martínez, Engine with Optically Accessible Cylinder Head: A Research Tool for Injection and Combustion Processes, 2003. doi:10.4271/2003-01-1110.

[55]   J. V Pastor, J.M. García-Oliver, J.-G. Nerva, B. Giménez, Fuel effect on the liquid-phase penetration of an evaporating spray under transient diesel-like conditions, Fuel. 90 (2011) 3369–3381.

[56]   J. V Pastor, R. Payri, J.M. Garcia-Oliver, J.-G. Nerva, Schlieren measurements of the ECN-spray A penetration under inert and reacting conditions, SAE Technical Paper, 2012.

[57]   J. V Pastor, J.M. Garcia-oliver, V. Bermudez, C. Micó, Spray Characterization for Pure Fuel and Binary Blends under Non-Reacting Conditions, 2014. doi:10.4271/2014-01-1407.Copyright.

[58]   S. Möller, G.K. Dutzler, P. Priesching, J.M. Garcia-Oliver, G. Pirker, W. Payer, Multi-Component Diesel Spray and Combustion Modelling, in: AVL Adv. Simul. Technol. - Int. User Conf. 2013, 2013: p. 16.

[59]   C. Antoine, Tensions des vapeurs; nouvelle relation entre les tensions et les températures, Comptes Rendus Des Séances l'Académie Des Sci. 107 (1888) 681–684.

# Appendix A - Thermodynamic Properties

Table A-1 contains for the AVL FIRE™ database selected property values.

With $T_c$ as critical temperature, $P_c$ as critical pressure, $\omega$ as acentric factor, $Z_c$ as critical real gas factor and $V_c$ as critical molar density.

**Table A-1: Thermodynamic properties**

| | Properties | | | | | | |
|---|---|---|---|---|---|---|---|
| | $T_c$ | $P_c$ | $\omega$ | $Z_c$ | Mol Wgt. | $V_c$ | |
| | [K] | [bar] | [-] | [-] | [g/mol] | [cm³/mol] | Ref. |
| **Inorganic** | | | | | | | |
| water | 647.1 | 220.64 | 0.308 | 0.2294 | 18.0153 | 57.1 | [1] |
| nitrogen | 126.2 | 33.98 | 0.037 | 0.289 | 28.0134 | 90.1 | [1] |
| oxygen | 154.58 | 50.43 | 0.02128 | 0.288 | 31.9988 | 73.5294 | [1] |
| carbondioxide | 304.12 | 73.74 | 0.225 | 0.2746 | 44.0095 | 91.9 | [1] |
| | | | | | | | |
| **Organic Hydrocarbons** | | | | | | | |
| methane | 190.56 | 45.99 | 0.011 | 0.2874 | 16.0425 | 99.2 | [1] |
| ethane | 305 | 49 | 0.099 | 0.2793 | 30.069 | 147 | [1] |
| propane | 369.9 | 42.5 | 0.252 | 0.27639 | 44.0956 | 200 | [1] |
| butane | 425.12 | 37.96 | 0.2 | 0.274 | 58.1222 | 255 | [1] |
| pentane | 469.8 | 33.6 | 0.252 | 0.268 | 72.15 | 311 | [1] |
| hexane | 507.6 | 30.25 | 0.3 | 0.2644 | 86.1754 | 370 | [1] |
| heptane | 540 | 27.4 | 0.349 | 0.2633 | 100.2019 | 243 | [1] |
| octane | 568.7 | 24.9 | 0.399 | 0.259 | 114.2285 | 243 | [1] |
| decane | 617.8 | 21.1 | 0.49 | 0.262 | 142.2817 | 603 | [1] |
| dodecane | 658 | 18.2 | 0.576 | 0.251 | 170.3348 | 713 | [1] |
| tridecane | 676 | 17.2 | 0.618 | 0.251867 | 184.3614 | 823 | [1] |
| tetradecane | 693 | 15.73 | 0.644 | 0.244075 | 198.388 | 894 | [1] |
| hexadecane | 723 | 14 | 0.718 | 0.241 | 226.4412 | 1034 | [1] |
| octadecane | 747 | 12 | 0.8 | 0.2275 | 254.504 | 1058 | [1] |
| eicosane | 768 | 10.7 | 0.865 | 0.209 | 282.5475 | 1177 | [1] |
| | | | | | | | |
| isopentane | 460.43 | 30.4 | 0.229 | 0.263 | 72.15 | 304 | [1] |
| benzene | 562.1 | 48.93997 | 0.212 | 0.2712 | 78.114 | 259 | [1] |
| toluene | 591.79 | 41.086 | 0.264 | 0.264 | 92.1384 | 316 | [1] |
| isooctane | 543.9 | 25.7 | 0.304 | 0.259 | 114.23266 | 468 | [1] |
| methylnaphtalene | 772 | 36 | 0.348 | 0.234 | 142.201 | 462 | [1] |
| | | | | | | | |
| **Alcohols** | | | | | | | |
| methanol | 513 | 81 | 0.565 | 0.222 | 32.0419 | 118 | [1] |

| | | | | | | | |
|---|---|---|---|---|---|---|---|
| ethanol | 513.93 | 61.48 | 0.649 | 0.2484 | 46.0684 | 167.1 | [1] |
| butanol | 563.1 | 44.2 | 0.59 | 0.259 | 74.123 | 275 | [1] |

References

[1]    B.E.. Poling, The Properties Of Gases And Liquids, McGraw-Hill New York, 2001.

# Appendix B -  Antoine Parameters

Based on the Clapeyron Equation, Antoine proposed [59] an empirical modification leading to the Antoine Equation

$$\log_{10} P^s = A - \frac{B}{C+T}$$ (B.1)

where $P^s$ is the saturation pressure of the fluid at T, the temperature of the fluid. The Antoine constants in are calculated and found in literature with $P^s$ in bar and T in K.

**Table B-1: Antoine constants**

| | Antoine constants | | | | |
|---|---|---|---|---|---|
| | A | B | C | T- range [K] | Reference |
| Inorganic | | | | | |
| nitrogen | 3.7362 | 264.651 | -6.788 | 63 - 126 | [1] |
| carbondioxide | 4.65139 | 835.06 | -4.927 | 150 - 250 | ** |
| oxygen | 3.9523 | 340.024 | -4.144 | 54 - 154 | [2] |
| water | 5.2711 | 1810.9694 | -29.2435 | 350 - 647 | [3]* |
| Organic | | | | | |
| methane | 3.9895 | 443.028 | -0.49 | 91 - 190 | [4] |
| ethane | 3.93835 | 659.739 | -16.719 | 135 - 200 | NIST |
| propane | 4.5367 | 1149.36 | 24.906 | 278 - 361 | NIST |
| pentane | 4.1899 | 1180.0936 | -28.0322 | 350 - 470 | [5]* |
| n-butane | 4.35576 | 1175.581 | -2.071 | 273 - 425 | [6] |
| hexane | 4.0373 | 1170.50856 | -52.135 | 350 - 507 | [7]* |
| heptane | 4.0458 | 1268.7665 | -57.4546 | 350 - 540 | [8]* |
| octane | 4.04867 | 1355.126 | -63.633 | 326 - 400 | NIST |
| decane | 4.07857 | 1501.268 | -78.67 | 368 - 488 | NIST |
| dodecane | 4.10549 | 1625.928 | -92.839 | 400 - 491 | NIST |
| tridecane | 4.12829 | 1689.093 | -98.866 | 412 - 510 | NIST |

| | | | | | |
|---|---|---|---|---|---|
| tetradecane | 4.13735 | 1739.623 | -105.616 | 428 - 527 | *** |
| hexadecane | 4.2615 | 1831.0194 | 122.9377 | 450 - 723 | ** |
| octadecane | 4.33209 | 2068.963 | -111.927 | 447 - 590 | NIST |
| eicosane | 4.27139 | 2032.7 | -141.15 | 450 - 768 | ** |
| | | | | | |
| benzene | 3.99906 | 1196.76 | -53.989 | 350 - 562 | [9]* |
| toluene | 4.54436 | 1738.123 | 0.394 | 420 - 580 | ** |
| isopentane | 3.97183 | 1021.864 | -43.231 | 350 - 460 | ** |
| isooctane | 3.93679 | 1257.84 | -52.415 | 350 - 543 | ** |
| methylnaphtalene | 4.16082 | 1826.928 | -78.148 | 450 - 772 | ** |
| Alcohols | | | | | |
| methanol | 5.1795 | 1568.9521 | -34.4869 | 350 - 513 | [10]* |
| ethanol | 4.8072 | 1332.0137 | -74.0521 | 350 - 516 | [11]* |
| butanol | 4.4292 | 1305.001 | -94.676 | 419 - 563 | NIST |

\* excel fit with experimental data using the specified reference
\*\* excel fit with AVL FIRE™ component data

References

[1]     M.P. Edejer, G. Thodos, Vapor pressures of liquid nitrogen between the triple and critical points, J. Chem. Eng. Data. 12 (1967) 206–209.

[2]     G.T. Brower, G. Thodos, Vapor pressures of liquid oxygen between the triple point and critical point, J. Chem. Eng. Data. 13 (1968) 262–264.

[3]     J. Gmehling, ed., Water Vapor Pressure: Datasheet from "Dortmund Data Bank (DDB) -- Thermophysical Properties Edition 2014'' in SpringerMaterials, http://materials.springer.com/thermophysical/docs/vap_c174.

[4]     R. Prydz, R.D. Goodwin, Experimental melting and vapor pressures of methane, J. Chem. Thermodyn. 4 (1972) 127–133.

[5]     J. Gmehling, ed., Pentane Vapor Pressure: Datasheet from "Dortmund Data Bank (DDB) -- Thermophysical Properties Edition 2014'' in SpringerMaterials, http://materials.springer.com/thermophysical/docs/vap_c134.

[6]     T.R. Das, C.O. Reed Jr, P.T. Eubank, PVT [pressure-volume-temperature] surface and thermodynamic properties of butane, J. Chem. Eng. Data. 18 (1973) 244–253.

[7]     J. Gmehling, ed., Hexane Vapor Pressure: Datasheet from "Dortmund Data Bank (DDB) -- Thermophysical Properties Edition 2014'' in SpringerMaterials, http://materials.springer.com/thermophysical/docs/vap_c89.

[8]     J. Gmehling, ed., Heptane Vapor Pressure: Datasheet from "Dortmund Data Bank (DDB) -- Thermophysical Properties Edition 2014'' in SpringerMaterials, http://materials.springer.com/thermophysical/docs/vap_c91.

[9]     J. Gmehling, ed., Benzene Vapor Pressure: Datasheet from "Dortmund Data Bank (DDB) -- Thermophysical Properties Edition 2014'' in SpringerMaterials, http://materials.springer.com/thermophysical/docs/vap_c31.

[10]     J. Gmehling, ed., Methanol Vapor Pressure: Datasheet from "Dortmund Data Bank (DDB) -- Thermophysical Properties Edition 2014'' in SpringerMaterials, http://materials.springer.com/thermophysical/docs/vap_c110.

[11]     J. Gmehling, ed., Ethanol Vapor Pressure: Datasheet from "Dortmund Data Bank (DDB) -- Thermophysical Properties Edition 2014'' in SpringerMaterials, http://materials.springer.com/thermophysical/docs/vap_c11.

# Appendix C -  Alpha Function Parameters

**Soave $\alpha(T)$- Function**

The acentric constants from the Appendix A -Thermodynamic Properties were used.

**Stryjek & Vera $\alpha(T)$- Function**

**Table C-1:** Stryjek Vera $\alpha(T)$ parameters

| | Stryjek & Vera $\alpha(T)$ parameters[1] | |
| --- | --- | --- |
| | $\omega_{SV}$ | n |
| Inorganic | [-] | [-] |
| water | 0.34380 | -0.06635 |
| nitrogen | 0.03726 | 0.01996 |
| oxygen | 0.02128 | 0.01512 |
| carbondioxide | 0.22500 | 0.04285 |

Organic Hydrocarbons

| | | |
|---|---|---|
| methane | 0.01045 | -0.00159 |
| ethane | 0.09781 | 0.02669 |
| propane | 0.15416 | 0.03136 |
| butane | 0.20096 | 0.03443 |
| pentane | 0.25143 | 0.03946 |
| hexane | 0.30075 | 0.05104 |
| heptane | 0.35022 | 0.04648 |
| octane | 0.39822 | 0.04464 |
| decane | 0.49052 | 0.04510 |
| dodecane | 0.57508 | 0.05426 |
| tridecane | 0.62264 | 0.04157 |
| tetradecane | 0.66735 | 0.02686 |
| hexadecane | 0.74397 | 0.02665 |
| octadecane | 0.79278 | 0.08291 |
| eicosane | * | * |
| | | |
| isopentane | * | * |
| benzene | 0.20929 | 0.07019 |
| toluene | 0.26323 | 0.03849 |
| isooctane | * | * |
| methylnaphtalene | 0.37666 | -0.01842 |

Alcohols

| | | |
|---|---|---|
| methanol | 0.56533 | -0.16816 |
| ethanol | 0.64439 | -0.03374 |
| butanol | 0.59022 | 0.33431 |

* no parameter was found

**Twu $\alpha(T)$- Function**

**Table C-2:** Twu $\alpha(\mathrm{T})$ parameters

| | Twu parameters | $\alpha(\mathrm{T})$ | | Ref. |
|---|---|---|---|---|
| | L | M | N | |
| Inorganic | [-] | [-] | [-] | |
| water | 0.41330 | 0.87450 | 1.88210 | [2] |
| nitrogen | 0.32950 | 0.88275 | 1.08532 | [2] |
| oxygen | 0.55016 | 0.93343 | 0.69306 | [2] |
| carbondioxide | 0.84553 | 0.95264 | 0.80392 | [3] |
| | | | | |
| Organic Hydrocarbons | | | | |
| methane | 0.94543 | 1.24525 | 0.42415 | [4] |
| ethane | 0.21225 | 0.87204 | 1.70100 | [4] |
| propane | 0.77313 | 0.91240 | 0.72633 | [4] |
| butane | 1.16264 | 1.07189 | 0.55301 | [4] |
| pentane | 0.42068 | 0.83028 | 1.41573 | [4] |
| hexane | 1.09414 | 1.00138 | 0.72398 | [4] |
| heptane | 0.87995 | 0.91716 | 0.97192 | [4] |
| octane | 0.94534 | 0.89762 | 0.96850 | [4] |
| decane | 0.31655 | 0.82847 | 2.90395 | [2] |
| dodecane | 1.05832 | 0.86325 | 1.06679 | [4] |
| tridecane | 0.50969 | 0.82274 | 2.10994 | [5] |
| tetradecane | 1.16443 | 0.90359 | 1.08532 | [4] |
| hexadecane | 1.14769 | 0.86326 | 1.16627 | [4] |
| octadecane | 0.48072 | 0.78381 | 2.47646 | [5] |
| eicosane | 1.41753 | 1.00998 | 1.11291 | [4] |
| | | | | |
| isopentane | 1.03044 | 1.03445 | 0.67039 | [2] |
| benzene | 0.65252 | 0.83278 | 0.92329 | [4] |
| toluene | 1.21115 | 1.06277 | 0.60130 | [4] |
| isooctane | 0.87636 | 0.89061 | 0.88678 | [2] |
| 1-methylnaphtalene | 0.65454 | 0.83747 | 1.19661 | [2] |
| | | | | |
| Alcohols | | | | |
| methanol | 1.12033 | 1.07426 | 1.07504 | [3] |
| ethanol | 1.19559 | 1.01480 | 1.05841 | [2] |
| butanol | 1.14746 | 0.70955 | 0.99903 | [2] |

References

[1]     R. Stryjek, J.H. Vera, PRSV: An improved Peng-Robinson equation of state for pure compounds and mixtures, Can. J. Chem. Eng. 64 (1986) 323–333.

[2]     B. Schmid, Einsatz einer modernen Gruppenbeitragszustandsgleichung für die Synthese thermischer Trennprozesse, Carl von Ossietzky Universität Oldenburg, 2011.

[3]     J. Ahlers, T. Yamaguchi, J. Gmehling, Development of a universal group contribution equation of state. 5. Prediction of the solubility of high-boiling compounds in supercritical gases with the group contribution equation of state Volume-Translated Peng-Robinson, Ind. Eng. Chem. Res. 43 (2004) 6569–6576.

[4]     J. Gmehling, B. Kolbe, M. Kleiber, J. Rarey, Chemical thermodynamics for process simulation, John Wiley & Sons, 2012.

[5]     C.H. Twu, J.E. Coon, J.R. Cunningham, A new generalized alpha function for a cubic equation of state Part 2. Redlich-Kwong equation, Fluid Phase Equilib. 105 (1995) 61–69.

## Appendix D - UGC VTPR Parameters

**Table D-1: Main- and subgroups and van der Waals surface parameters**

| No. | main group (MG) | No. | sub group (SG) | $Q_k$ |
|---|---|---|---|---|
| 1 | $CH_2$ | [1] | $CH_3$ | 1.2958 |
| | | [2] | $CH_2$ | 0.9471 |
| | | [3] | CH | 0.2629 |
| | | [4] | C | 0 |
| 2 | C=C | [5] | $CH_2$=CH | 1.1507 |
| | | [6] | CH=CH | 1.3221 |
| | | [7] | $CH_2$=CH | 0.988 |
| | | [8] | CH=CH | 0.676 |
| | | [70] | C=C | 0.485 |
| 3 | ACH | [9]* | ACH | 0.4972 |
| | | [10]* | AC | 0.1885 |
| 4 | $ACCH_2$ | [11]* | $ACCH_3$ | 1.4843 |
| | | [12]* | $ACCH_2$ | 1.1356 |
| | | [13]* | ACCH | 0.4514 |

| | | | OH | |
|---|---|---|---|---|
| 5 | OH | [14]* | (primary) | 1.0189 |
| 6 | $CH_3OH$ | [15]* | $CH_3OH$ | 0.8727 |
| 7 | $H_2O$ | [16]* | $H_2O$ | 1.5576 |
| 8 | ACOH | [17]* | ACOH | 0.9013 |
| 9 | $CH_2CO$ | [18]* | $CH_3CO$ | 1.448 |
| | | [19]* | $CH_2CO$ | 1.18 |
| 10 | CHO | [20]* | CHO | 0.948 |
| 11 | CCOO | [21]* | $CH_3COO$ | 1.728 |
| | | [22]* | $CH_2COO$ | 1.42 |
| 150 | $NH_3$ | [300] | $NH_3$ | 0.778 |
| 151 | $CO_2$ | [306] | $CO_2$ | 0.982 |
| 152 | $CH_4$ | [307] | $CH_4$ | 1.124 |
| 153 | $O_2$ | [308] | $O_2$ | 0.849 |
| 154 | Ar | [305] | Ar | 1.116 |
| 155 | $N_2$ | [304] | $N_2$ | 0.93 |
| 156 | $H_2S$ | [303] | $H_2S$ | 1.202 |
| 157 | $H_2$ | [302] | $H_2$ | 0.571 |
| | | [309] | $D_2$ | 0.527 |
| 158 | CO | [301] | CO | 0.828 |
| 160 | $SO_2$ | [310] | $SO_2$ | 1.164 |

* given the position of [70] C=C, to every sub group number from 9 to 70, +1 is added

**Table D-2: Group interaction parameters for the VTPR group contribution equation of state**

| MG | MG | $a_{nm}$ | $b_{nm}$ | $c_{nm}$ | $a_{mn}$ | $b_{mn}$ | $c_{mn}$ |
|---|---|---|---|---|---|---|---|
| n | m | [K] | | [$K^{-1}$] | [K] | | [$K^{-1}$] |
| 1 | 2 | 171.47 | -0.0432 | | -87.609 | -0.0544 | |
| 1 | 3 | 54.259 | 0.2882 | | 35.483 | -0.3693 | |
| 1 | 4 | 17.268 | -0.006983 | | -12.568 | 0.0237 | |
| 1 | 5 | 1809.5 | -0.4856 | -2.3211E-03 | 725.66 | -0.905 | 3.1538E-03 |
| 1 | 6 | 1733.4 | 1.8057 | -6.1885E-03 | 50.672 | -0.6378 | 1.7753E-04 |
| 1 | 7 | 2096.9 | -1.6565 | 5.9001E-01 | 56.588 | 0.5883 | 4.4729E-04 |
| 1 | 8 | 2115.5 | -2.2215 | | 53.666 | 1.4484 | |
| 1 | 9 | 425.31 | 0.6879 | -3.0781E-04 | 284.25 | -1.7731 | 1.6358E-03 |
| 1 | 10 | 757.96 | -0.0334 | | 169.86 | 0.0377 | |
| 1 | 11 | 138.56 | 1.5746 | -2.1910E-03 | 779.9 | -4.5744 | 5.8039E-03 |
| 1 | 150 | 402.49 | | | 73.633 | | |
| 1 | 151 | 403.11 | -0.1999 | -6.6800E-05 | 204.83 | -1.3096 | 1.1967E-03 |
| 1 | 152 | 66.255 | 0.0135 | | -23.372 | -0.0844 | |
| 1 | 153 | 193.93 | 0.0692 | 1.1713E-03 | 18.582 | -0.1597 | -1.3825E-03 |
| 1 | 154 | 81.304 | -0.0702 | | 8.4429 | -0.0506 | |
| 1 | 155 | 282.56 | -0.4109 | 3.1249E-03 | 26.923 | -0.5125 | -7.8581E-04 |
| 1 | 156 | 512.67 | -0.6966 | -4.9666E-04 | 120.11 | -1.1511 | 2.0618E-03 |

| | | | | | | | |
|---|---|---|---|---|---|---|---|
| 1 | 157 | 349.49 | -0.3913 | | 63.418 | -0.1526 | |
| 1 | 158 | 10.488 | | | 43.803 | | |
| 2 | 3 | 69.495 | -1.1411 | 1.3205E-03 | 101.92 | 0.5243 | 3.4756E-04 |
| 2 | 4 | 295.33 | -1.6878 | | -590.18 | 3.1509 | |
| 2 | 5 | 756.09 | 1.4097 | -1.9269E-03 | 2049.9 | 6.3523 | -1.3347E-03 |
| 2 | 6 | 3394.3 | 0.1123 | | -113.11 | 0.1866 | |
| 2 | 8 | 1058.4 | -0.1814 | | 528.72 | -0.9161 | |
| 2 | 9 | 366.63 | -0.1551 | | -102.95 | 0.254 | |
| 2 | 10 | 725.18 | | | -109.36 | | |
| 2 | 11 | -85.302 | 0.5312 | | 262.55 | -0.5966 | |
| 2 | 151 | 7.9448 | | | 218.62 | | |
| 2 | 152 | -10.839 | | | 89.576 | | |
| 2 | 155 | 116.49 | | | 116.58 | | |
| 3 | 4 | 85.631 | -0.8635 | | -37.825 | 1.1096 | |
| 3 | 5 | 1065.5 | 0.2236 | -1.7246E-03 | 1234.6 | 1.3853 | 1.5753E-04 |
| 3 | 6 | 1461.5 | -0.6763 | -7.3173E-04 | 102.41 | -0.6116 | -1.2890E-05 |
| 3 | 7 | 902.7 | 0.4987 | -2.4275E-03 | -515.45 | 5.2073 | -5.3002E-03 |
| 3 | 8 | 1274 | -1.5913 | | 1302.8 | 3.2141 | |
| 3 | 9 | -29.162 | -0.0322 | 1.6364E-04 | 214.38 | 0.0534 | 8.8990E-05 |
| 3 | 10 | 238.95 | 0.5456 | | -238.13 | 0.7806 | |
| 3 | 11 | 25.693 | -0.4457 | 1.6479E-03 | 538.6 | -2.1287 | 1.8735E-03 |
| 3 | 150 | 414.74 | | | 88.727 | | |
| 3 | 151 | 161.38 | | | 37.2 | | |
| 3 | 152 | 257.08 | | | -91.888 | | |
| 3 | 153 | 320.01 | | | 2.9972 | | |
| 3 | 154 | 191.77 | | | 19.421 | | |
| 3 | 155 | 387.44 | | | -4.3791 | | |
| 3 | 156 | 54.618 | | | -31.946 | | |
| 3 | 157 | 398.88 | | | 116.25 | | |
| 4 | 5 | -731.01 | 11.94 | -1.9532E-02 | 5960.3 | -4.297 | 9.3865E-03 |
| 4 | 6 | -779.2 | 11.387 | -1.5980E-02 | -4.458 | -0.388 | 3.0633E-04 |
| 4 | 7 | 4199 | -5.7863 | 6.1302E-02 | -353.75 | 3.8076 | -4.6341E-03 |
| 4 | 8 | 820.75 | 0.1362 | | 2105.2 | -2.3733 | |
| 4 | 9 | 440.19 | -0.4431 | 1.9219E-03 | 235.93 | -1.2281 | 7.2999E-04 |
| 4 | 10 | 880.94 | | | -39.748 | | |
| 4 | 11 | 574.06 | -2.2111 | 7.0491E-03 | 264.6 | -1.4341 | 9.0620E-05 |
| 4 | 151 | 207.75 | 1.1881 | | 153.19 | -1.1845 | |
| 4 | 152 | 217.05 | | | -108.43 | | |
| 5 | 6 | 97.346 | -1.3023 | 1.3126E-03 | -188.6 | 2.6813 | -2.3537E-03 |
| 5 | 7 | -789.48 | 2.8178 | -1.9454E-03 | 478.28 | -0.5389 | -2.0384E-03 |
| 5 | 8 | -286.06 | | | -260.82 | | |
| 5 | 9 | -57.664 | 0.7875 | -1.5955E-04 | 540.61 | -0.9922 | 3.5082E-04 |
| 5 | 10 | 4566.5 | 3.0252 | | -975.34 | 2.2004 | |
| 5 | 11 | -221.85 | 1.2243 | 9.9802E-04 | | | -3.6391E-04 |
| 5 | 150 | -168.15 | | | -195.62 | | |
| 5 | 151 | 440.88 | | | 578.82 | | |
| 6 | 7 | -387.4 | 1.9621 | -3.4336E-03 | -168.82 | 0.6674 | 4.1881E-03 |
| 6 | 8 | -273.88 | | | -69.044 | | |

| | | | | | | | |
|---|---|---|---|---|---|---|---|
| 6 | 9 | 143.82 | -0.7722 | | 275.58 | 0.1849 | |
| 6 | 10 | -847.96 | 2.1019 | | -1962.7 | 5.9274 | |
| 6 | 11 | 222.5 | -0.9449 | | 522.89 | -0.2263 | |
| 6 | 150 | -160.96 | | | -402.93 | | |
| 6 | 151 | -41.601 | | | 631.57 | | |
| 6 | 152 | 16.899 | | | 703.79 | | |
| 6 | 153 | 144.87 | | | 918.38 | | |
| 6 | 156 | -144.05 | | | 851.54 | | |
| 6 | 157 | 214.5 | | | 982.24 | | |
| 6 | 158 | 105.1 | | | 945.26 | | |
| 7 | 8 | 97.16 | -0.2118 | | 92.303 | -0.7272 | |
| 7 | 9 | -314.91 | 0.5693 | 2.6686E-03 | 577.46 | -1.1183 | -6.2358E-04 |
| 7 | 10 | -270.08 | 0.8723 | | 329.03 | -0.2521 | |
| 7 | 150 | -816.21 | 1.9119 | 6.9311E-04 | -337.79 | -0.1454 | -1.1401E-04 |
| 7 | 151 | -1643.4 | 10.588 | -1.0830E-02 | 1852.9 | 2.2201 | 1.1100E-03 |
| 7 | 152 | -1848.2 | 12.27 | -1.1594E-02 | 10201 | -38.292 | 3.8456E-02 |
| 7 | 153 | 1488.4 | 0.3965 | 7.9000E-04 | -503.96 | -1.0566 | 7.9000E-03 |
| 7 | 154 | -2242.4 | 14.067 | -1.5246E-02 | 1872.6 | 32.273 | 2.9551E-02 |
| 7 | 155 | -1877.1 | 12.93 | -1.0980E-02 | 2210.7 | -7.0804 | 7.3700E-03 |
| 7 | 156 | -504.51 | 5.2818 | -6.8600E-03 | -228.81 | -0.6266 | 1.8280E-02 |
| 7 | 157 | 726.59 | 1.9341 | 1.3018E-03 | -1277.1 | 0.4387 | 1.3087E-02 |
| 7 | 160 | -91.076 | 1.2411 | | 721.63 | 11.199 | |
| 8 | 9 | -514.14 | 1.2892 | | -393.16 | 0.0573 | |
| 9 | 151 | -177.94 | | | 267.6 | | |
| 10 | 151 | 32.7 | | | 207.48 | | |
| 11 | 151 | -146.54 | | | 95.601 | | |
| 11 | 155 | 410.28 | | | 53.021 | | |
| 150 | 152 | 495.58 | | | 417.63 | | |
| 150 | 154 | 525.84 | | | 367.48 | | |
| 150 | 155 | 786.44 | | | 638.21 | | |
| 150 | 157 | 1031.7 | | | 1473.9 | | |
| 151 | 152 | 222.08 | -0.4594 | 1.2899E-04 | 146.28 | 0.0194 | 8.9050E-06 |
| 151 | 153 | 199.51 | | | 98.663 | | |
| 151 | 154 | -215.08 | 1.5072 | | 551.13 | -1.9153 | |
| 151 | 155 | 184.15 | | | 80.825 | | |
| 151 | 156 | 112.61 | | | 114.7 | | |
| 151 | 157 | 703.37 | -1.3791 | | 805.44 | -0.5845 | |
| 151 | 158 | 241.02 | | | -6.3061 | | |
| 151 | 160 | 666.32 | | | -130.37 | | |
| 152 | 154 | 1.7641 | | | 27.639 | | |
| 152 | 155 | 53.308 | | | 12.181 | | |
| 152 | 156 | 659.84 | -1.9066 | | 59.702 | 0.5676 | |
| 152 | 157 | 170.57 | | | 61.06 | | |
| 152 | 158 | 54.47 | | | -0.3496 | | |
| 152 | 160 | 98.804 | | | 334.1 | | |
| 153 | 154 | -5.0462 | -0.0702 | | 36.42 | -0.056 | |
| 153 | 155 | 3.6807 | | | 16.868 | | |
| 153 | 160 | 140.61 | | | 430.23 | | |

| 154 | 155 | 9.4153 | | | 3.5561 | | |
|---|---|---|---|---|---|---|---|
| 154 | 157 | 147.63 | | | 86.176 | | |
| 154 | 158 | 5.4295 | | | 16.976 | | |
| 154 | 160 | 221.98 | | | 175.77 | | |
| 155 | 156 | 102.41 | | | 548.12 | | |
| 155 | 157 | 85.682 | | | 78.387 | | |
| 155 | 158 | -4.9625 | | | -0.0648 | | |
| 155 | 160 | 132.37 | -1.0722 | | 755.11 | 0.1987 | |
| 156 | 157 | 432.76 | | | 32.03 | | |
| 156 | 158 | 445.53 | | | 171.29 | | |
| 157 | 158 | 807.19 | -11.043 | 3.2874E-02 | 1118.5 | -25.222 | 1.5274E-01 |
| 157 | 160 | 2637.2 | | | 587.42 | | |

References

[1]     B. Schmid, J. Gmehling, Revised parameters and typical results of the VTPR group contribution equation of state, Fluid Phase Equilib. 317 (2012) 110–126.

# Appendix E -  Mixture Fugacities

Peng-Robinson equation of state:

$$P = \frac{RT}{v-b} - \frac{a(T,\omega)}{v^2 + 2bv - b^2}$$

(E.1)

Classical vdW Mixing Rule:

$$\varphi_i^{v,l} = \frac{b_i}{b}(z-1) - \ln(z-\beta) - q_i I$$

$$q_i = q\left(\frac{2\sum_j x_j^{v,l} a_{ij}}{a} - \frac{b_i}{b}\right)$$

$$I = \frac{1}{2\sqrt{2}} \ln \frac{z + (1+\sqrt{2})\beta}{z + (1-\sqrt{2})\beta}$$

(E.2)

HV Mixing Rule:

$$\varphi_i^{v,l} = \frac{b_i}{b}(z-1) - \ln(z-\beta) - q_i I$$

$$q_i = \frac{a_i}{b_i RT} + \frac{\ln \gamma_i}{C_{HV}}$$

$$I = \frac{1}{2\sqrt{2}} \ln \frac{z + \left(1+\sqrt{2}\right)\beta}{z + \left(1-\sqrt{2}\right)\beta}$$

(E.3)

MHV Mixing Rule:

$$\varphi_i^{v,l} = \frac{b_i}{b}(z-1) - \ln(z-\beta) - q_i I$$

$$q_i = \frac{a_i}{b_i RT} + \frac{1}{C_{HV}}\left(\ln \gamma_i + \ln \frac{b}{b_i} + \frac{b_i}{b} - 1\right)$$

$$I = \frac{1}{2\sqrt{2}} \ln \frac{z + \left(1+\sqrt{2}\right)\beta}{z + \left(1-\sqrt{2}\right)\beta}$$

(E.4)

LCVM Mixing Rule

$$\varphi_i^{v,l} = \frac{b_i}{b}(z-1) - \ln(z-\beta) - q_i I$$

$$q_i = \frac{a_i}{b_i RT} + \left(\frac{\lambda}{C_{HV}} + \frac{1-\lambda}{C_{MHV}}\right)\ln \gamma_i + \frac{1-\lambda}{C_{MHV}}\left(\ln \frac{b}{b_i} + \frac{b_i}{b} - 1\right)$$

$$I = \frac{1}{2\sqrt{2}} \ln \frac{z + \left(1+\sqrt{2}\right)\beta}{z + \left(1-\sqrt{2}\right)\beta}$$

(E.5)

Volume-Translated PR equation of state:

$$P = \frac{RT}{v-b+c} - \frac{a(T,\omega)}{(v+c)(v+b+c)+b(v-b+c)} \qquad (E.6)$$

Classical vdW Mixing Rule:

$$\ln\varphi_i^{v,l} = \frac{b_i}{b}(z-1) - \ln(z-\beta+\chi) - q_iI$$

$$q_i = q\left(\frac{2\sum\limits_j x_i^{v,l}a_{ij}}{a} - \frac{b_i}{b}\right) \qquad (E.2)$$

$$I = \frac{1}{2\sqrt{2}}\ln\left(\frac{z+\chi+\left(1+\sqrt{2}\right)\beta}{z+\chi+\left(1-\sqrt{2}\right)\beta}\right)$$

UGC Mixing Rule

$$\ln\varphi_i^{v,l} = \left(\frac{2\sum\limits_j x_i^{v,l}b_{ij}}{b} - 1\right)(z+\chi-1) - \ln(z-\beta+\chi) - \chi_i - q_iI$$

$$q_i = \frac{a_i}{b_iRT} + \frac{\ln\gamma_i}{C_{UGC}} \qquad (E.3)$$

$$I = \frac{1}{2\sqrt{2}}\ln\frac{z+\chi+\left(1+\sqrt{2}\right)\beta}{z+\chi+\left(1-\sqrt{2}\right)\beta}$$

References

[1]    S.I. Sandler, H. Orbey, Cubic Equations of State and Their Mixing Rules, 1998.

[2]    J. Gmehling, B. Kolbe, M. Kleiber, J. Rarey, Chemical thermodynamics for process simulation, John Wiley & Sons, 2012.